INVESTIGATION AND DESIGN OF IMPULSE RADIATING ANTENNAS DRIVEN WITH MARX GENERATOR

A THESIS SUBMITTED TO
THE GRADUATE SCHOOL OF NATURAL AND APPLIED SCIENCES
OF
MIDDLE EAST TECHNICAL UNIVERSITY

BY

ÖZGE EREN

IN PARTIAL FULFILLMENT OF THE REQUIREMENTS
FOR
THE DEGREE OF MASTER OF SCIENCE
IN
ELECTRICAL AND ELECTRONICS ENGINEERING

FEBRUARY 2021

Approval of the thesis:

INVESTIGATION AND DESIGN OF IMPULSE RADIATING ANTENNAS DRIVEN WITH MARX GENERATOR

submitted by **ÖZGE EREN** in partial fulfillment of the requirements for the degree of **Master of Science in Electrical and Electronics Engineering, Middle East Technical University** by,

Prof. Dr. Halil Kalıpçılar
Dean, Graduate School of **Natural and Applied Sciences** ________________

Prof. Dr. İlkay Ulusoy
Head of Department, **Electrical and Electronics Engineering** ________________

Prof. Dr. Özgür Ergül
Supervisor, **Electrical and Electronics Engineering, METU** ________________

Examining Committee Members:

Prof. Dr. Şimşek Demir
Electrical and Electronics Engineering, METU ________________

Prof. Dr. Özgür Ergül
Electrical and Electronics Engineering, METU ________________

Prof. Dr. Özlem Aydın Çivi
Electrical and Electronics Engineering, METU ________________

Prof. Dr. Serhat Çakır
Physics, METU ________________

Prof. Dr. Özcan Kalenderli
Electrical Engineering, ITU ________________

Date: 11.02.2021

I hereby declare that all information in this document has been obtained and presented in accordance with academic rules and ethical conduct. I also declare that, as required by these rules and conduct, I have fully cited and referenced all material and results that are not original to this work.

Name, Last name : Özge Eren

Signature :

ABSTRACT

INVESTIGATION AND DESIGN OF IMPULSE RADIATING ANTENNAS DRIVEN WITH MARX GENERATOR

Eren, Özge
Master of Science, Electrical and Electronics Engineering
Supervisor : Prof. Dr. Özgür Ergül

February 2021, 108 pages

Pulsed power technologies have been a subject of intense studies for many years. These technologies are used in a plethora of applications in diverse areas, such as defense industry, biology, and food processing.

In this study, pulsed electric field distributions at kV/m levels are aimed to be obtained by driving an antenna with an impulse generator. A Marx generator is preferred and built to generate impulses. Output signal from the Marx generator, whose rise time is slow to feed antenna, is passed through a pulse forming line (PFL) to obtain a suitable signal for antenna feeding. A pulse shaped by the PFL is transferred to an impulse radiating antenna with the help of a balun. Thus, when the whole system is combined, high-quality electromagnetic pulses can be obtained.

Within the scope of this thesis, a Marx generator, a PFL, a Klopfenstein tapered balun, and an impulse radiating antenna are designed, simulated, fabricated, and tested experimentally.

Building the overall system required overcoming several important challenges, as well as monitoring potential risks, such as high voltages and electrical breakdowns, which bring limitations on the design of the system.

Keywords: Pulsed power, high-power electromagnetics, Marx generators, pulse forming lines, impulse radiating antennas

ÖZ

MARX ÜRETECİ İLE SÜRÜLEN DARBE IŞIYAN ANTEN İNCELENMESİ VE TASARIMI

Eren, Özge
Yüksek Lisans, Elektrik ve Elektronik Mühendisliği
Tez Yöneticisi: Prof. Dr. Özgür Ergül

Şubat 2021, 108 sayfa

Darbeli güç teknolojileri uzun yıllardır yoğun çalışmalara konu olmuştur. Bu teknolojiler, savunma sanayii, biyoloji araştırmaları ve gıda işleme gibi çeşitli alanlarda çok sayıda kullanılmaktadır.

Bu çalışmada, bir darbe üreteci ile bir antenin sürülmesiyle kV/m seviyelerinde darbe elektrik alanı dağılımları elde edilmeye çalışılmıştır. Darbe sinyallerinin üretilebilmesi için bir Marx üreteci tercih edilmiş ve kullanılmıştır. Marx üretecinin çıkış sinyal yükselme hızı bir anteni sürmek için yavaş kaldığından, sinyal bir darbe şekillendirme hattından geçirilerek ve hızladırılarak anten sürmeye uygun hale getirilmiştir. Darbe şekillendirme hattı çıkışındaki sinyal bir balun yardımıyla darbe ışıyan antene aktarılmıştır. Böylece, tüm sistemin bir araya getirilmesiyle, yüksek kalitede elektromanyetik darbe sinyalleri elde edilebilmektedir.

Bu tez kapsamında, bir Marx üreteci, bir darbe şekillendirme hattı, bir Klopfenstein eğimli balun ve bir darbe ışıyan anten tasarımı, benzetim, üretim ve deneysel testler kapsamında gerçeklenmiştir.

Genel sistemi oluşturmak, birçok önemli zorluğun üstesinden gelmenin yanı sıra, sistemin tasarımına kısıtlamalar getiren yüksek gerilimler ve elektriksel atlamalar gibi potensiyel risklerin izlenmesini gerektirmiştir.

Anahtar Kelimeler: Darbeli güç, yüksek güçlü elektromanyetik, Marx üreteçleri, darbe şekillendirme hatları, darbe ışıyan antenler

to the memory of Turkish soldiers who will always be remembered

ACKNOWLEDGMENTS

First of all, I would like to express my gratitude to my supervisor, Prof. Dr. Özgür Ergül, for his support and guidance. I wish to thank him for spending time to read this thesis and providing useful suggestions. I am grateful to him for giving me the opportunity to study with him for master degree in METU.

I would like to thank to TÜBİTAK BİLGEM for supporting this study financially. I am also thankful to my collegue Dr. Raşid Ahmed Yıldız for his mechanical design. I wish to thank to Yunus Emre Sümer for his help in the experiments.

Finally, I must express my very profound gratitude to my family and to my husband Onur, for providing me with unfailing support and continuous encouragement throughout my years of study and through the process of researching and writing this thesis. This accomplishment would not have been possible without them. Thank you.

TABLE OF CONTENTS

LIST OF TABLES

TABLES

LIST OF FIGURES

FIGURES

LIST OF ABBREVIATIONS

ABBREVIATIONS

CST	Computer Simulation Technology
CVR	Current Viewing Resistor
EM	Electromagnetics
EMC	Electromagnetic Compatibility
EMI	Electromagnetic Interference
EMP	Electromagnetic Pulse
HIRA	Half Impulse Radiating Antenna
HPEM	High Power Electromagnetics
HPM	High Power Microwave
IEMI	Intentional Electromagnetic Interference
IRA	Impulse Radiating Antenna
NEMP	Nuclear Electro Magnetic Pulse
PEF	Pulsed Electric Field
PFL	Pulse Forming Line
PTFE	Polytetrafluoroethylene (Teflon)

TEM	Transverse Electro Magnetics
TLM	Transmission Line Method
UWB	Ultra-Wide Band
VNA	Vector Network Analyzer

CHAPTER 1

INTRODUCTION

Pulsed power technology has been the research subject of physicists and engineers with an increasing interest for many years. It has many military and civilian areas applications, and its application areas and techniques are still being investigated. The primary purpose of the research of modern pulsed power technology is to simulate a nuclear electromagnetic pulse (NEMP). As pulsed power technologies are continuously researched, many application areas, such as nonlethal directed energy weapons, target identification, radars applications, biological and medical practices, and air purifications, have been discovered.

Pulsed power was first used for radar applications in World War II. The figure related to the application areas is given in Figure 1.1 [1].

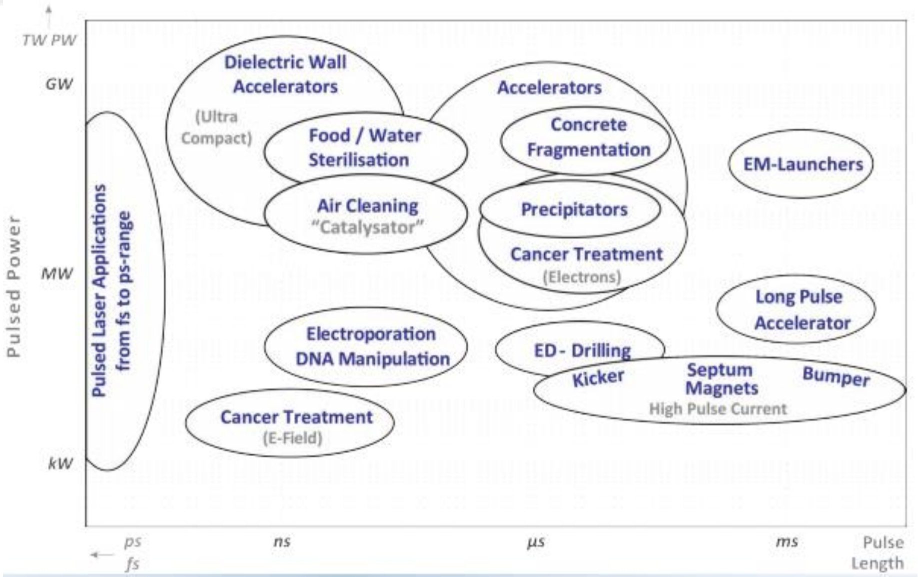

Figure 1.1: Application areas of pulsed power technology [1]

Pulsed power is the storage of the electrical energy for a relatively long time and compression with the help of some components to transfer an instant high power to the relevant load in a very short time (picoseconds to microseconds). Although the storage time of the energy varies depending on the systems, it is minutes in some systems and milliseconds in repetitive systems. Discharge times can be microseconds to picoseconds depending on the application. Energy per pulse can range from 1 J-120 J, corresponding to peak powers from MWs to hundreds of GWs. These systems have low energy levels because of the very short pulse durations, but they can reach very high peak power levels. Thanks to pulsed power technologies, it is also possible to create an electromagnetic pulse (EMP) to be used in many application areas. An EMP, also called a transient electromagnetic signal, is a short burst of electromagnetic energy. In fact, one of the most well-known EMP phenomena is the natural lightning. When lightning falls due to current flow in mega-amperes levels, electronic devices may be shut down, malfunction, or be permanently damaged. In the technological areas, Marx generators and especially high-speed closing switches are generally used to build small-scale EMP generators. In such a device, a Pulsed Electric Field (PEF) can be obtained by transferring the compressed power to ultra-wide band (UWB) antenna. Very-fast closing switches, which are often based on the phenomenon of electrical breakdown, are of great importance in these technologies.

In this thesis, a small-scale high-power electromagnetic pulse generator design, analysis, production, and tests were carried out. The block diagram of the design can be seen in Figure 1.2.

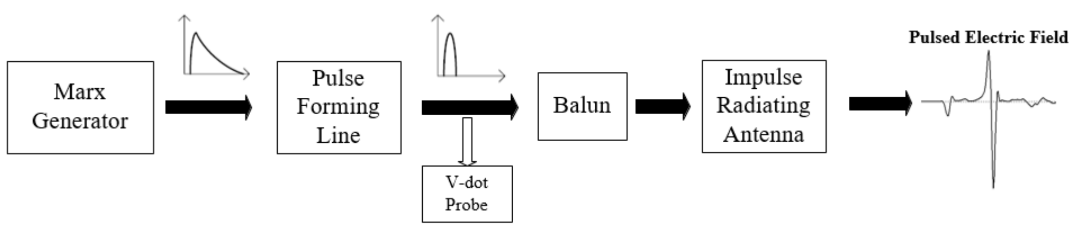

Figure 1.2: The block diagram of the small-scale high-power electromagnetic pulse generator

The designed and implemented EMP generator system has potentials to be useful in defense and medical applications in the future. Basically, it consists of a small Marx generator, a pulse forming line (PFL, a balun, an impulse radiating antenna (IRA) and a V-dot probe. An EMP signal with a broad bandwidth is tried to be obtained across the system. Pspice and CST Microwave Studio are used for circuit and electromagnetics simulations, respectively. The operation principles of the Marx generator, PFL, balun, IRA, and measurement system were studied individually, while experiments were carried out by building the entire system.

The thesis is divided into 5 chapters, considering the overall work involving high-power electromagnetic pulse generator design, analysis, and experiments. In the next chapter, literature on the subject is first summarized, considering similar systems. Marx, PFL, IRA, and V-dot probe are provided individually. In the third chapter, working principles of these components are explained, along with the specification of the design parameters. Simulation and component-level experiment results of the designs are given in the fourth chapter. Then, fabrication of the Marx generator, PFL, balun, IRA and V-dot probe, as well as the experimental results for the overall system are shared. In the last chapter, the pros and cons of the system are evaluated, together with possible directions in the context of future works.

CHAPTER 2

LITERATURE REVIEW

2.1 High Power Uwb System

EMP systems are often be called high-power UWB systems in the literature. Their applications include UWB pulse radars for detecting buried mines or people under debris [2], measuring electromagnetic compatibility (EMC) of electronic devices (in the form of NEMP) [3], UWB communication, and electromagnetic jamming [4]. In military applications, it is aimed to eliminate enemy elements or terrorist attacks, to remotely destroy target electronic devices, or to make them completely inoperable [5], [6].

Electromagnetic signals with sufficient intensity and 200 MHz - 5 GHz frequency range can cause permanent or temporary damage to target electronic systems. The electromagnetic effect induced on an electronic system is often called an intentional electromagnetic interference (IEMI).

Electronic systems can be damaged with different types of incoming signal, which can be listed as follows [7].

- An intense narrowband signal with several frequency variations
- An UWB pulse (spectral content from hundreds of MHz to several GHz);
- a burst of many UWB pulses.

Lightnings are the most well-known natural formation that affect electronic devices. Lightning strikes with pulse durations of microseconds can reach MVs levels, and they create EMP effects. Similar effects can also be created by humans. Protection methods against EMP effects are among the essential in EMC engineering.

High power electromagnetic (HPEM) systems, which have gained importance in defense industry in recent years, can be used to disrupt and inactivate an electronic system deliberately. The figure given below illustrates the distribution of typical spectral magnitudes of electromagnetic environments [7]. Specifically, in Figure 2.1 lightning is represented with high amplitudes but low frequencies [8], while UWB or narrowband signals (referred to as high-power microwave) have lower power levels.

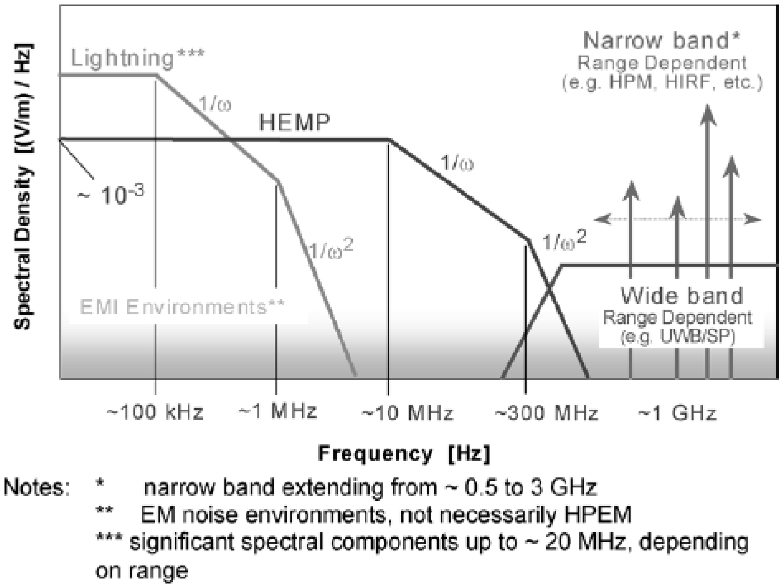

Figure 2.1: Spectral density vs. frequency graph for various EMI environments [7]

The effects of IEMI on target electronic circuits can be described as follows [7].

- Noise/False Information (Front Door): It creates noise (distortion) on the signal received by sensitive receivers.
- Soft-Kill (Back Door): It causes the system to stop or shut down, causing temporary damage to the system. Usually, the problem disappears when the system is restarted.
- Hard-Kill (Back Door): High electric field affects the transistors in the target, causing a breakdown in the system. The damaged component needs to be replaced.

High electrical field intensities are usually required to see the soft-kill and hard-kill effects.

UWB technologies started to attract attention in the 1980s. HPEM sources are categorized by Giri according to bandwidth, as listed in Table 2.1, given below [9].

Table 2.1. Categorization of bandwidth values [9].

Hypoband or narrowband	bw < 1%
Mesoband	1% < bw < 100%
Sub-hyperband	100% < bw< 163.4%
Hyperband	163.4% < bw<200 %

In a mesoband system, a wideband antenna is driven by a transmission line, which oscillates in 100-700 MHz, or a transient signal is transmitted to the oscillating antenna with a switch [9]. Using this method, Baum designed a system called MATRIX with a Half IRA [10]. This system started full-scale testing in Air Force Research laboratory in 2003. Oscillation frequency can be changed from 180 MHz to 600 MHz. At 15 m, 6 kV/m peak electric field strength has been reached and, as can be seen in Figure 2.2.

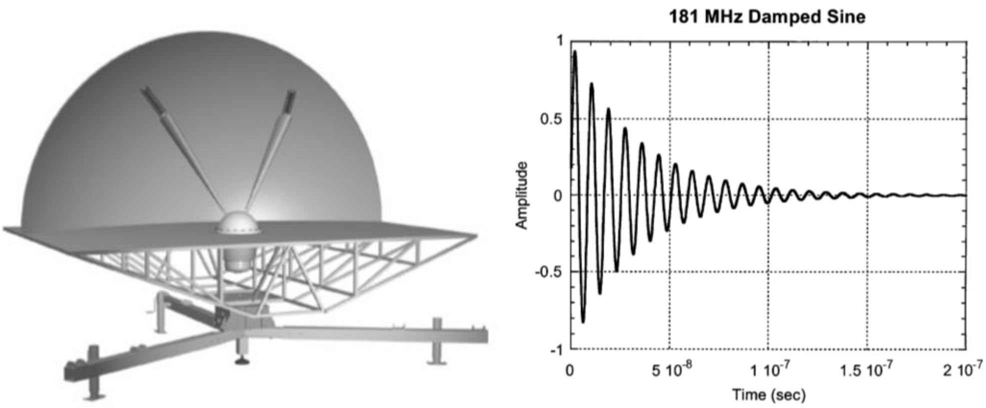

Figure 2.2: MATRIX oscillator source and electric field signal observed at 15 m [10]

DIEHL developed a similar mesoband system in Germany. This HPEM system, known as the DS110 series, is one of the damped sine sources and it can be seen in Figure 2.3. The system, driven by 400 kV and having a center frequency of 375 MHz, is designed with a cylindrical coil antenna. 125 kV/m was observed at 1 m. Signal form and frequency spectrum are also given in Figure 2.3. DIEHL further worked on a DS350 system with a 1 MV generator oscillating at 100 MHz [11] [12]. Different frequencies in diverse amplitudes could be obtained in this system using different insulation materials. DIEHL also worked on explosive UWB systems [13].

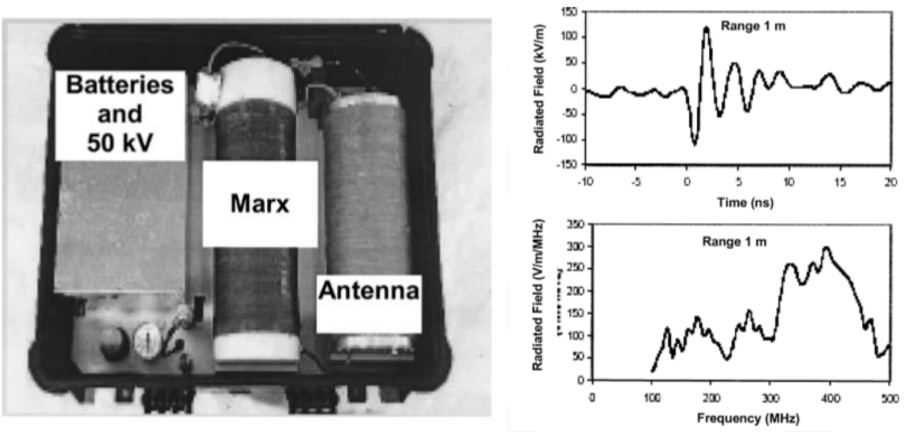

Figure 2.3: DIEHL System and the signal observed at 1 m [11]

H-series system built in Air Force Research Laboratory is also an example of subhyperband sources. In this system, high power UWB pulses were obtained using a coaxial pulse-forming line and a high-pressure hydrogen switch. The H-2 series was operational in 1992 for HPEM production using a 40-ohm coaxial PFL. The system that can produce 300 kV peak voltage and 250 ps rise time pulse is depicted in Figure 2.4 [14]. Using a large TEM horn antenna reached 43 kV/m peak electric field at 10 m.

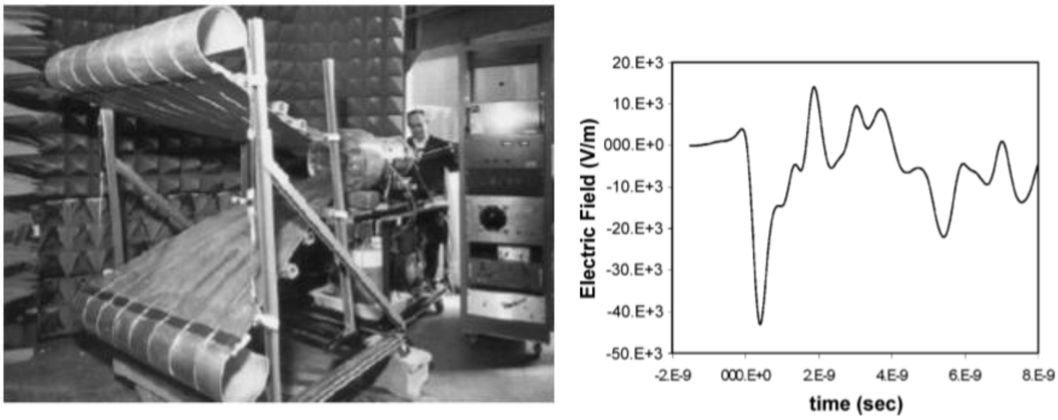

Figure 2.4: H-2 system with a large TEM horn antenna [14]

Transient high output radiator (THOR), another subhyperband system, reached 68 kV/m at 10 m. In this system, which is very similar to the H-2 series, the TEM horn antenna has been used. The system includes frequency components between 200 MHz and 1 GHz [15].

Systems with impulse radiating antennas are good examples of hyperband systems. In a system developed and used in 1994 with a high-pressure hydrogen switch and a focusing lens, an IRA with a 2 m reflector reached a peak electric field intensity of 4.6 kV at 305 m with a 60 kV source, as shown in Figure 2.5. This system had 200 Hz PRF in repetition mode, while the frequency band was between 200 MHz and 3 GHz [16], [17].

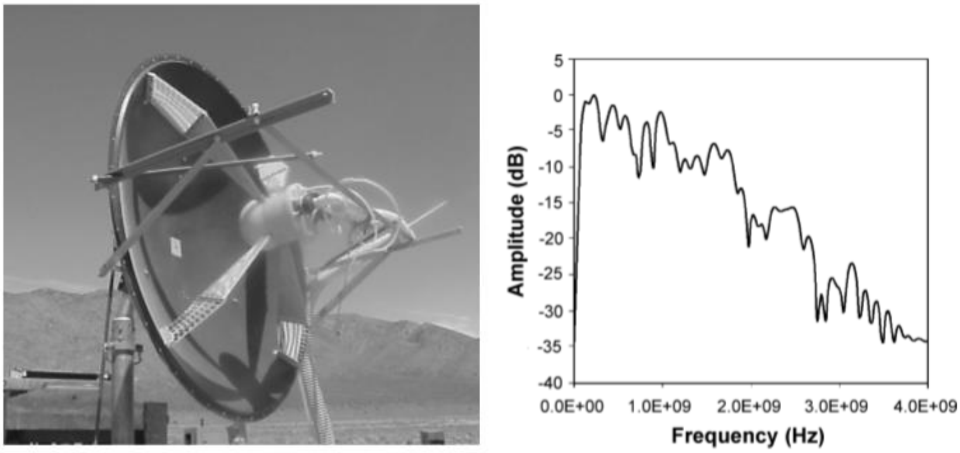

Figure 2.5: An example of a hyperband system with an IRA [16], [17]

Due to problems, such as balun and trigger jitter, in systems where full IRAs are used, half IRA systems have been developed which can be driven with focus from a high-voltage signal. However, in such a system, there is no uniformly symmetric field pattern since a finite ground plane is used [18]. A similar system, namely JOLT, was developed in AFRL from 1997 to 1999 [19]. A half-IRA (HIRA) with 85-ohm was driven with an oil transfer capacitor and a 1 MV resonant transformer. The JOLT system is depicted in JOLT Figure 2.6, while the radiated field and frequency spectrum provided by the system are illustrated in Figure 2.7. WIS and Rheinmetall have developed a similar system with a HIRA. It was a system that could generate 60 kV/m electric field intensity at 100 m and had a pulse duration of 650 ps [20].

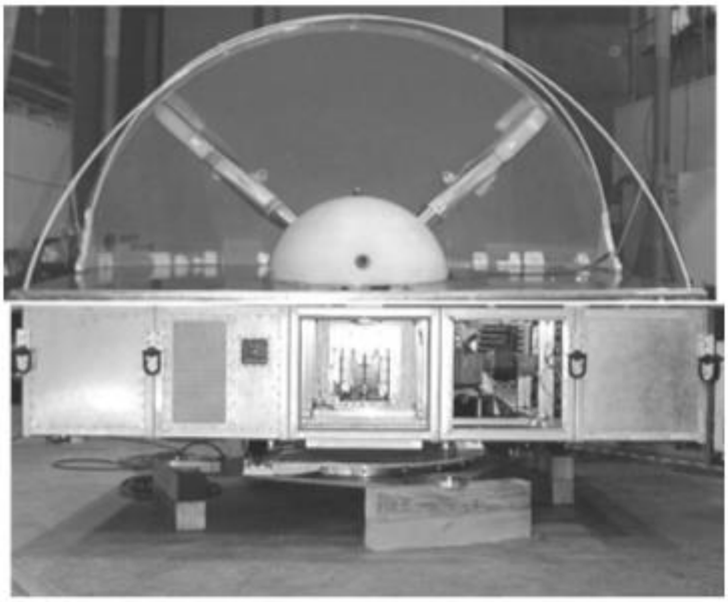

Figure 2.6: JOLT system [19]

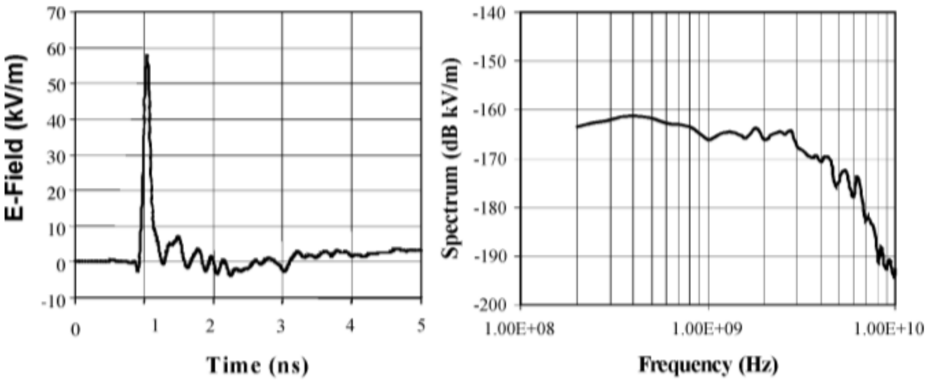

Figure 2.7: Output signal of the Jolt system and frequency spectrum [19]

The HPEM system was also built in Air Force Research Laboratory and realized with solid-state arrays. In this system, TEM horns, photo-conducting solid-state switches, and parallel-plate Blumlein line were used. The system, which operated with a charge voltage of 17 kV, reached 20 kV/m electric intensity at 10 m [21].

In 2007, a study explained an ultra-compact UWB pulse former system that could generate a bipolar pulse signal using a Blumlein line as a PFL [22]. In that study, the frequency spectra of bipolar and monopolar signals were examined, and it was observed that the bipolar signal has a broader frequency band, as given in Figure 2.8. As seen in Figure 2.8, the bipolar pulse does not contain DC components. The signal analysis required to feed an IRA was performed in [23]. Thus, after a few bursts, there is no residual charge left on the antenna. Thanks to the bipolar pulse with high-frequency components, more compact antenna structures could be studied.

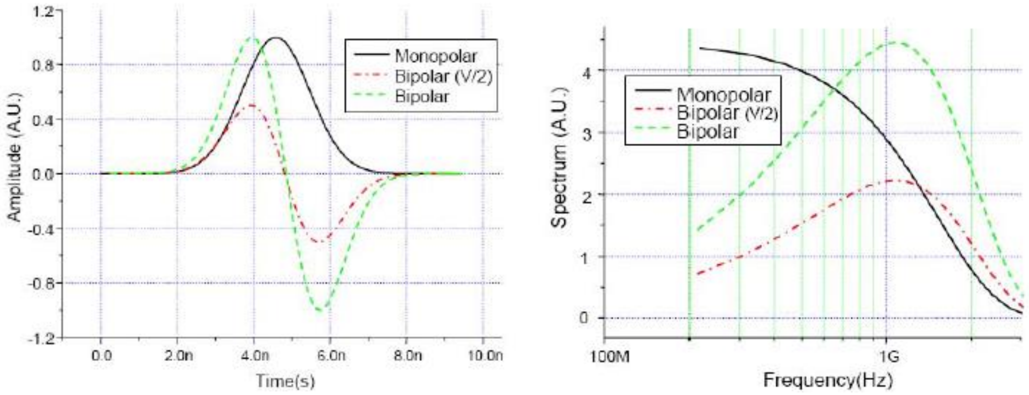

Figure 2.8: Monopolar and bipolar signal comparison [23]

The system described in [22] includes a biconical peaking switch and a grounding spark gap below 6 MPa. A Blumlein PFL is used to convert monopolar pulse to fast monocycle pulse. The Blumlein line is fed using a Marx generator with a rise time of less than 25 ns and a peak voltage reaching 650 kV. In the study to feed a TEM horn antenna, the first measurements were made by attaching an UWB 50-ohm equivalent load. In the measurements, 260 ps rise time and 500 MW output peak power were observed on the load.

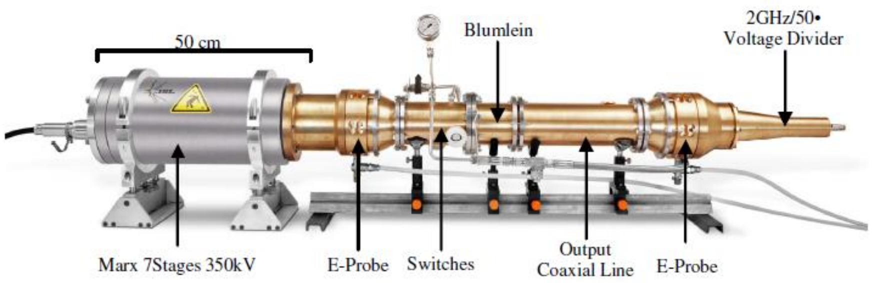

Figure 2.9: UWB system example [22]

In the system, a PFL with a length of 80 mm and a 50-ohm voltage divider for measuring used as described in Figure 2.9 [22]. The voltage signal measured on the probe is given in Figure 2.10. Peak-to-peak output signal reaching 200 kV has approximately 260 ps rise time.

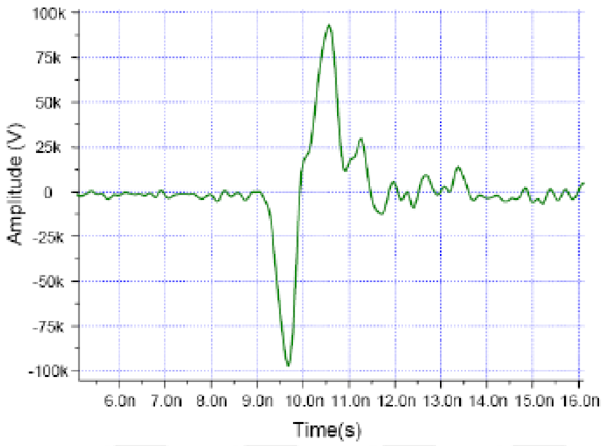

Figure 2.10: Output signal which is given in [22]

2.2 Marx Generators

A simple and widely used high-voltage impulse generator was proposed in 1925 by Erwin Marx for testing high-voltage components. If the operation of Marx generators is simply explained, the capacitors in the circuit are charged in parallel over high-impedance resistors and discharged in series over very fast switches. The signal obtained at its output has a rapid rise time. The peak value obtained from a Marx generator is equal to the product of the stages of the Marx generator and charging voltage. Despite of their simple working principle, when the behaviours of stray capacitance, inductance, and closing switches are included in the calculations, Marx generators are quite complex structures. A simple Marx generator circuit diagram is shown in Figure 2.11. As shown in this figure, spark gap structures are generally preferred as closing switches. In the following, a short survey on different designs of Marx generators and their application areas are presented.

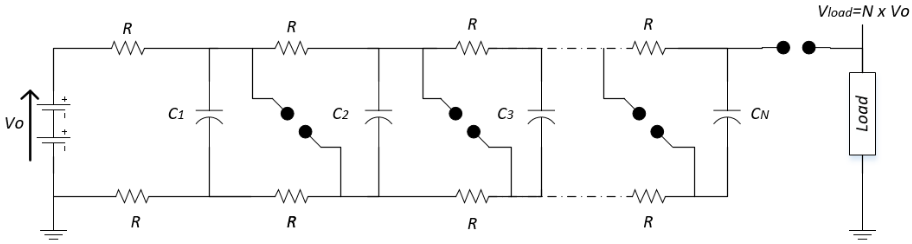

Figure 2.11: Schematics of a Marx generator

In [22], an 11-stage Marx generator was used to produce a pulse with a rise time of less than 10 ns and a charging voltage of 40 kV. Burst mode, which is especially needed in military areas, was reached using inductive charging instead of resistors in the Marx circuit. The output signal of a Marx generator can be compressed with a PFL which consists of a peaking capacitor and a spark gap. The Marx generator charges this capacitor, and thanks to the spark gap in the PFL, a pulse with a rise time of less than 1 ns can be obtained [22]. The authors of [22] also used a crowbar gap to sharpen the pulse. The sharpened pulse was transferred to the UWB antenna from the PFL output. High-power UWB electromagnetic signal was obtained across the antenna.

In [23], a charging inductor was used for repetitive operation, as shown in Figure 2.12. Spark gaps were designed using pressurized self-triggered switches with UV. Pspice simulation models were demonstrated, including stray capacitances. It is claimed that the use of high impedance charging resistors causes asynchronous charging of the stages. Electrodes with 12 mm diameters were used, while spark gap distances were set to 4 mm [23]. A voltage divider was used to measure the generator output signal. For this Marx generator, the charging voltage was 50 kV. The output signal changed with gas pressures ranging up to 0.35 MPa.

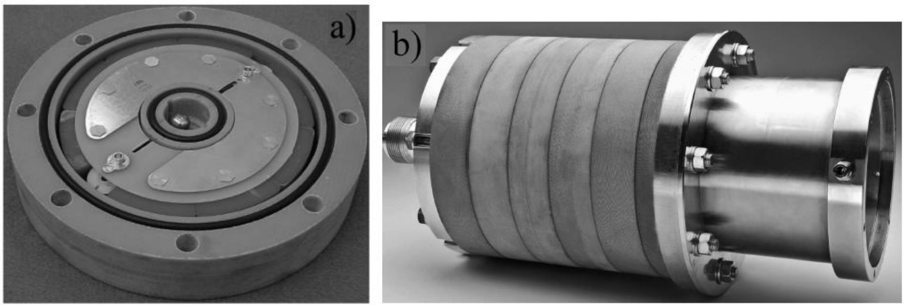

Figure 2.12: A compact Marx generator example [23]

In [24], an ultrafast coaxial Marx generator was realized without a peaking stage, as described in Figure 2.13. Specifically, by reducing the inductance in the system using a coaxial structure, and 800 ps fast rise time could be achieved. At the same time, the output current was measured by using a current viewing resistor (CVR). Exact electrode sizes and gap distances were used at every stage in the generator. The Marx generator trigger was tried to be stabilized by using a trigatron type spark gap in the first stage.

In [24], a Marx generator was used to drive HPM systems, such as virtual cathode oscillator. Measurements were carried out on a water load resistor instead of a vircator. Inductive charging was used to get fast rise time and this generator also had trigatron gap in the first stage. Burst mode was used for a repetitive system. In this study, the output voltage of the Marx generator was changing according to the load value, which is called load effect.

Figure 2.13: Marx generator structure example [24]

In [25], a generator with a maximum erected voltage of 4 MV is described, as also depicted in Figure 2.14. A dual polarity charging topology was used to reduce the source impedance. Spark gaps were filled with pressurized dry air.

The generator was made of ten stages with ceramic capacitors and a set of two home-made inductors vertically piled up in a cylindrical metallic tight enclosure filled with oil [26]. A vertical dry airflow, under low pressure, was used to keep the dielectric strength of the gaps constant. The simple trigger circuit ensured good stability in the triggering process of the Marx generator.

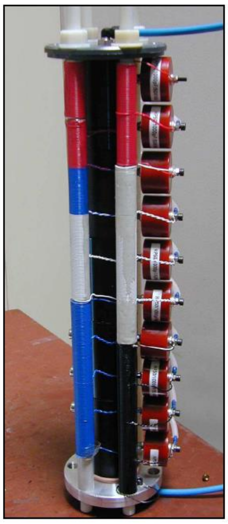

Figure 2.14: Marx generator example [26]

2.3 Pulse Forming Lines

PFLs are components that convert the signal from a pulse source (kV) with nanoseconds or microseconds pulse duration to a narrower pulse with a very fast closing switch. Two types of PFLs can be used to generate pulses at nanosecond levels. Specifically, PFLs can be designed in two different configurations, i.e., semiconductor-based and transmission-line-based. Pulse shaping is usually done with semiconductor based PFLs using semiconductor switching. Although these semiconductor pulse sources are not commonly available, they have sub-nanosecond pulse durations and they can produce pulses of several tens of kVs. Transmission-line-based PFLs consist of transmission lines and fast closing switch. The two most common types of these are Blumlein-line and single-line PFLs. The most important advantage point of these PFLs is that features, such as pulse duration, pulse amplitude and polarity are adjustable. A further advantage of a Blumlein line PFL is that the signal at the output is equal to the level of the charging voltage amplitude. A single-line PFL transmits only half of the charging voltage to the output, but it has a more straightforward structure than a Blumlein line PFL. Single-line PFL is studied in this thesis due to its simplicity.

In the literature, PFLs that are similar to each other but having small differences are studied. One example of single-line PFLs is a system designed to drive a corona reactor system for the aim of air purification, providing variable pulse duration in the range of 1-10 ns at its output [27], [28]. Telescopic antennas as outer conductors and ferrites in PFL are used for adjustable pulse duration. Pressurized oil insulated spark gap switch was used as a peaking switch. High-pressure oil flow was provided in PFL, as seen in Figure 2.15, and picosecond rise time was reached at the output signal. Figure 2.16 shows the oil spark gap structure used in this system [28], [29].

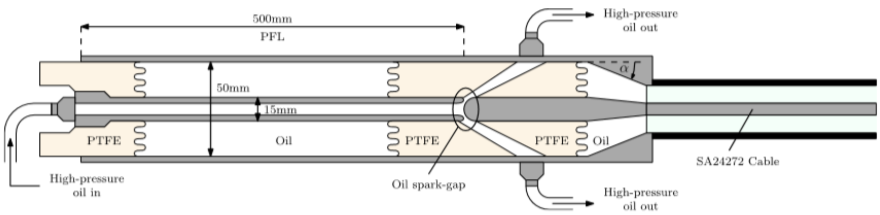

Figure 2.15: A PFL structure [28], [29]

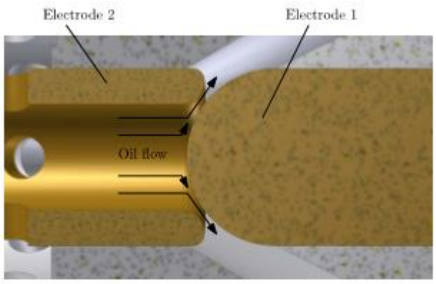

Figure 2.16: Spark gap configuration [28], [29]

Another study on PFLs is a system that drives Valentina antennas with a PFL and uses two gaseous spark gaps [30]. In this system, rapid rise time is first achieved using a peaking gap, and then the signal is cut off with a crowbar gap (or tail-cut switch) when it is at the peak value. Thus, the pulse duration is kept as short as possible so that an UWB signal can be observed. The output signal of PFL is transferred to the Valentine antenna by driving with 100 kV and 200 kV Marx generators, and the system can be seen in Figure 2.17 and Figure 2.18. With a peaking gap distance of around 1 mm, this PFL is 24 cm long and has a 50-ohm characteristic impedance. The spark gap range was insulated with hydrogen at 100 bar pressure. At the same time, rise time and pulse amplitude experiments were carried out by changing the pressure.

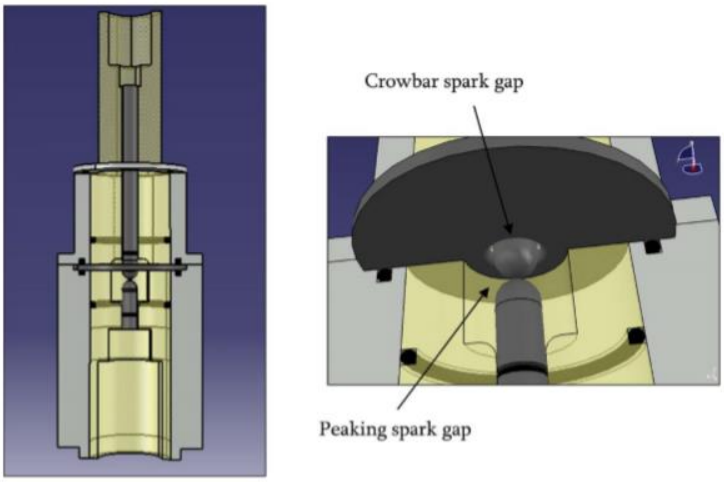

Figure 2.17: Spark gap and peaking gap example [26]

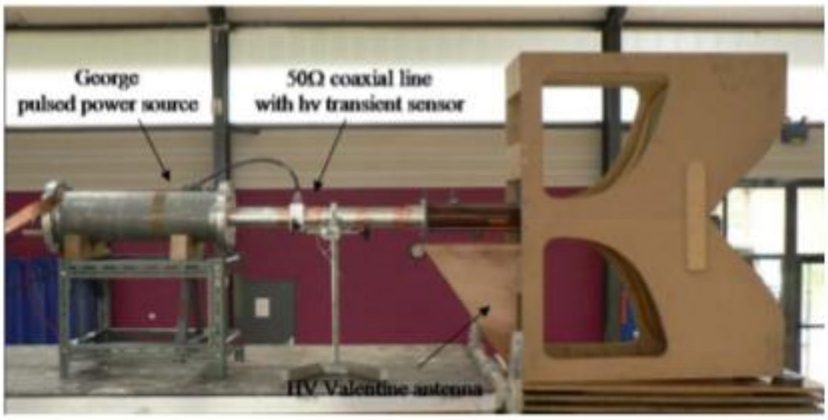

Figure 2.18: High amplitude electromagnetic pulse system with Valentine antenna [26]

In another study, PFL was charged with a repetitive Marx generator [26]. The spark gap environment was pressurized with 52 bar dry air, and a 310 kV peak voltage signal with 260 ps rise time was transferred to an UWB array antenna from the output of the PFL.

In some studies, two very-fast closing switches were used to generate very short pulse durations. The second switch, which can also be called crowbar gap or tail cut switch, allows the pulse duration to be adjusted [31]. Tail-cut switch was used in one of the systems designed for biological applications [32] and pulse duration was obtained at around 650 ps, while the tail-cut effect can be seen in Figure 2.19. In [33] and [34], a bipolar signal was obtained by driving a Blumlein line after a crowbar switch.

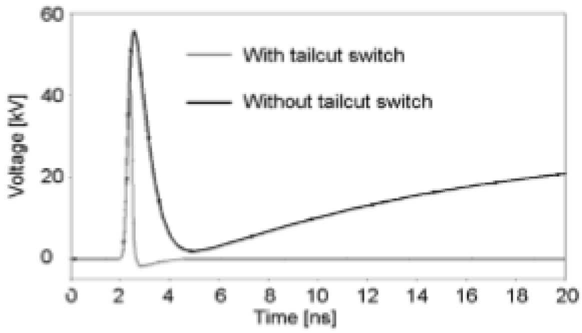

Figure 2.19: Output pulse of the system with and without tail-cut switch [32]

Since PFL simulations include spark gap switches, they are difficult to be solved with conventional electromagnetic solvers. One of the feasible approaches is given in [27], while another one is given in [35]. In the first approach, the spark gap was modelled as a current source, and the results were mostly compatible with the experiments. On the other hand, in [35], the spark gap was modelled as a step voltage source, which was compatible with simulated waveform experiment results. A high-voltage transient signal was transferred to a load using a spark gap with 0.2 mm distance and 30 bar nitrogen gas pressure [35]. The signal transferred from the PFL output to the load was measured by a capacitive divider patch mounted on the coaxial structure. The simulation model of the study is given in Figure 2.20 [35].

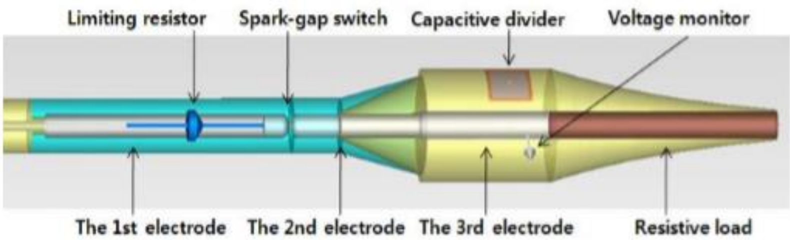

Figure 2.20: Simulation model of PFL [35]

2.4 Reflector Type Impulse Radiating Antenna

IRAs, which can be used in many areas, have different designs depending on the application areas such as UWB radars, biomedicine, and defense systems. One of the well-known defense IRA systems is the JOLT system [19]. A HIRA, fed with an amplitude above 1 MV, is powered by a transformer and an oil-peaking switch. This HIRA has 85-ohm input impedance, and the range product field is 5.3 MV across the antenna. Its rise time is around 130 ps. When using a full IRA, it requires a differential TEM feed to avoid common-mode currents on the feed plates. Full IRA can also be fed using balun, which converts single-ended source to differential feed. These problems can also be avoided by using HIRA. A peaking switch can be placed at the focal point, and HIRA can be fed directly from the peaking switch [19].

One of the most important works on IRA optimization was presented by Tyo [37], [38]. Change of feed impedance according to feed arm angle and plate widths was observed. Power-normalized gain, voltage-normalized gain, and prompt aperture efficiency graphs were created so that the feed arm angle and plate widths to be used for maximum gain are presented. The change of the optimum feed impedance graphic with respect to the feed arm angle was drawn, leading to a linear graphic.

One of the research topics on IRA is on changing the geometric shapes of the feed arm and trying to increase the gain and radiation efficiency. One of these studies used an inverse back-to-back Vivaldi feeding arm [40]. Time-domain simulations were performed to show that reflector efficiency can be increased to 35%. Also, the effects of the thickness and width of the feeding arms on the return loss and radiation efficiency were examined. The corresponding antenna and the results can be seen in Figure 2.21. It can be observed that the arm thickness affects the return loss to a large extent [39].

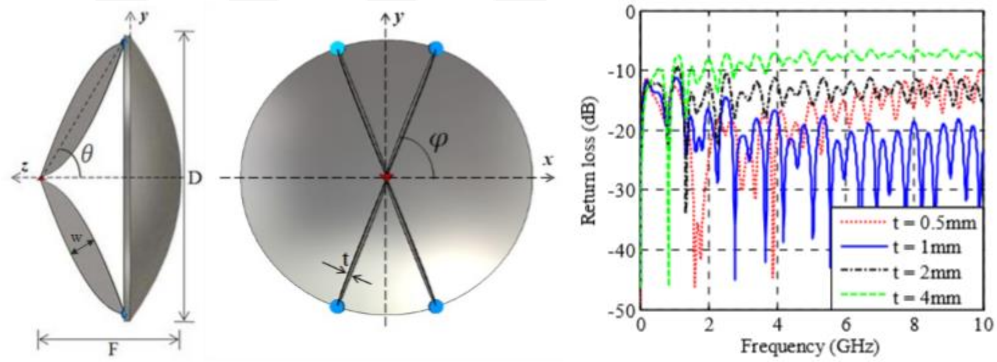

Figure 2.21: An IRA and the corresponding return loss graph [39]

Another study on the geometry of the feed arm can be found in [40] and [41]. A 100-ohm novel feed arm was designed without losing the gain of an antenna with a 120-ohm impedance. Feed arm geometry and IRA are illustrated in Figure 2.22. A balun with a splitter structure was also used in this study, as shown in Figure 2.23.

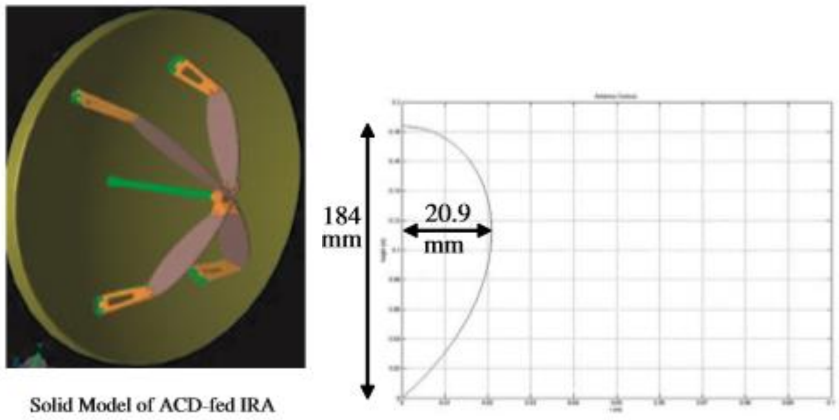

Figure 2.22: Feed arm geometry and solid model of ACD-fed IRA [40]

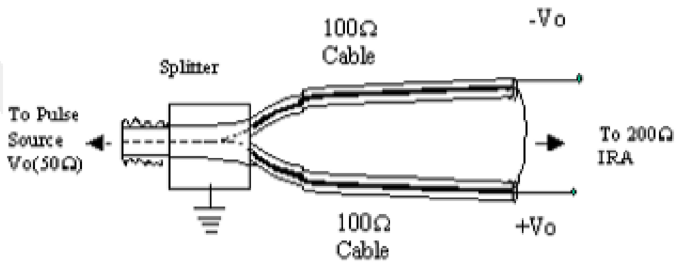

Figure 2.23: Splitter structure of the balun [40]

Another study on the termination load and arm tapering effects can be found in [42]. The larger circle of symmetry improves the gain. Considering current distributions, a standing wave effect is seen at the end of the feeding arms. Undesired energy is stored between the end of the feeding arms and the reflector [42]. Because of this stored energy, impedance has both real and imaginary parts. According to this study, standing waves cannot be removed by changing termination loads. To reduce the effects of the standing waves, however, the end parts of the feeding arms can be tapered, as shown in Figure 2.24

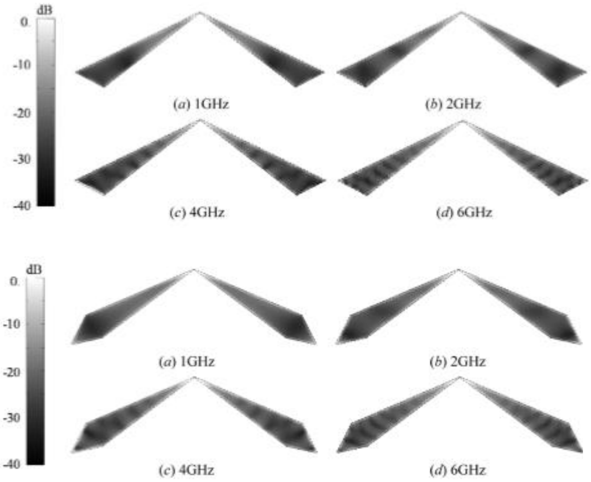

Figure 2.24: Different types of geometries for the feed arms and the corresponding standing wave images [42]

One of the prominent works on IRA feeding [43] demonstrates an IRA with 1.52 m diameters for a radar application. Since it was not possible to use a sharpening switch at the apex to drive the antenna with a large diameter of the 100-ohm cable, the use of splitter balun was presented. The manufactured IRA is shown in Figure 2.25. Unlike previous designs, cross-polarization effects were tried to be reduced by using a ground plane in a horizontal plane.

Figure 2.25: An IRA example with 1.52 m diameters [43]

The IRA was fed with a 100-ohm RG-213 cable using a high-voltage splitter. Splitter balun can be seen in Figure 2.26.

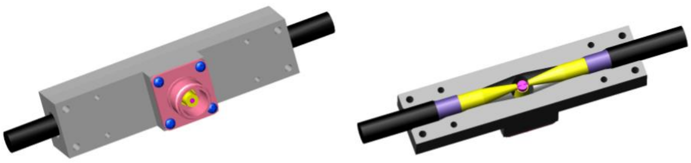

Figure 2.26: High-voltage splitter [43]

Splitter balun has two equal cables, and it is connected in series with the connector and in parallel with the IRA. The connection of the splitter balun behind the reflector can be seen in Figure 2.27.

Figure 2.27: Feeding the IRA with splitter balun [43]

Another interesting study is a collapsible antenna produced from a very tough conductive mesh fabric, which it can be seen in Figure 2.28 [44], [45].

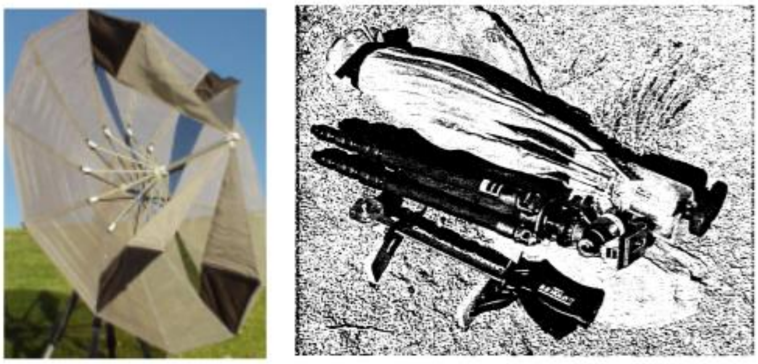

Figure 2.28: IRA produced by using conductive mesh fabric [44], [45]

Another IRA-feeding study tried to connect a broadband impulse generator to the antenna input with a tapered transmission line, as shown in Figure 2.29 and Figure 2.30 [46]. In the study with a frequency range from 50 MHz to 1 GHz, two different geometries for the tapered transmission line were exponential and logarithmic.

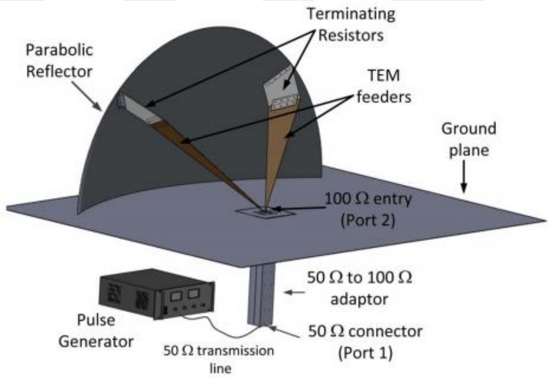

Figure 2.29: Half IRA with tapered transmission line [46]

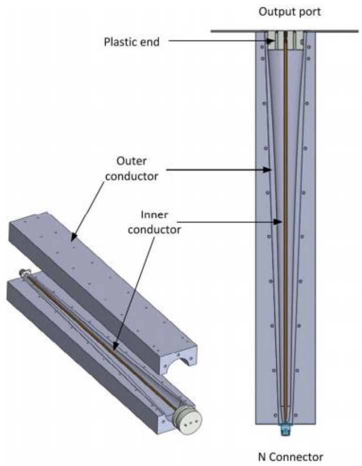

Figure 2.30: Tapered transmission line [46]

Another optimization study involved 150-ohm conical-plate reflector IRA optimization is given in [47]. In this study, the concept of a splitter and balun combination based on a directional coupler for feeding the antenna was presented. A three-port splitter-balun was used to feed the IRA with 50-ohm input impedance and 75-ohm output impedance. Splitters were lossy as they were based on resistor dividers [48]. The two ends at the output of a splitter were carried to the focal point with identical cables.

2.5 Balun

UWB transitions have started to be of interest in recent years due to their application areas (5G, radar, etc.). Planar transitions or Marchand baluns are often used to feed unbalanced UWB antennas, such as log-periodic or frequency-independent antennas [49], [50]. The exact analysis of Marchand balun was given by Cloete [51], [52]. However, these planar transitions may cause losses in connections with antennas. Cutting a coaxial line at certain angles, making it slotted, and using it as a UWB transition was first presented by Duncan and Minerva in 1960 [53]. This was achieved by removing a particular part of the outer jacket of the coaxial line during the transition. Foster also studied the upper and lower limits of impedance for different heights of this balun using MoM [53]. This type of transition was used to feed a TEM horn antenna [55], [55], and [57], as shown in Figure 2.31. At the same time, the optimal taper model for the transition was presented by Klopfenstein [58].

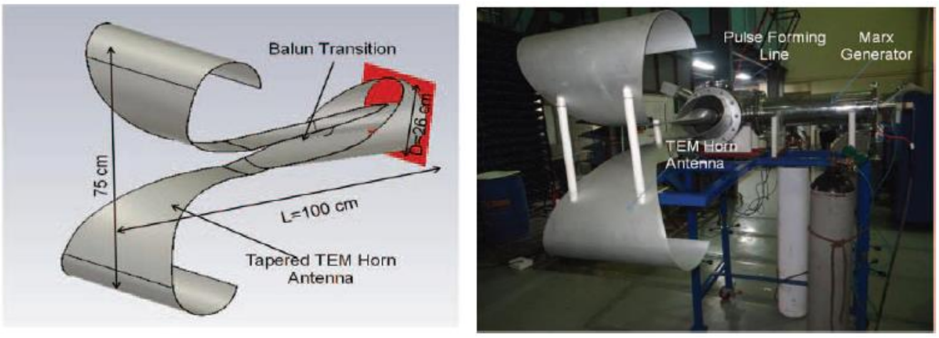

Figure 2.31: A tapered TEM horn antenna with a balun transition [57]

2.6 High Voltage Pulse Measurement

It is known that a measurement of high-voltage transient signals cannot be carried out easily with standard commercial products, and even conferences specific to this subject have also been arranged [59]. After discussed in the open literature in the 1980s, fast transient signals at kV and MV levels were measured [60]. Again, there have been similar studies on the subject in the literature [60], [62]. The measurement system should be resistant to high-voltages and have a wide band. Although there exist few commercial products [63], [64] that can be accessed, they are expensive, while each system has a different operating frequency.

For this reason, hand-made probes such as D-dot, B-dot probes [65], [66], capacitive voltage dividers, current viewing resistors, Rogowski coils, or electro-optics, which are resistant to high power and high-frequency levels, are used. These probes, which generally operate based on a capacitive divider, are preferred since their materials are easy to access and calibrate. If it is desired to measure a transient signal on a coaxial structure without breaking the line, the probe is mounted on the outer conductor. It is possible to obtain a capacitive divider using two small patches and a very thin dielectric sheet [35].

Capacitive dividers operate in integrating mode or differentiating mode according to the frequency band [67]. One of the descriptive studies on this subject in recent years is the handmade B-dot and D-dot high-voltage and high-current sensors described in [28], [68], [69]. The designs were very compact, inexpensive, and wideband. They are simply constructed for measuring current and voltage over the coaxial structure with SMA connectors. The sensors are calibrated with a vector network analyzer (VNA) and a commercial voltage pulse generator. Measurement result is available only after a short signal processing step. Meanwhile, 3D electromagnetics simulations are mostly compatible with high frequencies. The sensors that can be seen in Figure 2.32 have a clamp structures and they can easily be mounted on a coaxial structure.

Figure 2.32: D-dot and B-dot probes designed in study [28]

One of the similar studies in recent years [69] performed 3D simulations and it was on how to position a probe on a coaxial structure and how close it will be to the peaking switch on the PFL. Snapshots of the study can be seen in Figure 2.33. It was found that, distortion occurs in the probe signal if the probe is mounted very close to the closing switch [69]. Usually, V-dot probes can be made on the coaxial structure with SMA or N-type connectors or adapters [69], [69].

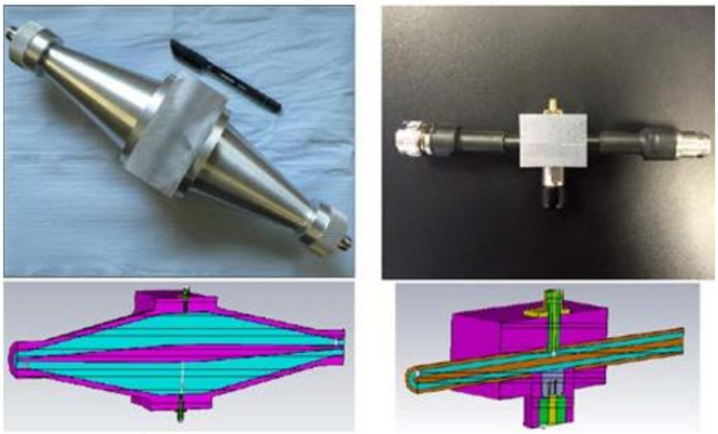

Figure 2.33: V-dot probes [69], [69]

An example of the V-dot probe's transfer function produced in [69] is given in Figure 2.34. Using a logarithmic horizontal axis, a linear graph is obtained.

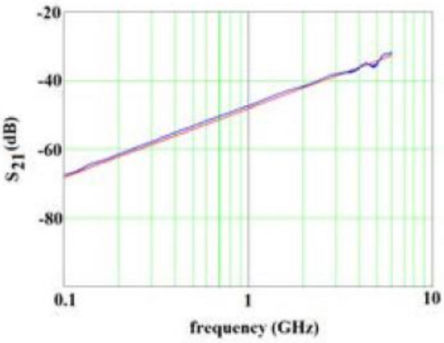

Figure 2.34: Transfer function of the V-dot probes [69]

2.7 Conclusion

In this section, literature on the subject is first summarized, considering similar systems. Marx, PFL, IRA, balun, and V-dot probe are provided individually. In the first stage, similar systems and output signals were examined and a literature is reviewed for designs and components that can be used in this study. As can be seen, Marx generators can be used in different configurations in UWB systems. In these generators, the reliability of Marx generators is tried to be increased by using different pressurized gas or oil systems. It has been seen that resistors or inductors are used for Marx generators in repetitive systems. After Marx generator, which is an impulse generator, it was observed that a very fast pulse signal was tried to be created with transformers or different types of PFLs. It is seen that the coaxial type PFL is generally designed after the Marx generator. This component is important because it determines the output signal rise time and pulse duration. It is usually designed with pressurized gas or oil. Different IRA designs are also examined in this section. It was seen that there are different antenna configurations such as half and full IRA. Half-IRA is easy to feed but has an asymmetric radiation pattern. Feed arm designs in different geometries were observed for optimization studies. For the high-voltage pulse measurements, home-made V-dot probes were examined. The probe which operates on the capacitive voltage divider principle was seen to be suitable for UWB and high-voltage applications.

CHAPTER 3

THEORY OF OPERATION

3.1 Marx Generators

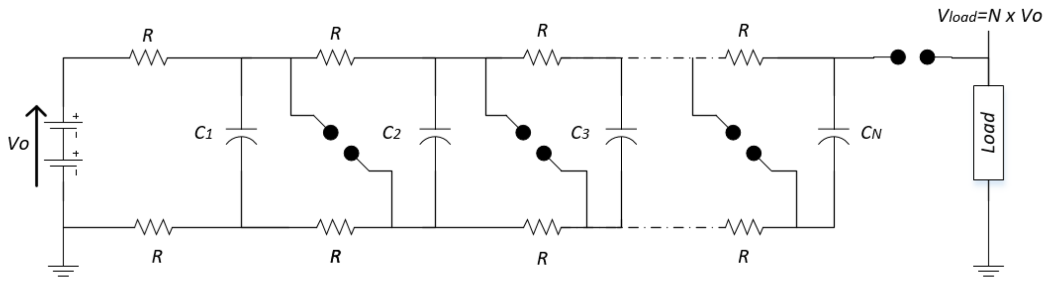

Figure 3.1: Marx generator circuit schematics

Using RLC components and spark gap structures, Marx generator generates an impulse voltage signal that rises rapidly at its output and reaches high-voltage levels. With a DC source at the input, capacitors in a parallel structure are charged to V_0 via charging resistors. When the breakdown voltage of the spark gaps is reached, the spark gaps close very quickly, shorting the resistors in the circuit, while the capacitors are discharged in series. Briefly, it is a voltage-multiplying circuit that charges capacitors in parallel and discharges them in series. Switching the capacitors from parallel to serial is known as “erecting the Marx” or “Marx Discharging” [67]. As seen in Figure 3.1, a “stage” consists of a capacitor, a resistor, and a switch. Capacitor and resistor values in each stage are equal. Switches are usually gas insulated or oil-insulated spark gaps. Charging resistors play two essential roles: Capacitors are charged via resistors during a charge period, while high-impedance resistors force the current to flow through spark gaps during a discharge. Therefore, resistance values are chosen from kΩ to MΩ levels to limit the current.

Because Marx generators are fast generators, they can be used in repetition mode. In a repetition mode, which is especially important in military areas, a high repetition rate can be achieved using inductors instead of resistors. Inductors can also be used as isolation impedances.

The output signal shape and amplitude produced by a Marx generator depend on to the load. In this thesis, a PFL is used as a load of the Marx generator. Capacitance calculations and effects of PFL, which shows capacitive load effect, are described in the next sections.

3.1.1 Charging Marx Generator

When charging a Marx generator, N capacitors with equal C_0 capacitances are charged to V_0 voltage through charging resistors. We can define the capacitances as,

$$C_1 = C_2 = \cdots = C_N = C_0 \,. \qquad (1)$$

On the other hand, capacitors cannot be charged at the same time. The charging time of the capacitor at the nth stage is given as [71], [72].

$$\tau_{ch} = n^2 R C_0 \text{ , where } 1 \leq n \leq N. \qquad (2)$$

At the end of a sufficient time, the voltage will reach V_0 at the last stage. While charging, the Marx generator equivalent circuit diagram can be drawn as in Figure 3.2.

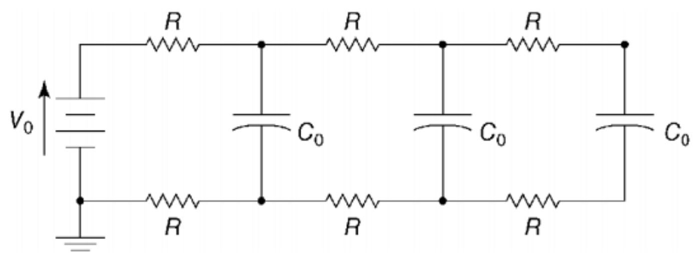

Figure 3.2: Marx generator circuit diagram during charging [67]

Charging time is critical, since electrical stress on the Marx generator's insulation may cause insulation failure for long charging periods. Therefore, as an important parameter, the minimum charging time can be determined by the voltage differences between the first and last capacitors [67], [73]. One can obtain (see in Figure 3.3.).

$$\frac{\Delta V_c}{V_c} = \frac{N^2 R C_0}{T_m} \; where \; \Delta V_c = V_{C,N} - V_{C,1}. \tag{3}$$

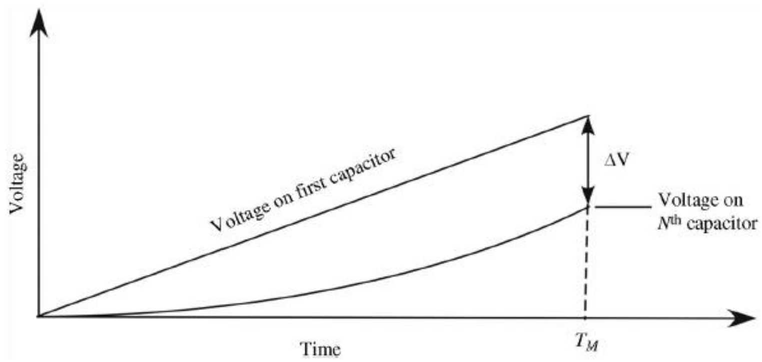

Figure 3.3: Voltage differences between the first and last capacitors [67]

When the last capacitor is charged to approximately V_0 voltage, the total energy stored in the Marx generator can be calculated approximately as [67], [73].

$$E_{marx} = \frac{1}{2} N C_0 V_0^2 \, . \tag{4}$$

In the above, NC_0 comes from the parallel combination of capacitors. The stored energy is lower than the value given in (4) since some of the energy is spent on the resistors during charging.

3.1.2 Marx Discharging

A Marx discharging process occurs when the spark gaps are opened sequentially, bringing capacitors from parallel to serial circuit configuration. Marx discharge is initiated due to the increased voltage in the remaining stages after the first spark gap is fired. The non-simultaneous breakdown of the spark gaps decreases the amplitude of the output voltage and distorts the waveform, as shown in Figure 3.4. It is called "overvolted" when the voltage on a spark gap exceeds the DC self-breakdown value. Spark gap overvoltages are essential for the stability of the Marx generator.

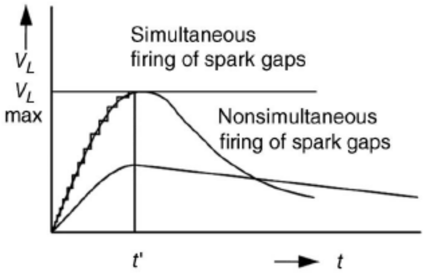

Figure 3.4: Output voltage of simultaneous & non-simultaneous firing of spark gaps [67]

When the switches on all stages are closed, the circuit model of the Marx generator is as shown in Figure 3.5.

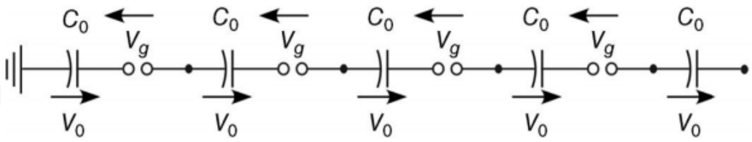

Figure 3.5: The circuit model of a Marx generator while discharging [67]

In an ideal Marx discharging process, if the stray inductance of switches, connections, and capacitors are included, an equivalent Marx discharging circuit can be shown simply as in Figure 3.6. Marx equivalent discharging inductance is given as

$$L_{marx} = L_{spark\ gaps} + L_{capacitors} + L_{stray}\,. \tag{5}$$

The equivalent capacitance during a discharge can be found as

$$C_M = \frac{C_0}{N}\,. \tag{6}$$

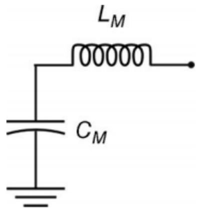

Figure 3.6: Equivalent circuit schematic during discharge [67]

The discharge cycle and the output signal shape of a Marx generator are mostly dependent on the load impedance. As the Marx generator charges PFL in this study, the corresponding load impedance has a capacitive property; so $C_M >> C_{Load}$ case will be discussed.

3.1.3 Discharging on Capacitive Loads

It is crucial for Marx generators to drive capacitive loads in pulsed power and pulse compression systems. A charged capacitor can transfer almost all its energy to an uncharged capacitor through an inductor. Peaking capacitor architectures form the basis of multi-GW pulsed power machines [67].

Energy transfer to a capacitive load from a Marx generator is shown as in Figure 3.7. The inductance given in Figure 3.7 may be the Marx generator's internal inductance, or an extra installed inductor. When the spark gap breaks down, energy on C_M is transferred to C_2 via L_M

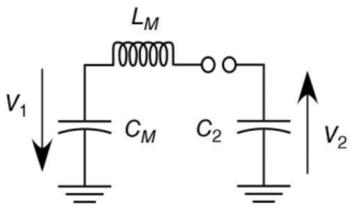

Figure 3.7: Equivalent circuit schematics of the Marx generator while charging capacitive loads [67]

If the initial voltage of C_M is accepted as V_i, then Kirchhoff's law can be used to derive,

$$V_M(t) - L\frac{di}{dt} = V_2(t)\,. \tag{7}$$

$$V_M(t) - V_i = \frac{1}{C_M}\int i(t)\,dt\,. \tag{8}$$

$$V_2(t) = \frac{1}{C_2}\int i(t)\,dt\,. \tag{9}$$

Considering also initial conditions, these equations can be solved to arrive at [67],

$$V_2(t) = \frac{V_i C_M}{C_2 + C_M}(1 - \cos(\omega t)). \tag{10}$$

When $C_M >> C_2$, this is known as a peaking circuit. Energy transfer is performed when (1-cos(ωt)) = 2, and by neglecting C_2 in the upper equation, we obtain

$$V_M\left(t = \frac{\pi}{\omega}\right) \approx V_i \quad \& \quad V_2\left(t = \frac{\pi}{\omega}\right) \approx 2V_i\,. \tag{11}$$

The voltage of the peaking capacitor reaches twice the voltage of the Marx generator, while the voltage of the Marx generator capacitors remains almost the same. This situation is shown in Figure 3.8.

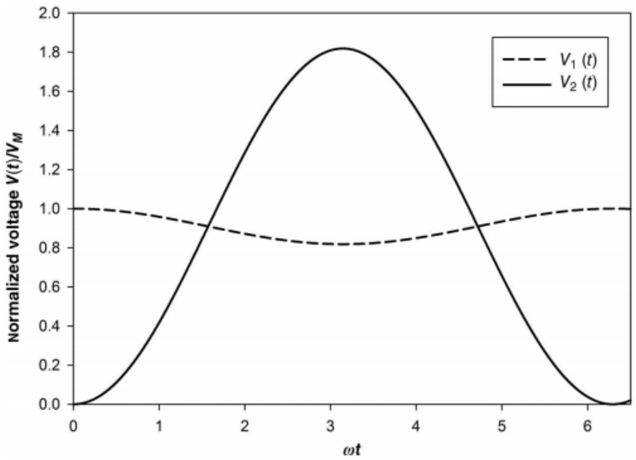

Figure 3.8: The voltages on the peaking capacitor and Marx generator [67]

3.1.4 A Peaking Capacitor Driving a Resistive Load

A peaking capacitor is used to have a faster rise time in the output of a Marx generator. The voltage can then be transferred to a resistive load with the help of a peaking switch. The equivalent circuit of this situation is given in Figure 3.9.

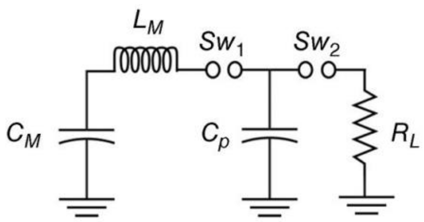

Figure 3.9: Equivalent circuit of a peaking capacitor driving a resistive load [67]

If the value of the peaking capacitor is selected as in,

$$C_p = \frac{L_M C_M}{L_M + C_M R_L^2} \tag{12}$$

a high-voltage pulse with a fast rise time can be transferred to the load [67].

3.2 Pulse Forming Line

In pulsed power applications, transformers, Marx generators, and Tesla coils can be used as primary energy sources to obtain very high voltage values in the form of pulses. However, since the rise time of a pulse obtained at the outputs of these generators is not short enough, it is difficult to reach high frequencies in the frequency domain. Therefore, a unit is needed to accelerate the output signals of these generators. For this purpose, a PFL unit consists of a capacitor, and a very-fast closing switch. Consisting of these components, such a structure can be charged in microseconds by a high-voltage generator, such as a Marx generator. Then the energy is transferred to the load with the closing switch. The charging time of the peaking capacitor is much shorter than the discharge time of the Marx generator. Dielectrics are exposed to very high electrical stress, but they have high breakdown strengths so that high charge levels can be achieved [67]. The gap distance of the peaking switch, which usually uses gas pressure or oil insulation, is very small (<1 mm); so the rise time of the signal transmitted to the load can be reduced to several hundred picoseconds. Thus, on the load, frequencies can be seen in the MHz to GHz ranges. A peaking capacitor can be designed by using lumped elements or transmission lines.

In pulsed power applications, since the pulse signal carries many frequency components, the fundamental frequency f_0 of a signal with t_p duration can be found as

$$f_0 = \frac{1}{t_p}. \tag{13}$$

The highest frequency is determined by the rise time of the pulse [67]. According to the electrical length of the signal, the network type can be decided to be a lumped element or a transmission line. In many pulsed power applications, the circuit is treated as a transmission line since the pulse duration is less than 1 ms.

3.2.1 Coaxial Type Pulse Forming Line

Coaxial type PFLs are among the most used PFLs in pulsed power applications. Generally, by adding a closing switch to a coaxial transmission line, such a structure can be created [67], as shown in Figure 3.10. With the closing switch on the coaxial PFL, the primary energy source sees this structure as a cylindrical capacitor (C_p) and charges it to V_0 voltage. The spark gap turns off when the PFL voltage reaches V_0 and transfers the charge with $V_0/2$ amplitude on the load. The electrical breakdown strength of the dielectric used in this coaxial structure limits the voltage that can be charged. C_p, line characteristic impedance, pulse width, dielectric strength, and dispersion determine the dimensions of the structure.

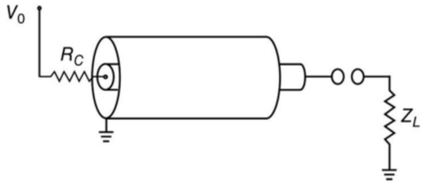

Figure 3.10: A coaxial PFL with a spark gap and resistive load [67]

The characteristic impedance of a coaxial transmission line can be calculated as

$$Z_0 = \frac{1}{2\pi}\sqrt{\frac{\mu}{\varepsilon}}\ln\left(\frac{D_o}{D_i}\right). \tag{14}$$

D_o and D_i indicate the outer and inner diameters, L indicates the length of the coaxial, μ and ε indicate the properties of the dielectric used. The capacitance of a cylindrical capacitor can be found as

$$C_p = \frac{2\pi\varepsilon L}{\ln\left(\frac{D_o}{D_i}\right)}. \tag{15}$$

Furthermore, the velocity of propagation in the PFL can be calculated as

$$v_p = \frac{c}{\sqrt{\varepsilon_r \mu_r}}. \tag{16}$$

The pulse duration is determined by the length of the PFL and the magnetic properties of the dielectric material used inside the coaxial structure. The pulse width can be found as

$$\Delta t = \frac{2L}{v_p}. \tag{17}$$

The dielectric strengths of the insulators which are given in the literature are generally used for DC voltage levels. However, in the case of a pulse, the dielectric strength usually increases. Specifically, the dielectric strength of the insulator for a ns pulse is higher than E_{max} .When the dielectric strength of the insulator is E_{max}, the maximum charging voltage can be calculated as [67]

$$V_{max} = E_{max} D_i \ln\left(\frac{D_o}{D_i}\right). \tag{18}$$

The structure before the spark gap in PFL acts as a peaking capacitor and is charged to V_0voltage by the Marx generator. Meanwhile, the electric field intensity between the spark gap electrodes increases, and the spark gap switch turns off. Then the peaking capacitor transfers half of its charge to the matched line connected to the load. As stated in the literature, the wave at $-V_0/2$ amplitude propagates from the end of the capacitor to the Marx generator and reflects back as it sees an open circuit here [27]. This situation can be seen in Figure 3.11.

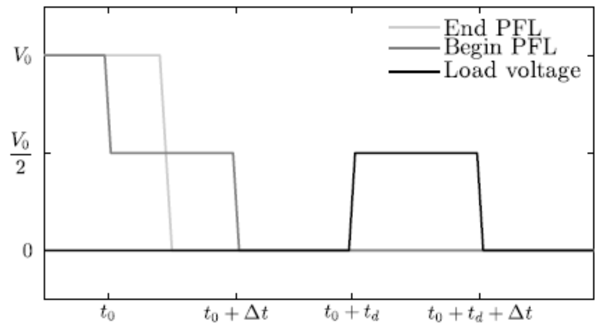

Figure 3.11: Sketch of the waveforms in a PFL [27]

3.2.2 Dispersion

One of the most critical factors causing distortion in output pulse shape is dispersion. Electromagnetic waves should propagate only in TEM mode in the coaxial PFL. Since the excitation of different modes in the coaxial line causes dispersion [27], the maximum operating frequency should be below the cut-off frequency to avoid higher-order modes. In the coaxial line, the cut-off frequency limits the inner and outer conductor diameters. The first higher-order mode that propagates in a coaxial line is the TE_{11} mode. The cut-off wavenumber and frequency can be calculated as [48].

$$k_c = \frac{2}{D_o + D_i}. \tag{19}$$

$$f_c = \frac{ck_c}{2\pi\sqrt{\varepsilon_r}}. \tag{20}$$

Higher values for the cut-off frequency can be achieved by using small diameters. However, if the inner and outer conductors are close to each other, the increasing electric field intensity between them may cause electrical breakdowns.

3.2.3 PFL Switching

The pulse rise time determines highest frequency of the output signal, while the pulse duration determines the fundamental frequency component. Wider bandwidth can be obtained with faster pulse rise times and shorter pulse durations. The rise time of the output voltage depends on the spark gap distance used in the PFL, the shape of the electrodes and the insulation material used in this gap. Since they affect the pulse shape, positions of closing switches are critical for pulsed power applications. They are used in these applications due to their high-voltage resistances and fast operations. The most common high-voltage and high-current switches are pseudo-sparks, thyratrons, solid-state switches, spark gaps, and ignitrons [67].

3.2.4 Spark Gaps

A spark gap usually formed by separating two conductive electrodes with an insulating medium. This insulation medium can be gas, liquid, or vacuum. Unless the voltage applied on the electrodes exceeds the threshold value, it behaves like an open circuit. Hence, when the voltage between the gaps is below the threshold value, the spark gap has a stray capacitance and very high resistance. When the threshold value is reached, however, breakdown occurs in the gap, and the insulating media turns into a conductive line. Meanwhile, the resistance in gap drops rapidly, allowing current to flow. An example to an arc form and a spark gap can be seen in Figure 3.12.

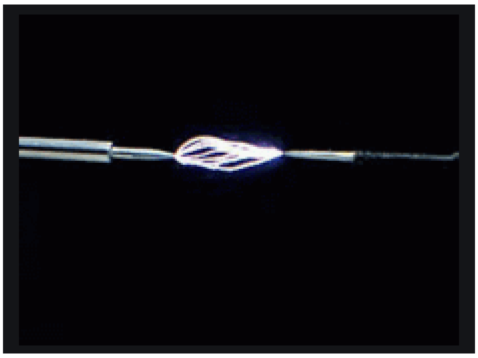

Figure 3.12: An example of a spark gap

In addition to the one described above, the breakdown can be initiated with external factor like an electron beam or a laser beam. Such triggered spark gaps can be used to increase switching time and reliability. The breakdown voltage varies depending on whether the applied voltage is DC or AC. For example, it is around 10 kV/cm when the insulating medium is atmospheric air, while it is around 20 kV/cm when oil or pressurized gas is used [67].

When *Sw* is open, it acts as a spark gap capacitor. When the spark gap breaks down, the self-capacitance is paralleled by the resistance and the channel inductance. In the Figure 3.13, L_{gap} and R_{gap} represent the inductance and resistance of the arc channel. In this equation A is the surface area of the electrodes and d is the gap distance in meter, then spark gap capacitance can be calculated as (21).

$$C_s = \frac{\varepsilon\, A}{d}\ F \tag{21}$$

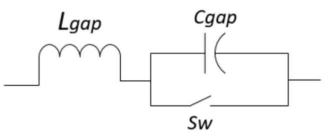

Figure 3.13: Equivalent circuit of the spark gap

The resistance and inductance calculations for a spark gap arc channel are relatively complicated. The channel inductance increases as the gap distance increases. In a PFL, the peaking gap distance is chosen as small as possible since the rise time of the output signal is largely determined by the inductance of the spark gap arc channel. High-pressure gases (SF_6, N_2, etc.) or transformer oil can be used to increase the dielectric strength since electrodes are very close to each other at high voltages.

Electrode erosion is very important in pulsed power applications, especially for systems operating in repetition mode. After a certain number of shots, erosion occurs on the electrode surfaces, and since it damages the smoothness of the electrode surfaces, it disrupts the electric field distribution in the gap, leading to decrease in reliability.

3.2.5 Spark Gap Insulation Medium

Spark gap insulation medium can be gas, liquid, solid, and even vacuum. The most important factor for the used material is its reliability and lifetime. The most frequently used materials are pressurized gases and transformer oil. Due to its electronegativity and high electrical breakdown feature, SF6 gas is widely used, while gases such as N_2, H_2, and Ar are also very common. These gases are used at high pressures (2 to 10 MPa) to increase the dielectric strength [74]. Gas mixtures can also be used.

Vacuum spark gaps can be used, although not as common as gases. Disadvantages of these media are statistical delay times and large deviations in jitter. But very fast rise times can be achieved with this medium.

The use of oil is also quite common in spark gap studies [75], [76]. This easy-to-find material needs to be cleaned frequently, and moderate oil pressure is required. The breakdown voltage of spark gaps can be significantly large, but it can vary according to the applied voltage signal, medium insulation, gap distance, electrode material, and electrode geometry [77], [78], [79].

Transformer oil was used in this study, as it is easy to find, and the mechanical design required for sealing is not challenging. DC breakdown strength for transformer oil is about 60 kV/mm and this value further increases for pulsed electric fields [27], [80]. At the same time, transformer oil is preferred to match the EM environment in the line since its dielectric constant is close to the dielectric constant of PTFE used in the coaxial structure.

3.3 Impulse Radiating Antenna

An IRA consists of a reflector, 4 feed arms, and termination components. The spherical wave that moves over the feed arm is reflected from the reflector and converted into a plane wave. During excitation, a voltage difference occurs between feed arm pairs. The induced surface currents on the feed arms move from the focal point to the reflector along edges. This situation causes spherically symmetric TEM wave between arms with different potentials. Meanwhile, non-radiating energy is dissipated, thanks to the terminations between the reflector and feed arms. This dissipation minimizes the reflections of the TEM wave. A conventional IRA can be seen in Figure 3.14. In the figure, F indicates the distance of focus, while D indicates the diameter of the parabolic reflector.

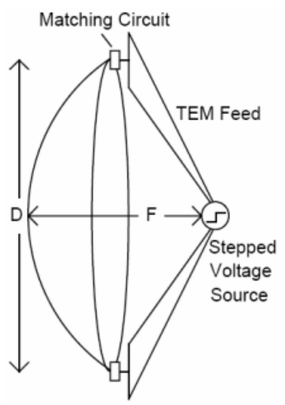

Figure 3.14: A conventional IRA [80]

IRAs are antennas particularly designed to make UWB electromagnetic impulse radiation. These antennas can also be characterized as dispersionless. Bandwidth rates (f_{high}/f_{low}) of the output signal can reach 100. These antennas behave like differentiators because they have non-dispersive TEM feed structures focused apertures.

In general, the radiated electric field is the derivative of the input voltage signal applied to the antenna. If $V(t)$ is the excitation signal, V_o is the peak value of the excitation signal, and S_a is the aperture surface, the radiated electric field signal can be found as

$$E_{rad}(r,t) = \frac{\int_{S_a} E(x,y)\, dxdy}{V_o 2\pi rc} \frac{dV(t)}{dt}. \quad (22)$$

The idealized step response of an IRA is as in Figure 3.15. Due to the direct radiation of the current on the feed arms, a prepulse occurs at 2F/c [81].

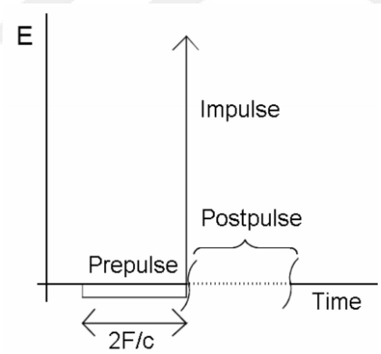

Figure 3.15. Radiated electric-field pulse signal radiated from an IRA [80]

3.3.1 Feed Arms

In an IRA, impedance matching is mostly provided by feed arms. When the impedance is not matched, some of the transferred power returns and causes loss. Feed arms start from the feed point and act as a transmission line extending towards the reflector. The most important physical parameter affecting the characteristic impedance of the feed arms is the angles between them. Hence several factors appear in the optimization and design of feed arms, like the expansion angle of the arms or the angle of the arms towards the reflector, as illustrated in Figure 3.16.

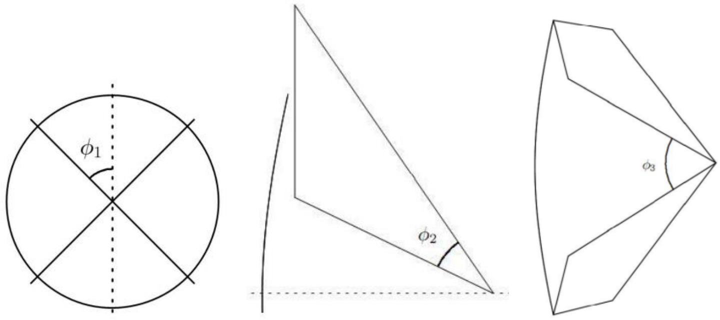

Figure 3.16. The angles involved in IRA feed arms [82]

A wide variety of examples in the literature on the geometric features of feed arms are presented in the previous chapter. In this thesis, mostly conventional IRAs, i.e., conical feed IRAs, are studied. A conventional IRA has a 45-degree feed arm angle with a vertical symmetry line. However, the angle can be changed to obtain different gain values according to the input impedance. For example, better gain values can be obtained for 30-degrees angle [84], [85]. The characteristic impedance of the conventional IRA is defined as [38]

$$f_g = {}^{Z_{line}}/_{Z_{med}} . \tag{23}$$

f_g denotes the geometrical impedance factor and Z_{med} denotes the free space impedance. The geometrical impedance factor can further be calculated with complete elliptical integrals $K(m)$ [85]. In these calculations, m is determined by the geometry of the feed arms as

$$m = \frac{b_1^2}{b_2^2} \qquad f_g = \frac{K(m)}{2K(1-m)} . \tag{24}$$

b_1 and b_2 are as defined in Figure 3.17 [37], [38].

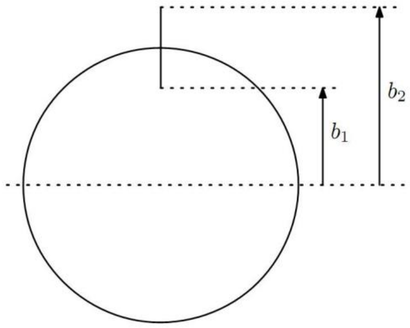

Figure 3.17: Two parameters of the reflector [82]

Using the optimization study given in [37], an IRA can be designed by finding b_1/a ratio for the desired feed impedance, a is the radius of the reflector. In [37], different plate widths vs. feed arm angles ϕ_1 are given for various feed impedance values.

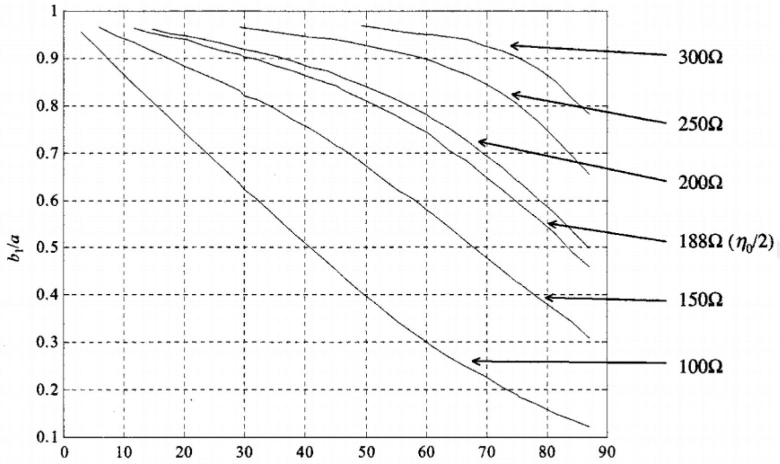

Figure 3.18: Different plate widths vs. feed arm angles for various feed impedance values [37]

However, S_{11} parameter is not taken into consideration in [37]. In addition, the distance of the feed arms in the focus is not considered. Feed height has also great importance in high-voltage systems. Because if the upper and lower plates are close to each other, there is a higher risk of electrical breakdown.

3.3.2 Reflector

The most dominating elements in an IRA are feed arms and the reflector. Using a simple description, a parabolic reflector is a surface that reflects spherical waves and transforms them into plane waves, as illustrated in Figure 3.19

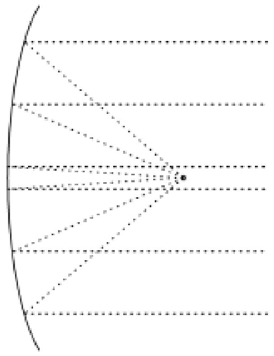

Figure 3.19: A reflector converts spherical waves into plane waves

The most critical parameters that characterize an IRA reflector are the diameter D and the focus F of the reflector. If we express the reflector with these two parameters, the F/D ratio an important parameter determining the reflector's geometric feature. For an IRA, this ratio is usually in the range from 0.35 to 0.60.

3.3.3 Termination Loads

There are resistors in a junction between a feed arm and a reflector for matching purposes. These resistors are used to minimize reflections from the reflector and to drain accumulated charges in this region. The effect of resistors on return loss is generally seen at low frequencies, and they do not affect high-frequency components [47].

3.4 Balun

The outer conductor and dielectric material of a coaxial structure can be cut out by sector angles according to the Klopfenstein tapered structure. This way, a parallel two-wire structure is reached. The sector angle of the coaxial structure is initially zero and it continues along the removed part until the width of the outer conductor is equal to the width of the inner conductor.

The slotted coaxial line transition described above behaves like a balun and an impedance transformer between the coaxial and parallel two-wire structures [53]. The tapered part can follow different geometric lines. These can be referred to as linear or Klopfenstein tapers. According to Klopfenstein's study, the most optimal coefficients are given in [58]. Although the linear taper is not optimal, it can be preferred for ease of production. Tapered coaxial-to-parallel two-wire transitions are used when impedance transformation, unbalanced-to-balanced transition, and 10:1 bandwidth are required.

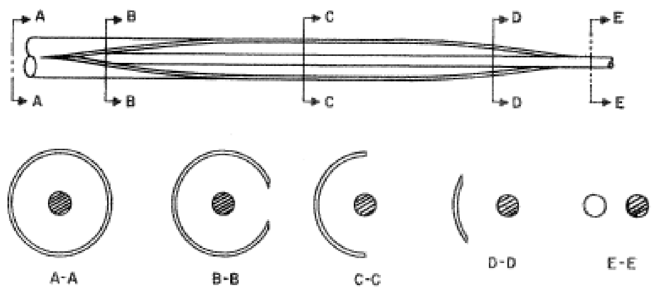

Figure 3.20: Tapered coaxial-to-parallel wire transition [53]

The coaxial port of a balun supports TEM mode below the high end of the frequency band. Parallel-wire port supports balanced (differential-mode) currents. The characteristic impedance of a two-wire transmission line is always greater than that of a closed coaxial line. Since the transition is not shielded, it also supports unbalanced (common-mode) currents related to spurious radiation from the tapered slot. Careful experimental studies show that unbalanced current and spurious radiation are very low in Klopfenstein tapers [58].

The highest operating frequency is dependent on the high-order coaxial modes [48]. An ideal tapered transition is a high-pass device, and the minimum operating frequency constraints the size of the transition. The highest operating frequency is determined by the inner and outer diameters of the coaxial structure. Radiation from the transition increases with frequency. The length of a -20 dB Klopfenstein transition is approximately equal to half of the wavelength. S_{11} parameters for 100-ohm output from 50-ohm input in four different transitions cases (with the same length) are given in Figure 3.21. The Klopfenstein taper appears to be better than the linear taper and performs better particularly at low frequencies.

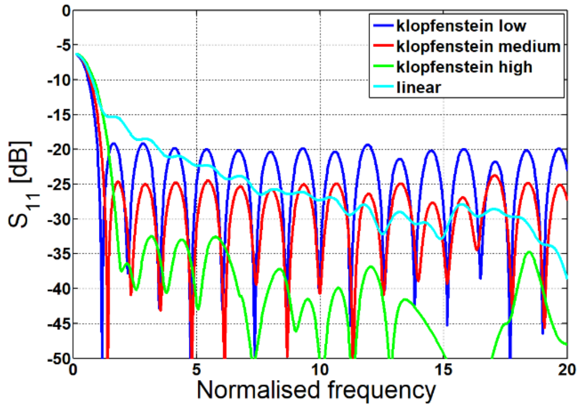

Figure 3.21: S_{11} parameter for different types of Klopfenstein tapered balun [87]

Since the transition is an open structure, some of the energy can radiate. As the transmission coefficient is less than 0.3 dB in the operating frequency range, this kind of spurious radiation is low as in Figure 3.22 [87].

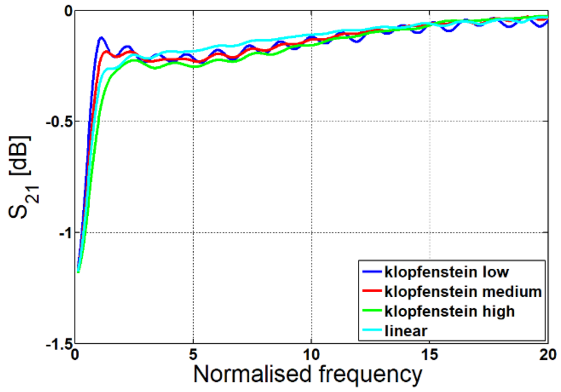

Figure 3.22: S_{21} parameter for different types of Klopfenstein tapered balun [87]

3.5 High-Voltage Pulse Measurement

Many pulsed power systems operate from 50 kV to 10 MV and they generate electrical pulses with pulse durations of nanoseconds or microseconds. In high-voltage pulse systems, measurement equipment must be high-voltage resistant, while their operation bands must be UWB. Measurement results can easily be corrupted due to the distortions in the measured signal forms. In general, pulse voltages and currents can be measured with D-dot or V-dot probes, capacitive probes, electro-optical transducers or Rogowski coils, I-dot probes, and current viewing resistors.

3.5.1 D-dot or V-dot Probe

In high-voltage pulsed systems, measuring the signal produced by the coaxial PFL is of great importance. In this study, a D-dot or V-dot probe design is designed and built, since commercially available products are costly, and they are not fully compatible with all frequency and voltage levels. The designed probe, which can be found in many successfully implemented studies with the capacitive voltage divider principle. By connecting two capacitors in series with $C_1 << C_2$, a large part of the voltage can be measured on C_1, and a small portion can be measured on C_2. An equivalent circuit diagram is given in Figure 3.23.

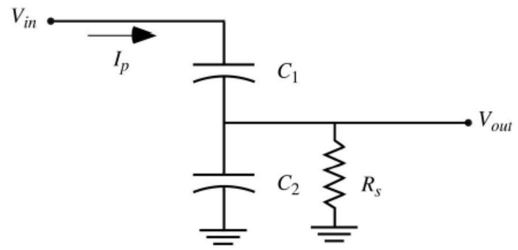

Figure 3.23: Equivalent circuit of a V-dot probe (capacitive voltage divider) [67]

Considering Figure 3.23, mathematical relationship between the input and output voltages can be calculated by Laplace transform as [67]

$$\frac{V_{in}}{V_{out}} = \frac{(C_1 + C_2)}{C_1} + \frac{1}{sR_sC_1}. \tag{25}$$

The bandwidth of the capacitive voltage divider can be calculated with,

$$\omega_{3dB} = \frac{1}{R_s(C_1 + C_2)}. \tag{26}$$

The capacitive voltage divider shows different characteristics according to the operating frequency band. Specifically, it switches to differential mode at high frequencies, while it is in linear operating mode at low frequencies. Consequently, for signals with low and fast rise times, two different equations are used to characterize the output voltage as

$$V_{out} = \frac{C_1}{(C_1 + C_2)} V_{in} \tag{27}$$

$$V_{out} = R_s C_1 \frac{dV_{in}}{dt}, \tag{28}$$

respectively. One of the most common ways to measure the high-voltage between the two electrodes is by adding a new low-voltage leg using the natural capacitance between the electrodes. To measure the high-voltage pulse voltage on a coaxial cable or on a PFL, the probes can be placed on it without disturbing the coaxial structure. Then, the frequency response or the S_{21} parameter can be measured via VNA. In this process, an inverse calculation is required to characterize the signal in the main coaxial structure from the probe signal. The probe placed in the coaxial structure behaves like a capacitive divider can be seen from Figure 3.24. N-type or SMA connectors can be used as probes.

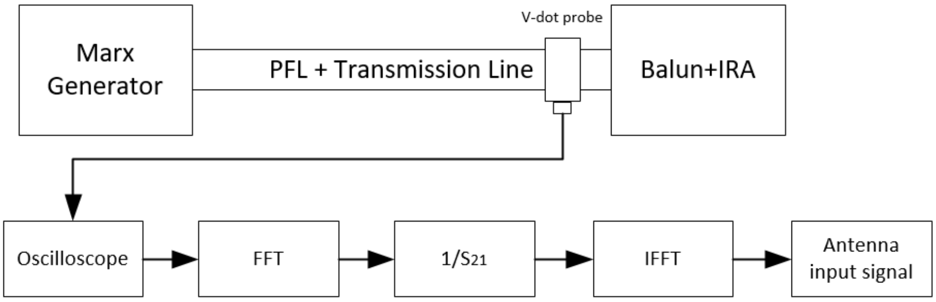

Figure 3.24: Processing the data extracted by a V-dot probe [69]

3.6 Conclusion

In this chapter, working principles of the system components, i.e., Marx generator, PFL, balun, IRA, and V-dot probe are explained, along with the specification of the design parameters. Equivalent circuit diagrams of the Marx generator in charging and discharging phases are given. This generator works like a multiplier circuit with very fast closing switches. It generates different output voltage signals for different load values. For this reason, a PFL, which has capacitive load characteristics, is charged very quickly by the Marx generator so that most of the energy remains in the generator. In the research on PFL operation theory, the pulse duration of the coaxial PFL is determined by the length of the PFL. The breakdown risk and dispersion parameters determine the inner and outer conductor diameters of the coaxial PFL structure. The energy stored in the PFL is transferred to the IRA by a spark gap that operates as a very fast closing switch. Different types of insulation materials (gas, vacuum, oil, etc.) can be used in the spark gap. Klopfenstein tapered balun, which possesses a two-wire structure, is considered for the transition from the coaxial structure to the IRA. This balun can operate in broad frequency ranges, while spurious radiation from the slotted part is at acceptable levels.

IRA operates like a differentiator; it takes the derivative of the pulse at the input and converts it into an electric field signal. This type of antennas is also called dispersionless. An ideal IRA signal has a prepulse and tail structure. Optimization studies show that the dimensions and angles of the feed arms determine the input impedance. Finally, V-dot probe works like a capacitive voltage divider. During pulse measurements, it shows linear characteristics for signals with slow rise times and differentiative properties for signals with fast rise times.

CHAPTER 4

DESIGN, SIMULATION, AND EXPERIMENTS

4.1 Simulation Environment: CST Studio Suite

In this thesis, simulations and optimization of designs are carried out by using CST Microwave Studio. In CST, 3D EM designs, systems, and components can be analyzed and optimized. Specifically, CST Studio Suite can be used for different applications, such as analyzing the performance and efficiency of antennas and filters, electromagnetic compatibility, and interference (EMC/EMI), and investigating thermal effects in high-power devices [88]. CST Suite includes different types of solvers for analysing EM problems, like time-domain, frequency-domain, and eigenmode solvers etc. In this thesis, mostly the time-domain solver is used, considering the nature of the problems under investigation.

4.1.1 Time-Domain Solver

The CST Time-domain Solver can perform broadband simulations in a single run. The time-domain solver calculates fields at discrete times, locations and computes the energy transfer from one port to another port. Two time-domain solvers can be used in CST MWS [88]. One of them is the transient solver, and it is based on the finite integration technique. The other is the TLM solver, which is based on the transmission line method (TLM). These solvers use slightly different grid types as hexahedral TLM.

4.2 Marx Generator

4.2.1 Design and Experiments

The circuit diagram of the Marx generator designed by TÜBİTAK BİLGEM is given in Figure 4.1.

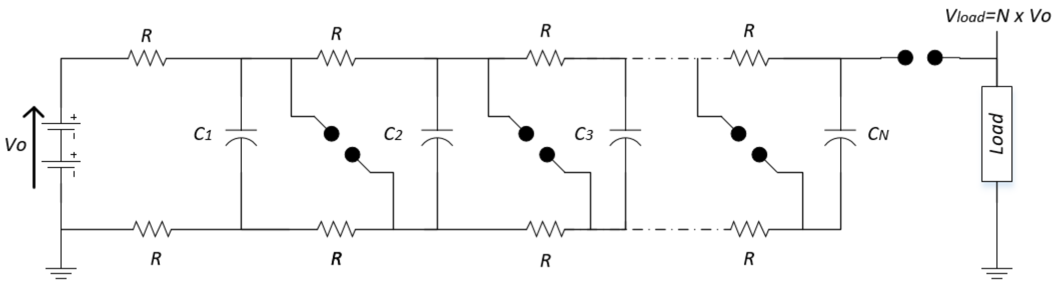

Figure 4.1: General circuit schematics of a Marx generator with load

Six 0.22-μF, 2.5 kV capacitors and two 1-kΩ charging resistors are used on each stage, and the equivalent capacitor, inductor, and resistor values as given in Table 4.1. Each capacitor of the Marx generator, which has a total of 5 stages, is charged to 10 kV to obtain 50 kV peak voltage on the load. The Marx generator used in the experiments can be seen in Figure 4.2. Spark gap electrodes are made of brass and they have spherical shapes. A commercial 39 kV Caltest voltage probe is used to measure the output signal of the Marx generator, as shown in Figure 4.3.

Table 4.1. Marx generator components

C_M	7.33 nF
L_M	2.25 μH
R_{ch}	1 kΩ

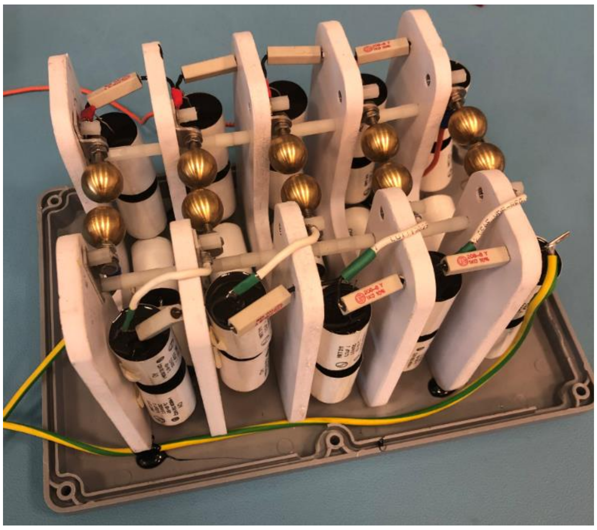

Figure 4.2: Mini Marx generator with 5 stages

Figure 4.3: Caltest CT4028 39 kV voltage probe

The output signal of the Marx generator varies according to the load. In other words, the use of resistive or capacitive loads directly affects the output signal of the Marx generator. For this reason, in this section, the output signal is measured with different resistive loads connected (as outputs) to the output of the Marx generator. HVR non-inductive 10, 22, 47, and 100-ohm carbon resistors are used as loads in the first experiments, leading to the results in Figure 4.4. We observe that, as the resistance value increases, the amplitude of the output signal increases. In addition, over-damped, under-damped, and critical-damped situations can be observed in these experiment results.

Due to the inertial inductance of the Marx generator and the noise generated by spark gaps, oscillations can be observed in the output signal. Specifically, the Marx generator causes a lot of noise without a shield because of the spark gaps. Therefore, it is placed into a cylindrical aluminium case in the final design, in order to reduce noise, as well as the inductance.

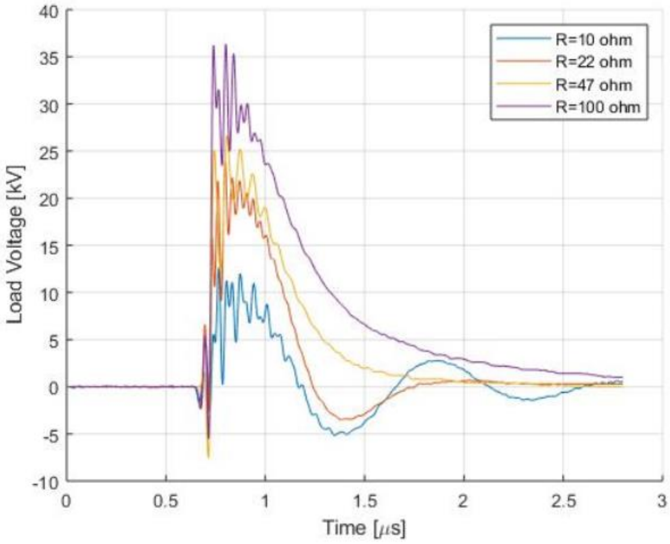

Figure 4.4: Output signal of the Marx generator with different resistive loads

4.2.2 Simulations

As described previously, a spark gap is simulated as a parallel capacitor connected in series to an inductor and a switch structure in Pspice, as seen in Figure 4.5. The Pspice simulation model of the Marx generator can be seen in Figure 4.6. The inductance values of the model are optimized using the experiment results. Thus, the simulation and experiment results are matched, as shown in Figure 4.8 and Figure 4.9. The equivalent circuit model is given in Figure 4.7, and the total internal inductance of the Marx generator is set to 2.25-μH. This value is relatively high for a Marx generator. When the Marx generator is shielded, however, the outer conductor acts as a return conductor to decrease the inductance of the generator. As the inductance decreases, the Marx generator's discharge time is reduced.

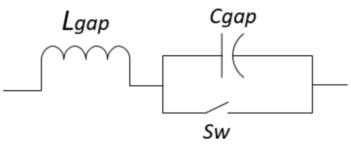

Figure 4.5: Equivalent spark gap circuit schematic

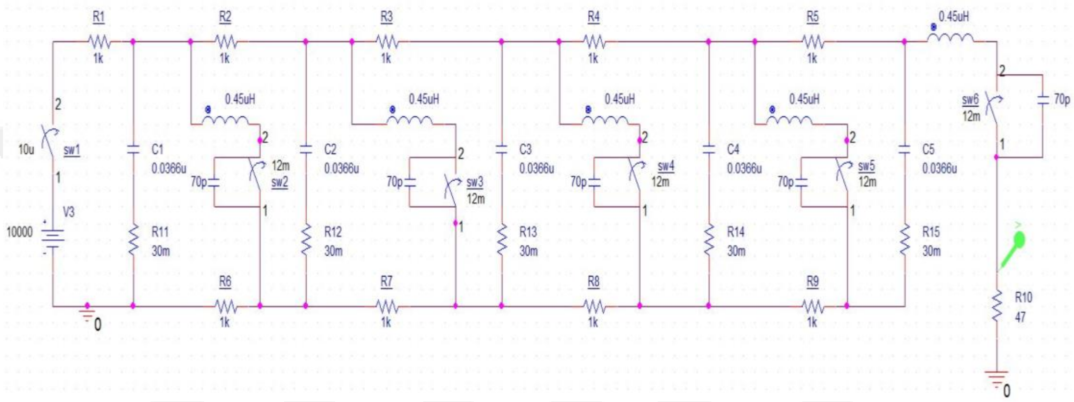

Figure 4.6: Marx generator Pspice circuit model

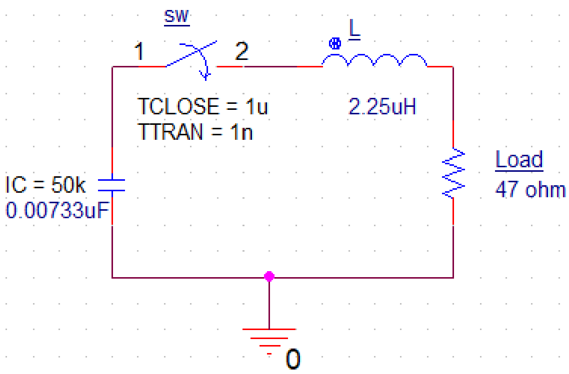

Figure 4.7: Equivalent circuit model of the generator during discharge

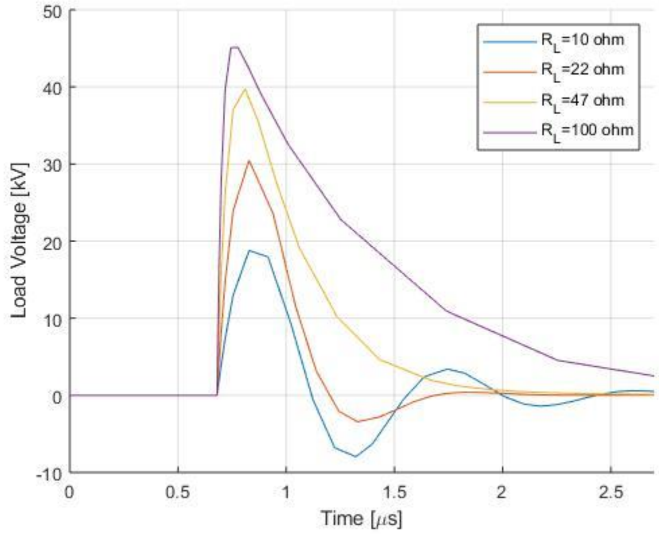

Figure 4.8: Pspice simulation results with different resistive loads

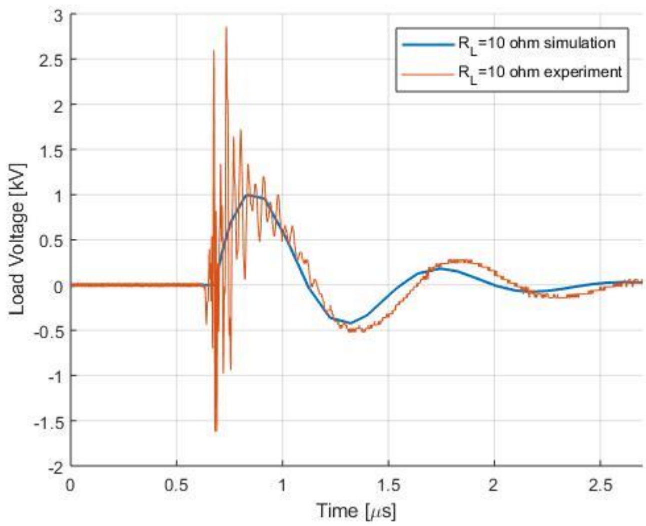

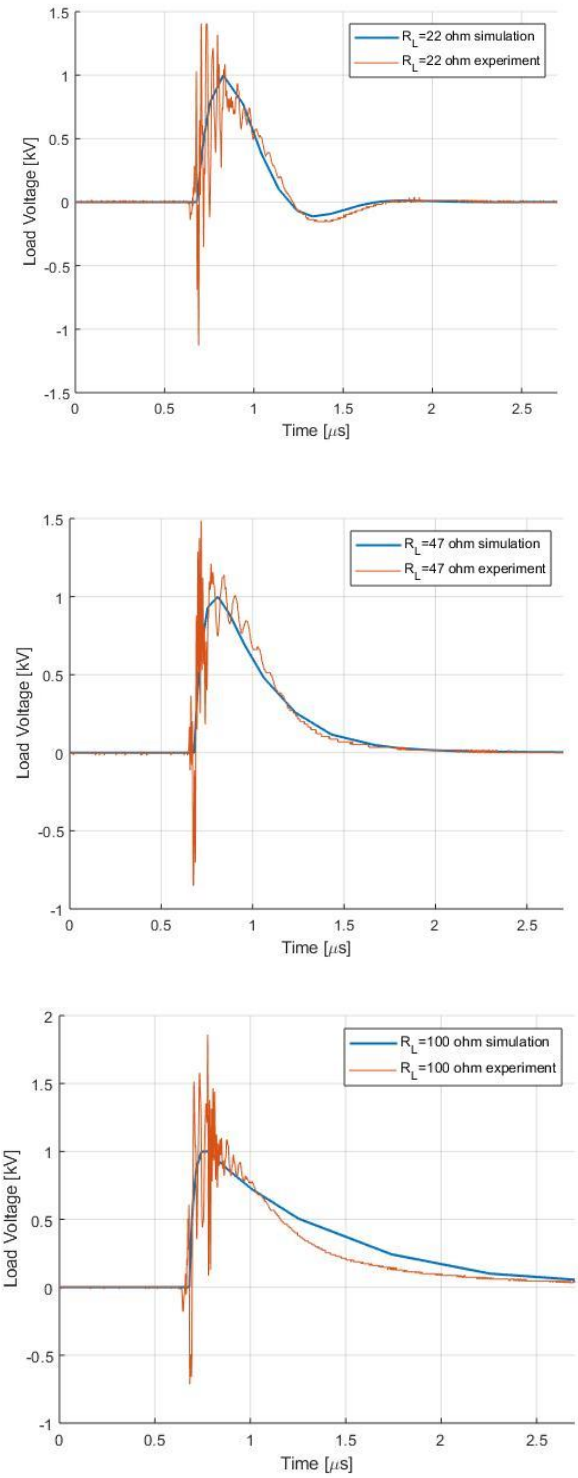

Figure 4.9: Comparison of the simulation and experiment results (normalized)

4.3 Pulse Forming Line

A coaxial PFL consists of two main components: A peaking capacitor and a very-fast closing switch. This unit's design parameters are determined by the desired rise times of the pulse, pulse width, characteristic impedance of the coaxial line, and the capacitance of the peaking capacitor. In this context, since the pulse width is desired to be around 2 ns, the length of the PFL is calculated as approximately 10 cm with equation (17), while the capacitance of the peaking capacitor is calculated as 10 pF using equation (15). The other design criterion is 50-ohm characteristic impedance of the coaxial structure, which provides the ratio of the inner and outer diameters via equation (14). However, two other criteria that limit the diameters of the inner and outer conductors are dispersion and electrical breakdown risk. Specifically, the inner and outer conductors cannot be very close to each other to avoid electrical breakdown. The breakdown strengths of transformer oil and PTFE are roughly 50 kV/mm. Hence, the applied voltage between the inner and outer conductors should be smaller than this value multiplied by the distance between them. This is how the minimum value of the distance is limited.

On the other hand, the upper value of the distance is limited by the dispersion criteria with the cut-off frequency of 1.7 GHz. This cut-off frequency is determined by the rise times of the expected pulse. High-frequency components or picosecond rise times are not expected from this PFL output since unpressurized transformer oil is used. Thus, maximum diameters are calculated by considering equation (19) and equation (20). The final PFL design parameters can be seen in Table 4.2.

Table 4.2. PFL dimensions

Length	10 cm
D_o	3 cm
D_i	8.7 mm
ε_r	2.1
Z_o	50 ohm
C_p	10 pF

Equivalent capacitance and inductance values of the Marx generator are given in the previous section, and the graph related to the Marx discharging on the peaking capacitor is shown in Figure 4.10. As we observe in the graph, the peaking capacitor is rapidly charged to twice the Marx generator's total charge. In other words, a 30 kV Marx generator charges a 10-pF peaking capacitor to 60 kV in ns levels.

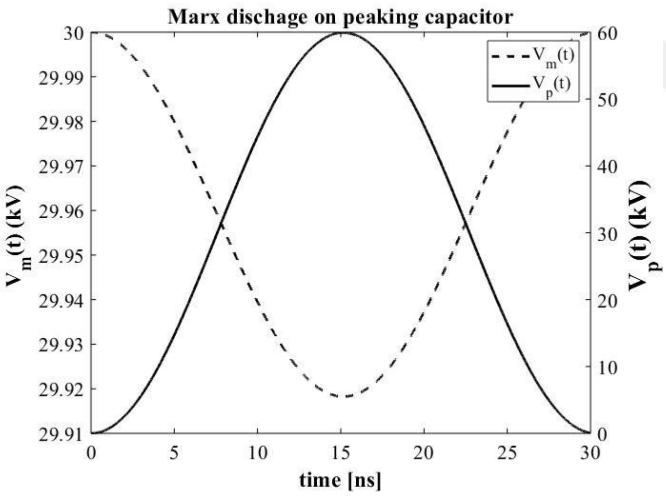

Figure 4.10: Simulation results of Marx discharge on the peaking capacitor

4.3.1 Simulation

PFL simulations are rarely seen in the open literature since available simulation programs cannot model spark gaps. One of the simulation models presented in recent years is modelling a spark gap as a discrete voltage source [35], while another is modelling it as a discrete current source presented for the first time in [27] [88].

In this thesis, the spark gap is modelled as a discrete current source with CST studio suite, as in [27]. This simulation aims to see the effect of the length of the PFL on the pulse width on the load. The simulation configuration of the spark gap and the PFL model are given in Figure 4.11.

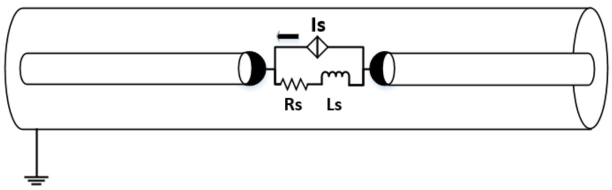

Figure 4.11: A simulation model of the PFL and the spark gap

In the model, 50-ohm load impedance is placed at the end of the 50-ohm coaxial transmission line for termination. The current source generates the predetermined current signal through L_s and R_s (inductance and resistance of the spark gap). Meanwhile, a voltage drop occurs in the spark gap switch, which shows that the impulse generator is charging the peaking capacitor. After a while, a steady-state is reached, and we have $V_{pfl} = V_0 = I_{sg}R_{sg}$ [27]. Then, the charge in the PFL is transferred to the load when the spark gap is closed, which means that the discrete current source is turned off. The rise times of the signal transferred to the load can be controlled with the fall time of the current signal [27]. The signal of the current source is shown in Figure 4.12.

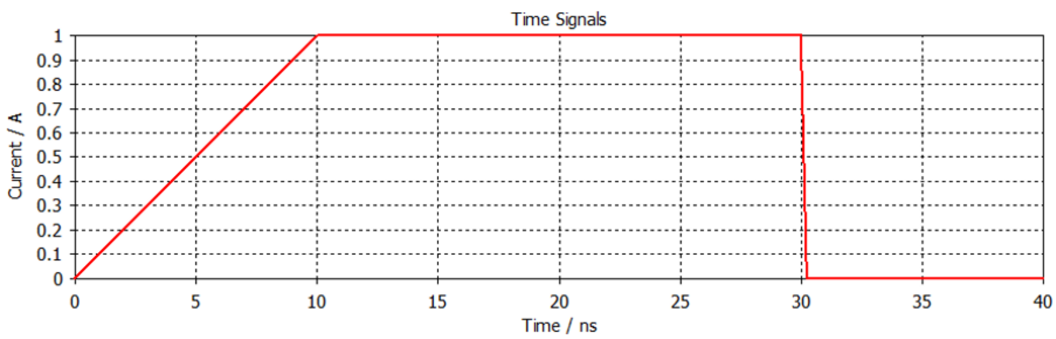

Figure 4.12: Input current signal of the discrete current source

In this study, a PFL simulation with 50-ohm characteristic impedance and 15 cm length is performed with CST MWS. After the spark gap, a transmission line is added to show the transfer of the signal to the load. PTFE with a dielectric constant of 2.1 was used as an insulation material. As the length of the PFL determines the pulse duration via equation (17), this effect can also be seen in the simulation results. After the current source is turned off, the delay in transferring the signal to the load is determined by the transmission line length on the right-hand side. In Figure 4.13, a zoomed view of the spark gap used in the simulation model is shown. A current source, lumped element, and voltage monitor are added. Figure 4.14 shows the entire PFL model. The transmission line is terminated with 50 ohm. The left-hand side is seen as an open circuit, as the spark gaps close after the Marx generator charges the PFL [27]. Figure 4.15 shows the voltage signals on the load and the PFL. As can be seen, once the PFL is charged to 5 V and the current source is turned off, $V_0/2$ impulse appears on the load after a short time. The pulse duration is around 1.5 ns, as also seen in Figure 4.15.

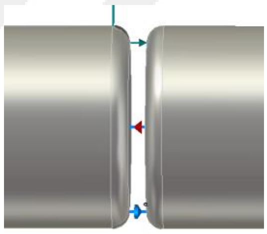

Figure 4.13: Spark gap with current source

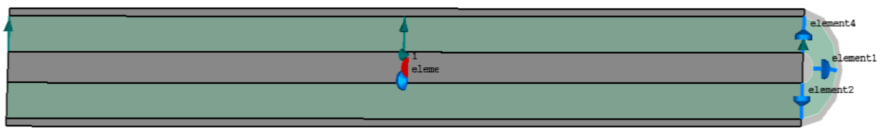

Figure 4.14: PFL simulation model

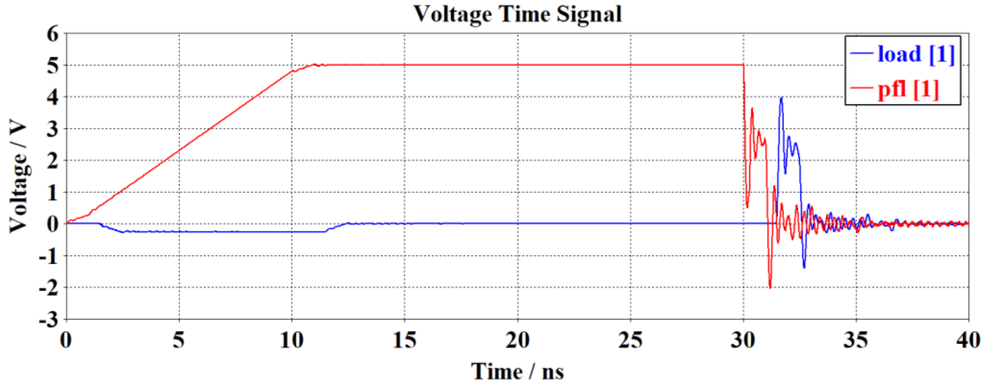

Figure 4.15: Simulation results for the PFL

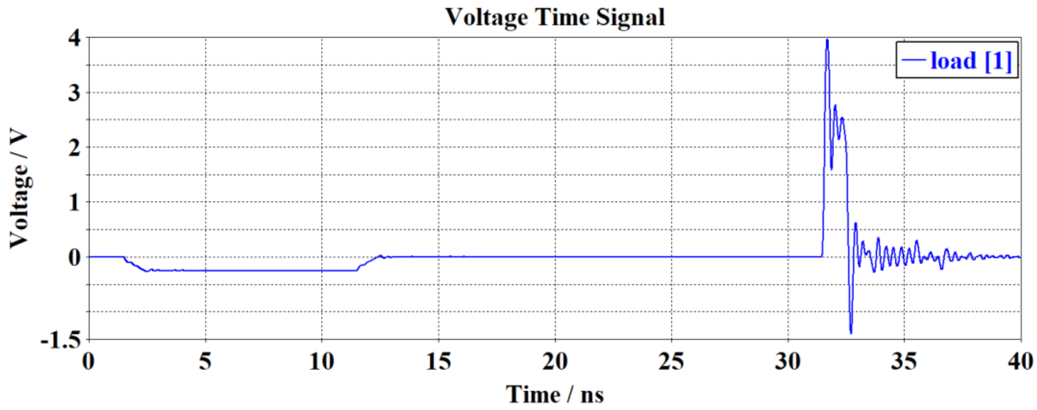

Figure 4.16: The signal transferred to the load

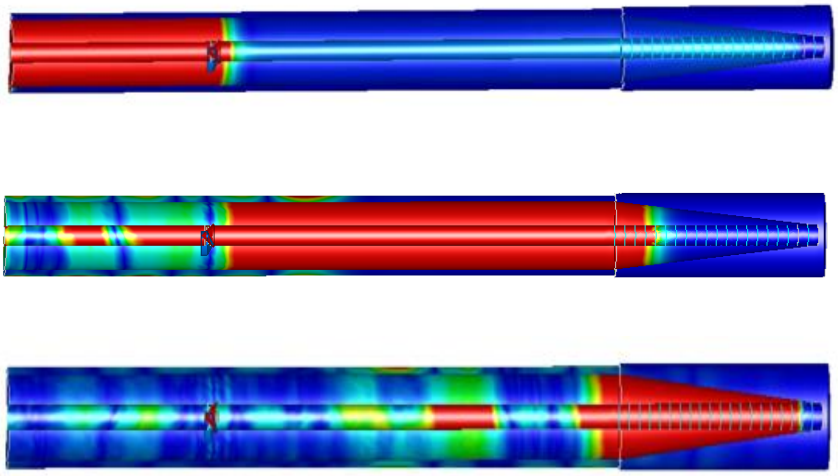

Figure 4.17: PFL simulation with a 50-ohm termination

4.4 Impulse Radiating Antenna

4.4.1 Reflector

A parabolic reflector, which is already available in TÜBİTAK BİLGEM, is used in this study. The reflector dimensions are listed in Table 4.3, and photographs of the reflector can be seen in Figure 4.18. F/D ratio is equal to 0.33, which is lower than the F/D ratios of typical IRAs.

Table 4.3. Reflector dimensions

Diameter	87 cm
Focus	28.7 cm
F/D ratio	0.33

Figure 4.18: Parabolic reflector

4.4.2 Feed Arms

Feed arm designs are made based on the optimization study given in [38], and then the reflection coefficient is reduced below -10 dB in the operating frequency range using a coaxially tapered balun. The geometric structures, dimensions, and angles of the feed arms are illustrated in Figure 4.19. Each feed arm has 40 cm length and 20 cm width. There is a 45-degree angle from the vertical line, while they make 74.29-degree angles towards the reflector. In simulations, feed arm dimensions are determined as a result of an optimization process. The dimensions that give the best reflection coefficient for 100 ohm input impedance are chosen for the final design. The reflection coefficient could further be improved using exponential geometric features, but a conventional IRA is considered in this thesis. The feed height is equal to 10 mm at the feed point. According to the optimization studies, the return loss parameter gets better as the feed height decreases. But when the feed arms get closer, there is a risk of electrical breakdown at the feed point.

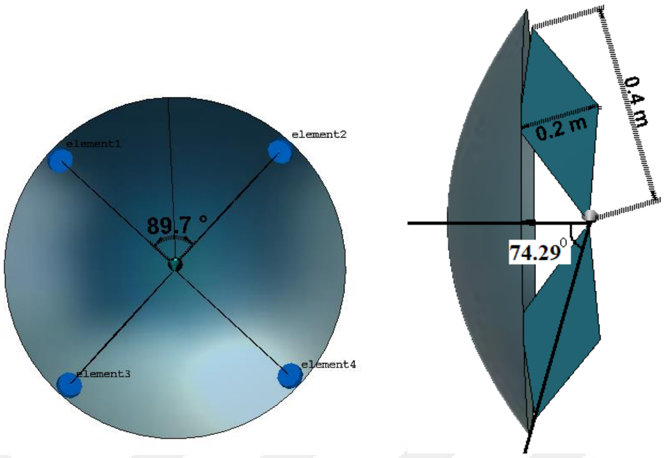

Figure 4.19: Dimensions and angles of the feed arms

4.4.3 Termination

In the design, 200-ohm resistors are placed at the junctions between the reflector and the feed arms to eliminate the DC components of the output signal. For this purpose, parallel 200-ohm carbon resistors are used in the experiments, considering that input impedance is 100-ohm for a feed arm.

4.4.4 Balun

As explained in the literature review, a splitter balun is usually preferred to feed a full IRA, while a HIRA can directly be fed directly from the focus with the help of a closing switch.

In this thesis, a full IRA is designed because HIRAs have asymmetric radiation patterns. For this purpose, an alternative balun is tested as feeding. The proposed balun transforms the coaxial structure with 50-ohm characteristic impedance to a 100-ohm parallel-plate structure, as seen in Figure 4.20. Then IRA feed arms are fed with this parallel-plate end of the balun. On the other hand, there are many restrictions on the design of the balun. In the antenna simulations, it is observed that an increase of the outer conductor diameter decreases the symmetry of the radiation pattern. The feed arm is shifted approximately 1 cm upwards along the vertical line in order to feed the balun through the focus, not at the center of the reflector. In this case, it causes asymmetry in the radiation pattern at low frequencies. The most critical factor limiting the length of the balun is the focus of the reflector. It is noted that the balun is not longer than the focus (28.7 cm). The length of the balun's slotted part is 255.2 mm, as shown in Figure 4.21 and it determines the lowest component of the operating frequency.

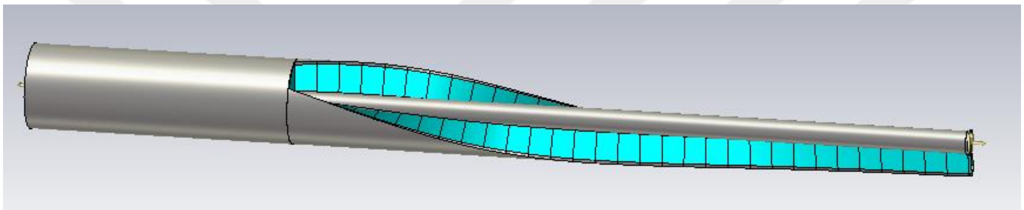

Figure 4.20: Balun with Klopfenstein taper

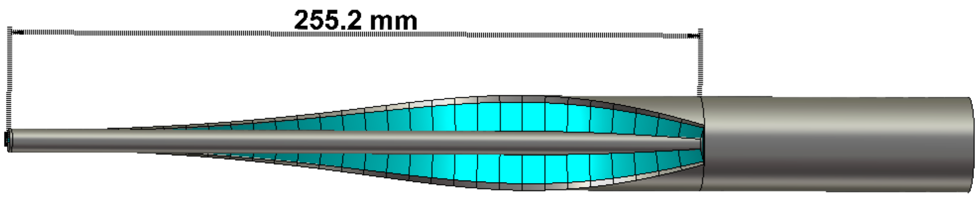

Figure 4.21: Balun length

The balun, which was manufactured in a 5-axis laser machine, can be seen in Figure 4.22. Aluminium is used for the inner and outer conductors, and PTFE is used as a dielectric material. Inner and outer conductor diameters are equal to the diameters of the PFL. Calculation of these dimensions are mentioned in the PFL section.

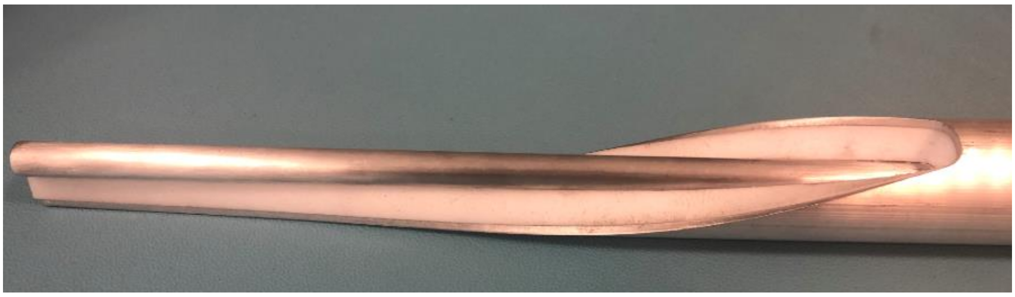

Figure 4.22: Manufactured Klopfenstein tapered balun

Table 4.4. Balun dimensions

Klopfenstein Tapered Balun (medium)	
f_{min}	350 MHz
Transition length	255.2 mm
D_i	8.7 mm
D_o	30 mm
ε_r	2.2

The simulation results for the Klopfenstein tapered balun can be seen in Figure 4.23, Figure 4.24, and Figure 4.25. It can be observed that the S_{11} parameter is below -25 dB between 500 MHz and 3.5 GHz. In addition, the S_{21} parameter has a constant behaviour, which indicates that this transfer function can transmit the whole signal without distortion.

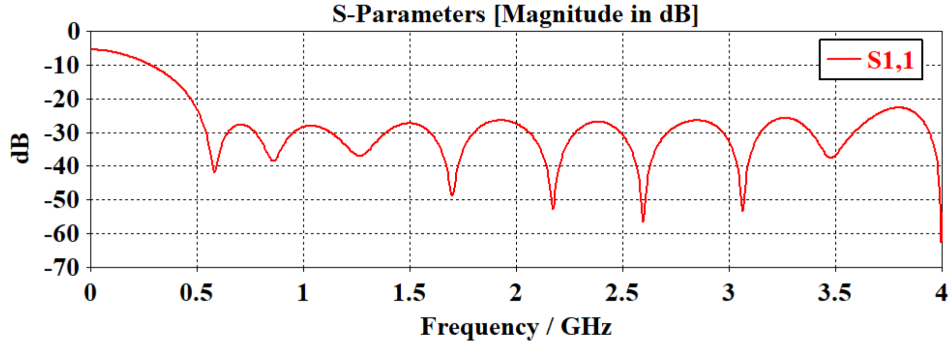

Figure 4.23: S_{11} parameter of the coaxial tapered balun

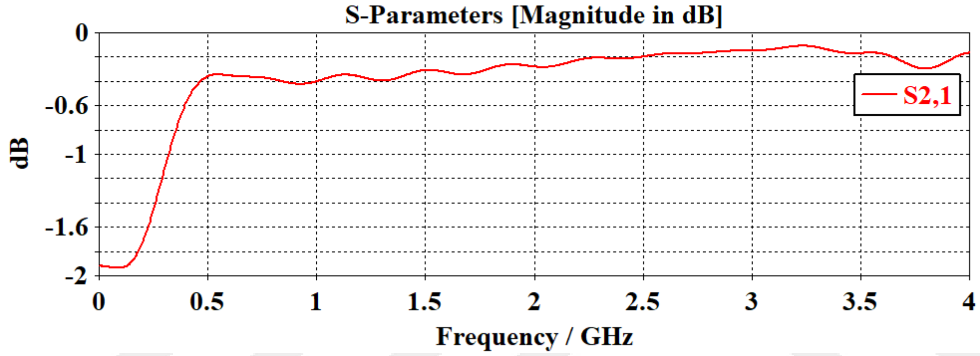

Figure 4.24: S_{21} parameter of the coaxial tapered balun

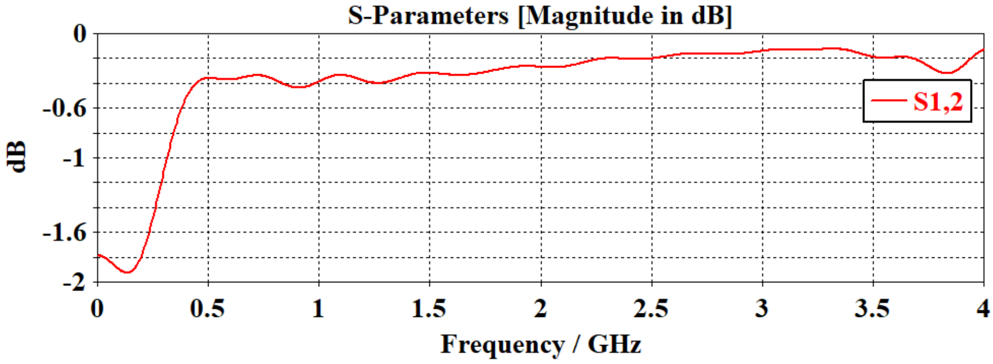

Figure 4.25: S_{12} parameter of the coaxial tapered balun

4.4.5 Simulation of Balun and IRA Structure

The designed balun and IRA structure can be seen in Figure 4.26. The coaxial balun transforms into a parallel wire structure and feeds the upper and lower feed arms at focus of the antenna. Time-domain simulations in this section are realized by feeding the balun with a waveguide source. As explained in the theory of operation section, the input impedance is mostly determined by the geometric shapes and angles of the feed arms. By changing the feed arm lengths, widths, angles, and conical structures parametrically, the S_{11} parameter is kept below -10 dB in the range from 300 MHz to 3.5 GHz range, as depicted in Figure 4.27. Four 200-ohm termination resistors, which are used as a matching circuit, can also be seen in Figure 4.26.

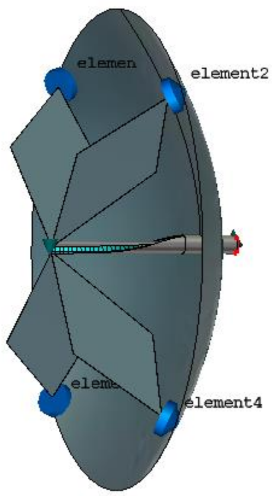

Figure 4.26: CST sketch of the IRA design with balun

Although the reflector with an F/D ratio of 0.35 gives better results in comparison to the 0.33 antenna, the S_{11} parameter is worsened slightly. Real and imaginary parts of the antenna impedance and time-domain reflectometer simulation results can be seen in Figure 4.28, Figure 4.29, and Figure 4.30, respectively. As seen in Figure 4.28 and Figure 4.29, the real part of the antenna impedance varies at around 50 ohm, while the imaginary part fluctuates at around 0 ohm. The impedance with respect to time can be observed in Figure 4.30.

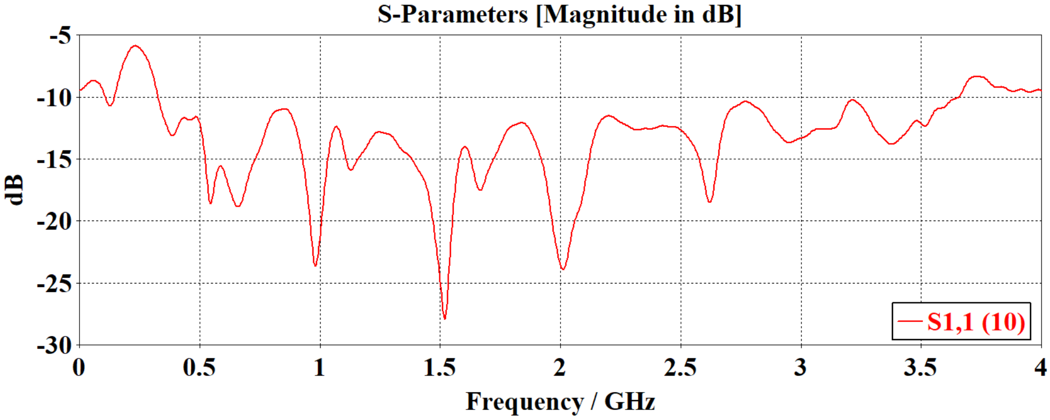

Figure 4.27: S_{11} parameter of the IRA with balun structure

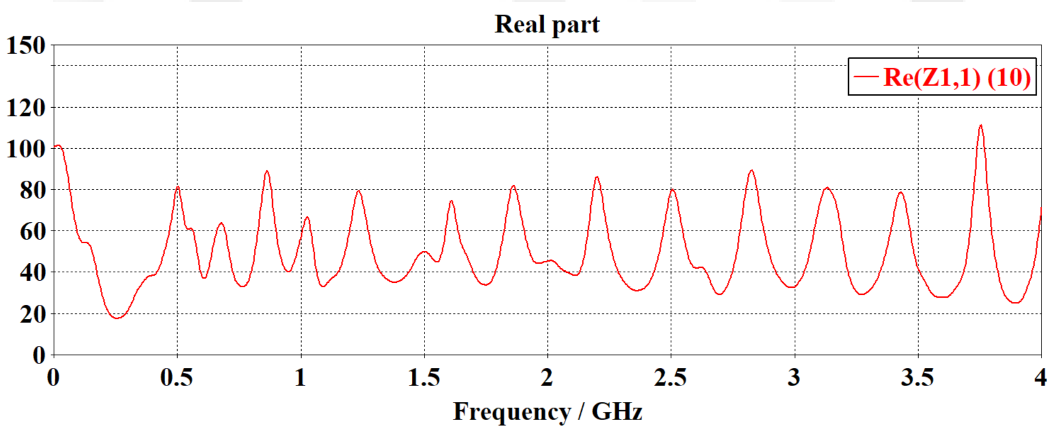

Figure 4.28: Real part of the impedance

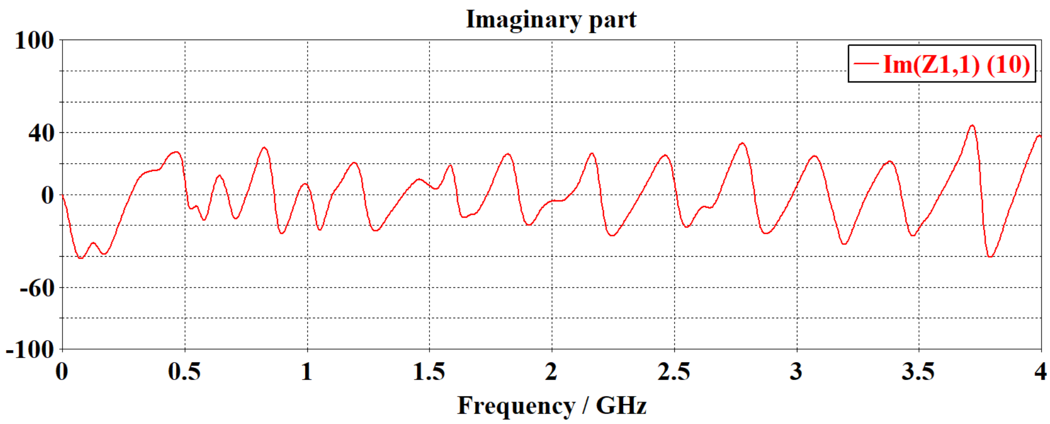

Figure 4.29: Imaginary part of the impedance

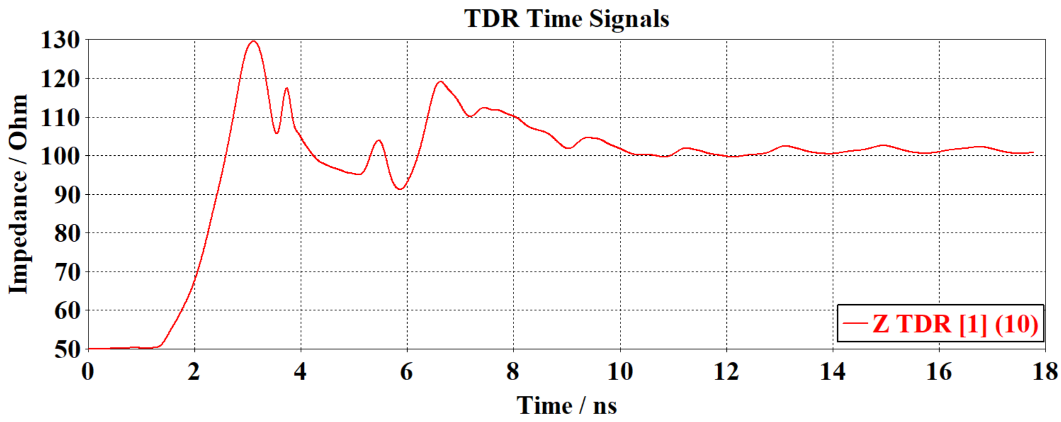

Figure 4.30: Time-domain reflectometer simulation result for the antenna with balun structure

The returned part of the power signal sent via the balun input is shown in Figure 4.31. We observe that a part of the pulse with an amplitude of less than 10% is reflected. We note that the reflected signals are critical in these systems since they may cause breakdowns. For this reason, such reflections are tried to be kept as low as possible.

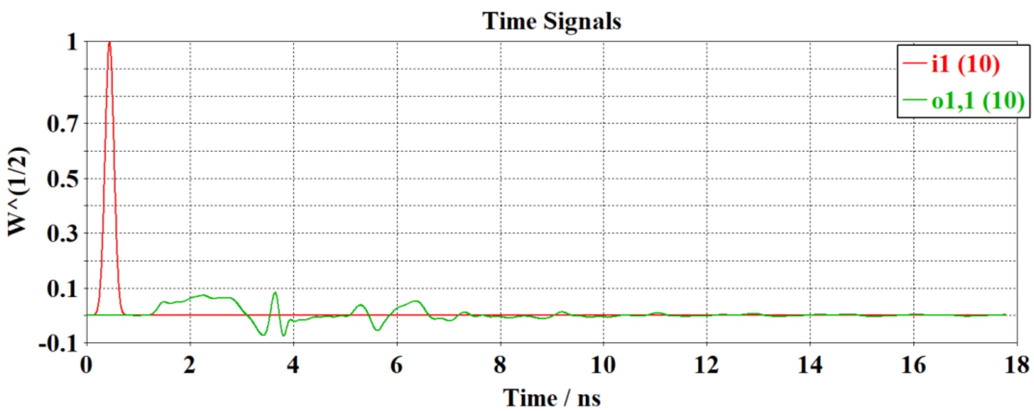

Figure 4.31: Input signal and reflected signal

Assuming that the voltage signal coming from the PFL is a Gaussian pulse (0-3 GHz) with an amplitude of 7 V as shown in Figure 4.32, the electric field strength at 15 m is calculated with an E-field probe in CST Microwave Studio. As seen in Figure 4.33, prepulse and main pulse forms are seen in measured E-field strength, and the overall function is the derivative of the signal applied to the antenna input. The peak-to-peak value of the y-polarized electric field intensity measured at 15 m is approximately 3V. The electric field strength with x-polarization is shown in Figure 4.34. Very low electric field values are obtained for this polarization.

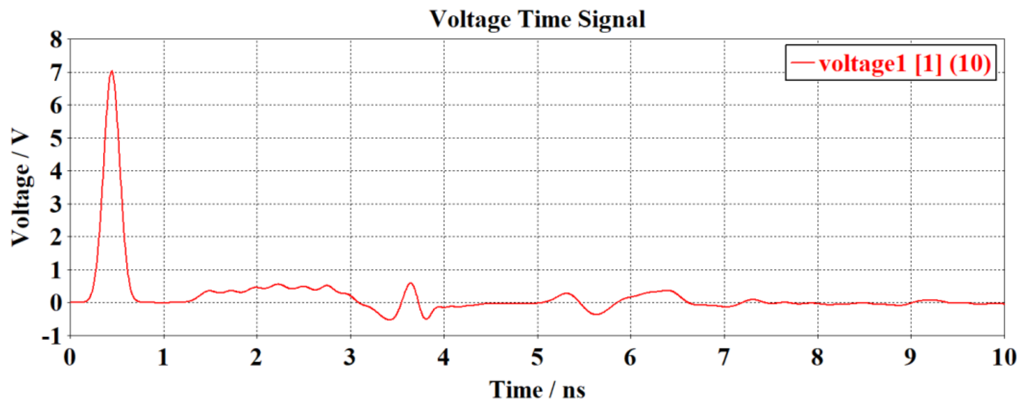

Figure 4.32: Input signal of the IRA with balun structure

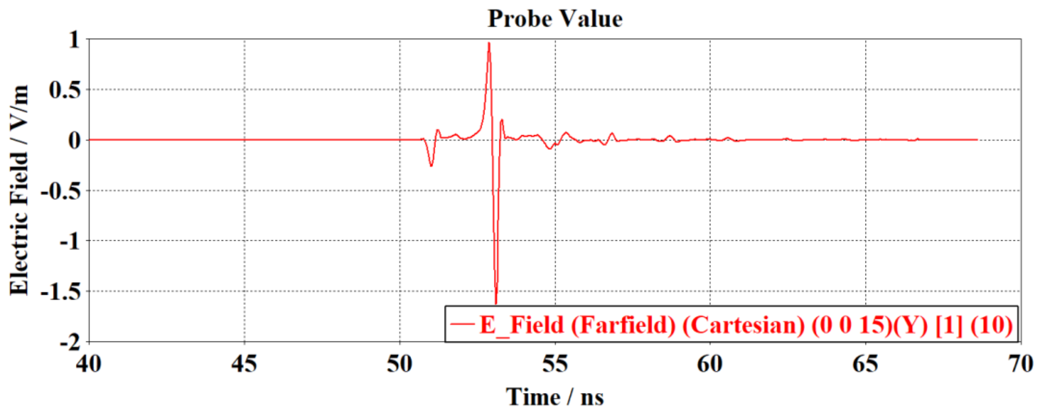

Figure 4.33: Simulation result for the y component of the electric field intensity at 15 m

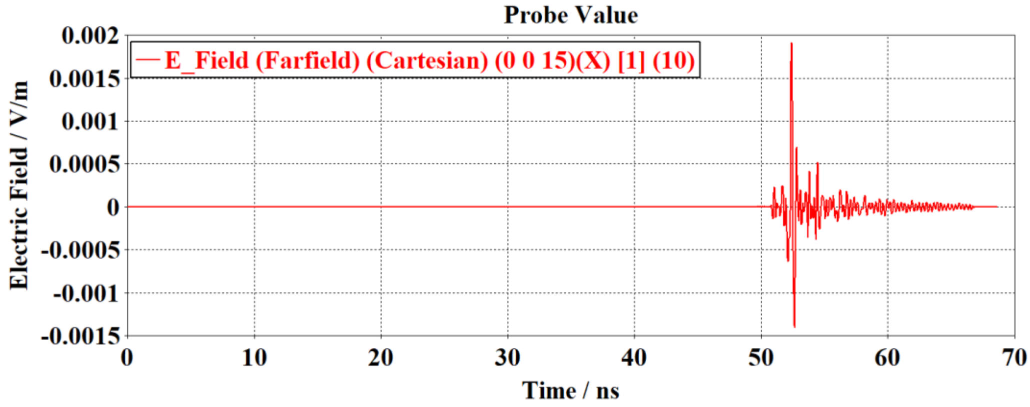

Figure 4.34: Simulation result for the x component of the electric field intensity at 15 m

4.4.6 Radiation Patterns

The radiation pattern images for the IRA simulated in the 300 MHz-4 GHz range can be seen in Figure 4.35 and Figure 4.36. We note that the radiation patterns are quite symmetric in the $\varphi = 0^o$ plane, and the directivity and gain of the antenna increase as the frequency increases. While the main beam is wide with a magnitude of 8 dB at 500 MHz, it becomes narrower with a value of 19 dB at 4 GHz. In the φ = 90o plane, it is seen that there are asymmetric patterns, specifically due to the shift of the balun by 1 cm upwards to the feed of the arms. Nevertheless, even these patterns are more symmetric than those of a HIRA. In addition, the symmetry of the patterns improves as the frequency increases.

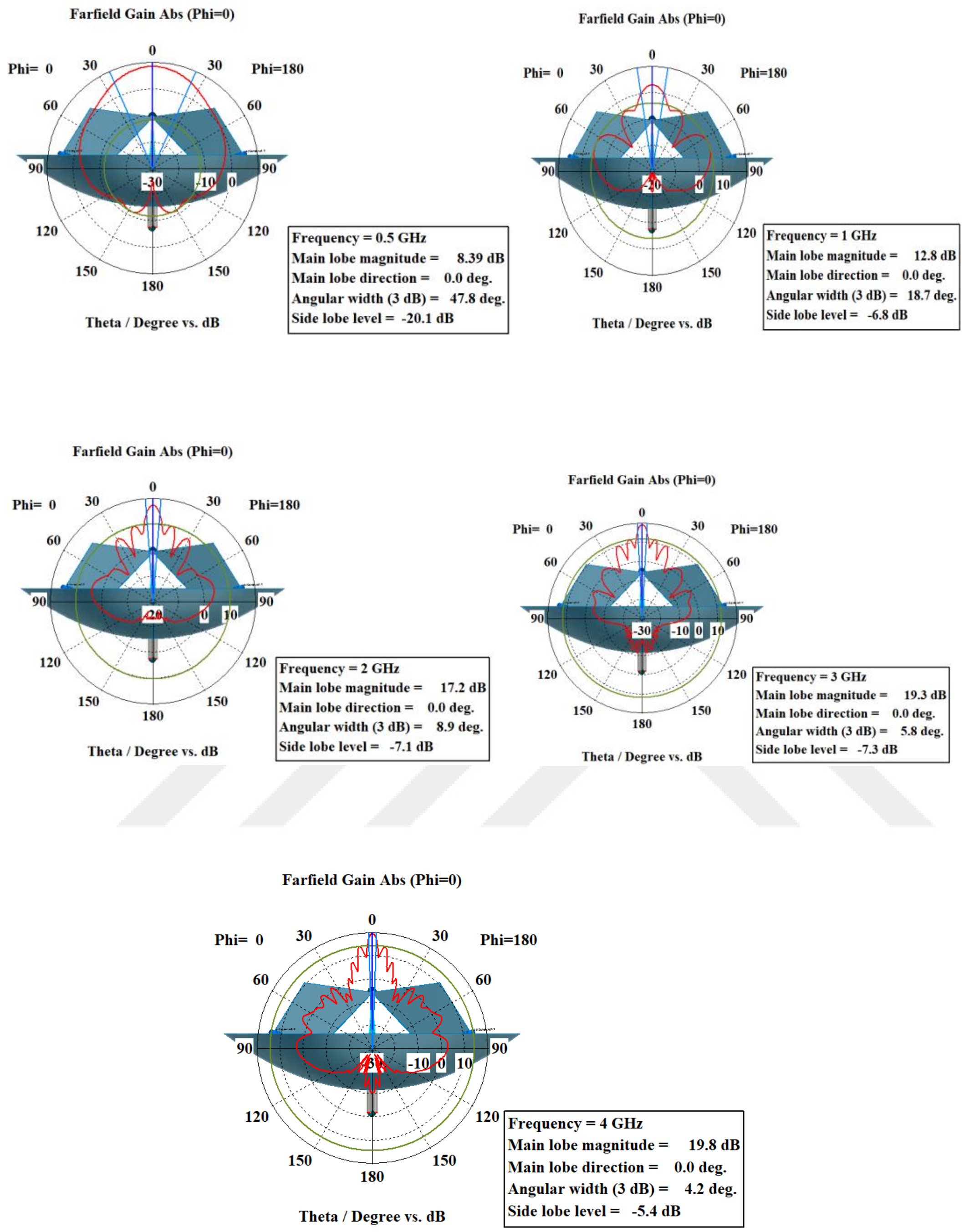

Figure 4.35: Gain patterns for the IRA in the $\varphi = 0^{o}$ plane

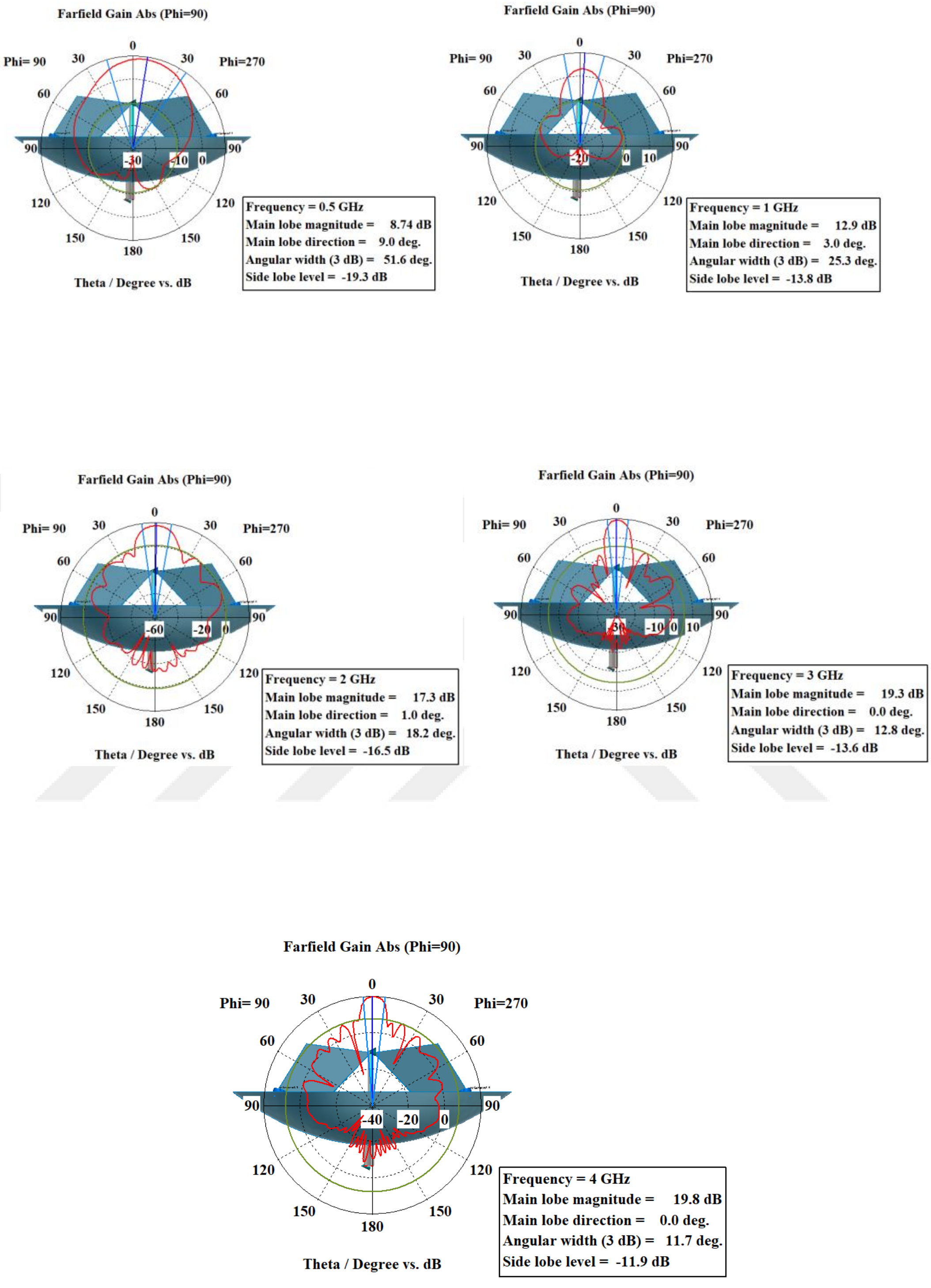

Figure 4.36: Gain patterns for the IRA in the $\varphi = 90^{o}$ plane

4.5 V-dot Sensor

In this section, design and measurement of a V-dot probe, which is also common in the literature, for a coaxial system containing high-voltage and high-frequency components are explained. Since commercially available high-voltage and high-frequency sensors are very expensive and have application limitations, a suitable sensor is designed in this thesis. The most significant advantages of the designed sensor are that it is inexpensive, easy to manufacture, and it does not require extensive 3D (EM) simulations. In the first stage, the sensor simulations are carried out by using the parameters of Times Microwave LMR-1700 [90], a low-loss coaxial cable. The impedance of the coaxial cable, whose outer conductor diameter is approximately 3.5 cm, is 50-ohm when PE is used as a dielectric. The probe is then manufactured with an SMA connector, a clamp, and a 30 cm LMR-1700 low-loss cable. S_{21} parameter is measured with a VNA, and compatibility of the results with the simulations is tested. The probe design, whose results are similar, is adapted to the actual system design. The probe to be mounted on the PFL could not be measured with VNA since a standard cable and connector suitable for PFL dimensions could not be found.

4.5.1 V-dot Sensor Simulation

CST simulation images of the V-dot sensor are given in Figure 4.37. An SMA connector mounted on a clamp is used as a probe, where the samples are taken. The clamp is in contact with the return conductor of the cable so that the outer conductor of the SMA connector is grounded. The voltage pulse signal sent along the coaxial cable is seen in Figure 4.38, while the voltage signal received from the SMA connector is given in Figure 4.39. When the signal form is examined, it is observed to be the derivative of the input signal, while being attenuated by 10^{-5} times in terms of the amplitude.

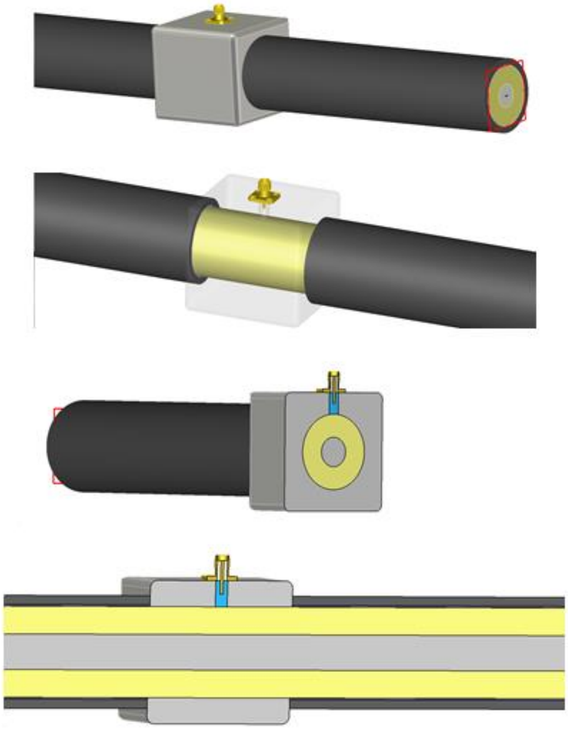

Figure 4.37: Side views of the V-dot probe mounted on the coaxial line

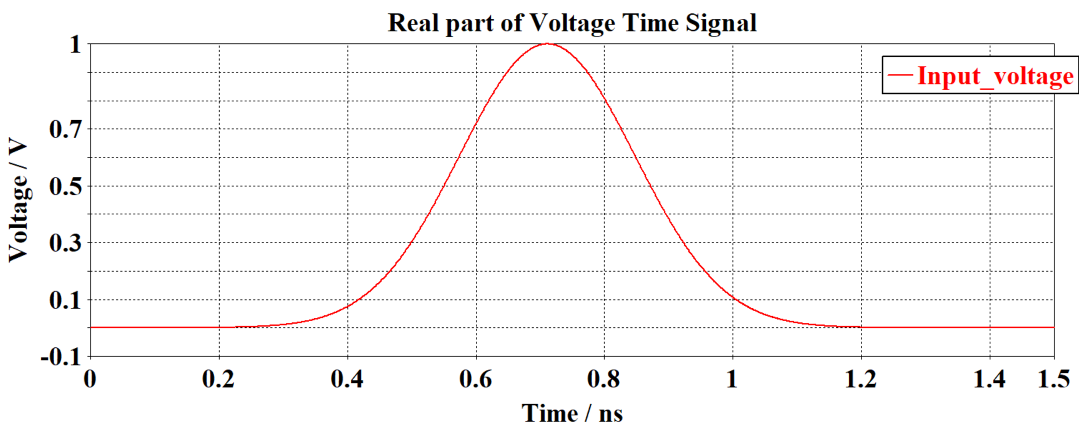

Figure 4.38: Input voltage signal of the coaxial line

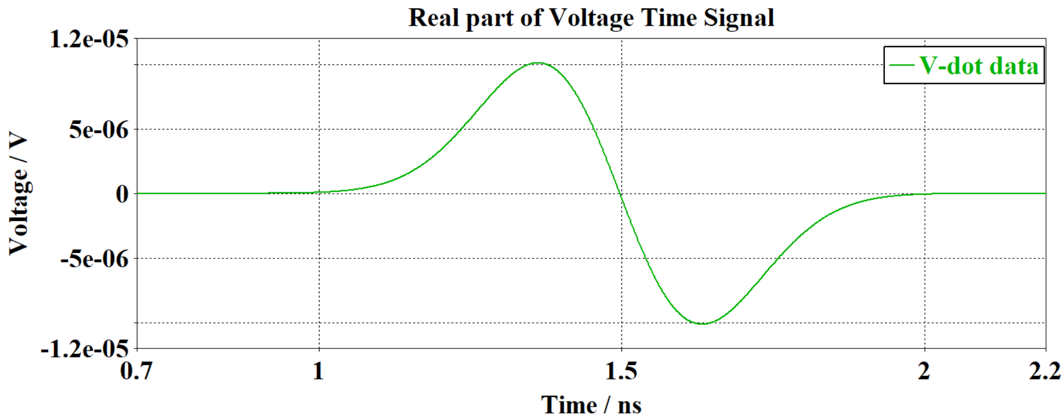

Figure 4.39: Voltage signal received by the V-dot probe

4.5.2 VNA Measurement

The manufactured V-dot probe is depicted in Figure 4.40. One end of the coaxial cable is terminated with 50-ohm impedance, and the S_{21} parameter between the input and the SMA connector is measured. VNA and S_{21} parameter measurement are further shown in Figure 4.41.

Figure 4.40: Manufactured V-dot probe with LMR 1700 coaxial cable

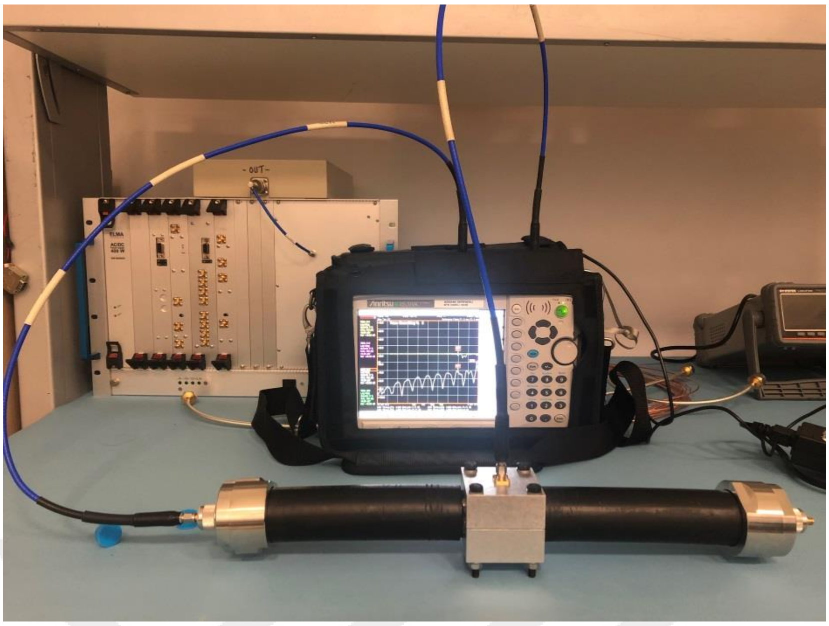

Figure 4.41: VNA measurement of the V-dot probe

The measurement results obtained from the VNA are exposed to 0% and 3% smoothing and compared with the CST simulation results, as seen in Figure 4.42. After obtaining the transfer function (S_{21} parameter) of the V-dot probe, signal processing steps should be performed as shown in Figure 3.24, then the pulse signal which is generated by the PFL can be calculated. Also, a standardized very-short pulse generator should be used for the calibration of the home-made V-dot probe. But in this thesis, calibration steps could not be completed since there is no available standardized commercial picoseconds level pulse generator in Tübitak Bilgem.

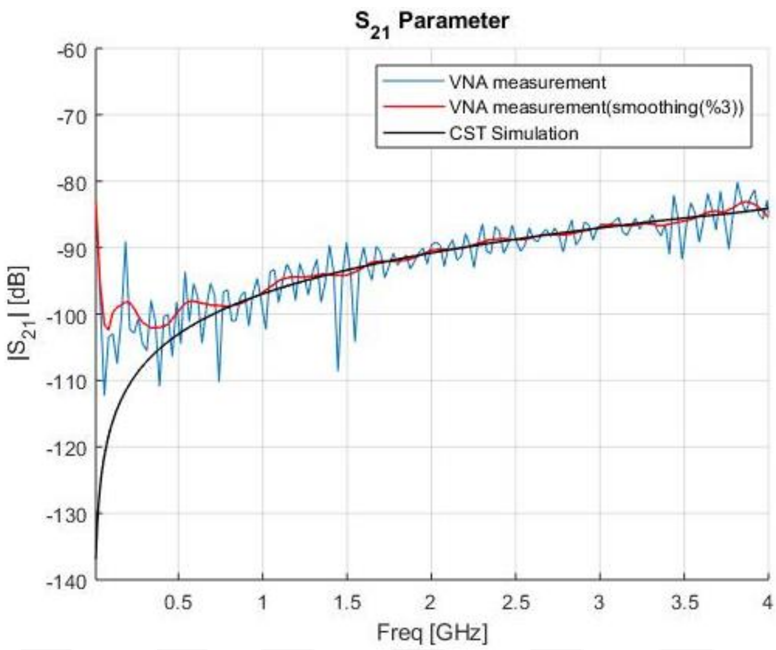

Figure 4.42: VNA measurement and CST simulation results for the V-dot probe

After simulations and VNA measurements are performed on a standard cable, SMA connectors are placed on the PFL to obtain the signal generated from the PFL after the spark gap, as shown in Figure 4.43.

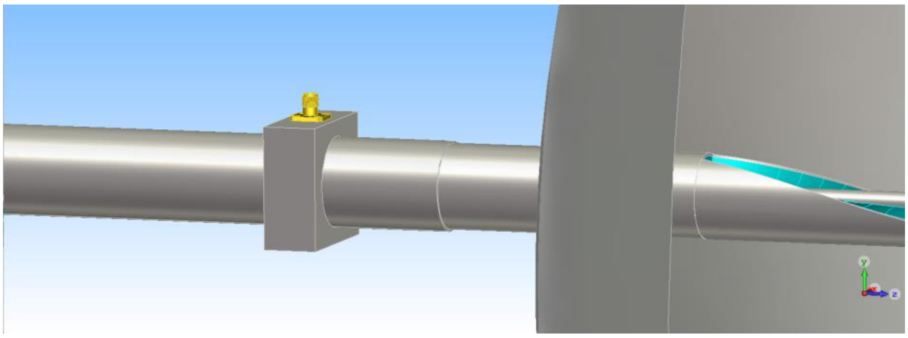

Figure 4.43: CST sketch of the V-dot probe

Since the LMR-1700 cannot be used with the PFL, the V-dot probe is mounted on the coaxial PFL.

After finding the transfer function of the probe, the signal processing steps to be taken can be seen in Figure 3.24. The FFT of the raw data obtained from the oscilloscope is switched to the frequency domain and the frequency response of the signal feeding the antenna is reached via the transfer functions. Then, by evaluating IFFT, the voltage produced by the PFL and feeding the antenna is obtained in the time domain. This is the voltage signal obtained from the probe.

4.6 System

In the previous sections, design, simulation, and production of all individual components are described. In this section, we consider their combinations into a small-scale EMP system. The chamber where the Marx generator is placed is designed as cylindrical structure, which acts an outer conductor to reduce the inductance of the Marx generator. The return conductor structure has also continued in the PFL. In Figure 4.44, a sketch of the assembled system before the production is illustrated. A butterfly-shaped mechanical piece is designed for the transition from the balun to the feed arms of the antenna, and all arms are assembled with the balun, as shown in Figure 4.45. The inner conductor of the balun is in contact with the upper arms, while the lower arms are in contact with the outer conductor of the balun. Resistors are added to the junction between the feed arms and the reflector, and the connection is made by supporting them with small non-conductive pieces. The SMA connector for the V-dot probe is placed on the transmission line.

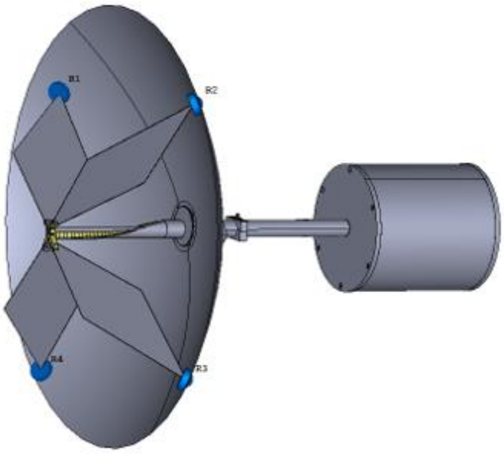

Figure 4.44: System mechanical sketch

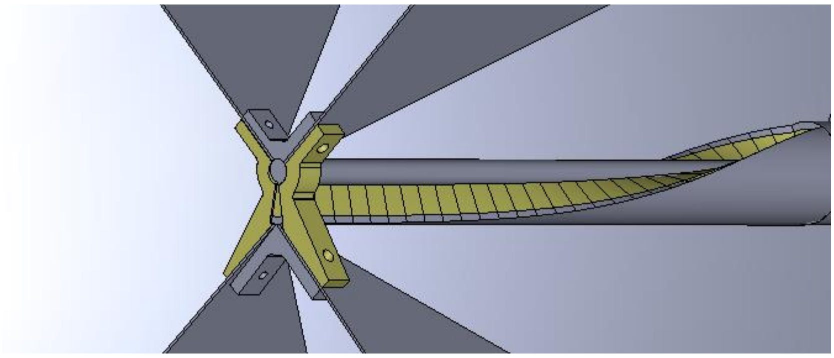

Figure 4.45: Feed arm and balun junction with mechanical support

In Figure 4.46, cutting plane image is given. Oil reservoir, spark gap, Marx generator chamber, and V-dot probe can be observed in this figure.

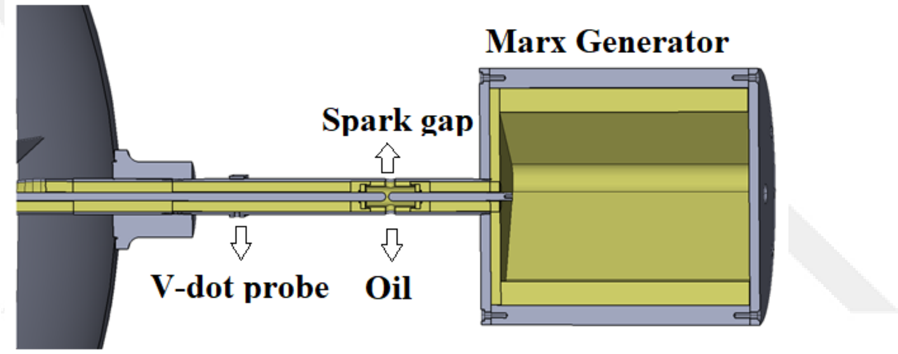

Figure 4.46: PFL and spark gap CST sketch

For the sealing of the oil chamber, a mechanical design is constructed, where O-rings are used. The spark gap can be varied by moving the inner conductor back and forth, as illustrated in Figure 4.47. The performance of the closing switch, which uses Shell Diala ZX-I transformer oil in the spark gap chamber and has a gap distance of approximately 1-2 mm, is demonstrated by experiments.

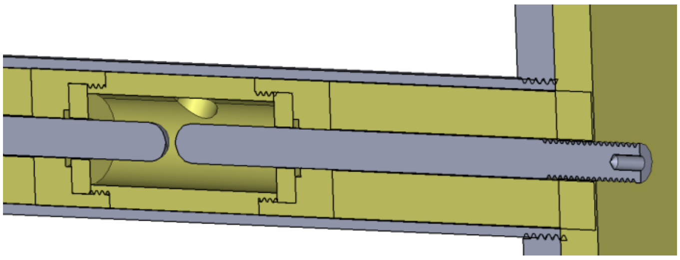

Figure 4.47: Spark gap and oil chamber

4.6.1 Experiments

Following few revisions, including mechanical designs, the fabricated components are integrated and prepared for the experiments. Figure 4.48 shows the integrated balun, reflector, feed arms, and termination resistors.

Figure 4.48: Conventional IRA and coaxially tapered balun

Experiments are started by placing the antenna part combined with the Marx generator and PFL on a vehicle, as shown in the photograph in Figure 4.49. V-dot probe is placed on the PFL and connected to an oscilloscope.

Figure 4.49: Photograph of the entire system

The V-dot probe and spark gap chamber on the PFL can be seen in Figure 4.50. The spark gap chamber is filled with clean transformer oil to cover the electrodes and it is not pressurized.

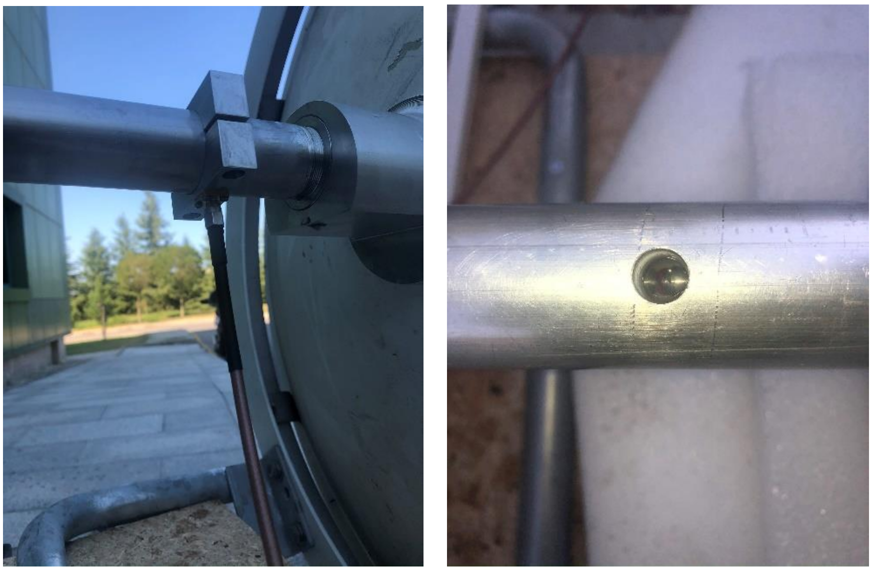

Figure 4.50: V-dot probe and spark gap image

With the help of a variac, each stage of the Marx generator is charged to 10 kV, and the Marx generator charges the peaking capacitor while discharging. In the experiments, the spark gap on the PLF is observed to operate as desired.

Montena D-dot probe shown in Figure 4.51 is further used to measure the electric field strength created across the antenna. The probe placed 15 meters away from the antenna is connected to a Keysight 6 GHz oscilloscope with fiber optic cables to observe the raw data of the electric field. D-dot probe obtains the derivative of the electric field strength in the air.

Figure 4.51: D-dot probe manufactured by Montena

In the first outdoor experiments, data could not be obtained from the V-dot probe. Arc problems was experienced at the antenna feed arms and feed point of the PFL, which is the connection between the Marx generator and the PFL. This undesirable arcing problem was mitigated by increasing insulation at the feed point. It was seen that the spark gap in the PFL works, enabling the observation and extraction of data from the D-dot and V-dot probes. But arcing problems on the antenna could not be solved completely.

In the experiments, the spark gap is about 0.2 mm and filled with transformer oil. The raw data obtained from the D-dot probe, which is located 15 m away from the antenna, can be seen in Figure 4.52. After the raw data is processed, the E-field strength 15 m away from the antenna is obtained, as shown in Figure 4.53. It is remarkable that, at 15 m, peak-to-peak 1.5 kV/m electric field strength is observed, while the first part of the signal is in the pulse form. It has about 1.7 ns rise time and 4 ns pulse width. The oscillations seen in the pulse signal are not desired, and it is predicted that they may be due to oscillations of the Marx generator or ground reflections. Since a tail-cut switch is not used, the pulse cannot be cut quickly, and oscillations continue. The frequency spectrum of the signal with these oscillations is examined by evaluating the FFT, leading to the result shown in Figure 4.54. In the first experiments, approximately 450 MHz bandwidth is obtained.

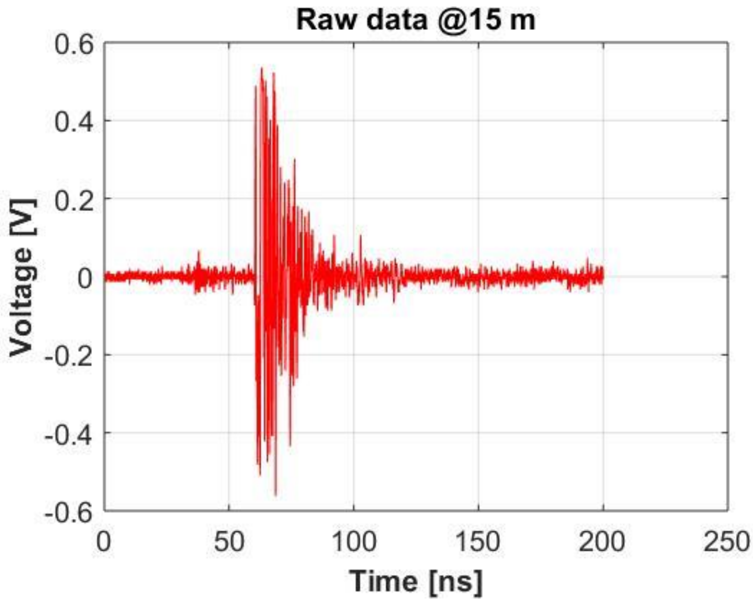

Figure 4.52: Raw data obtained with the Montena D-dot probe

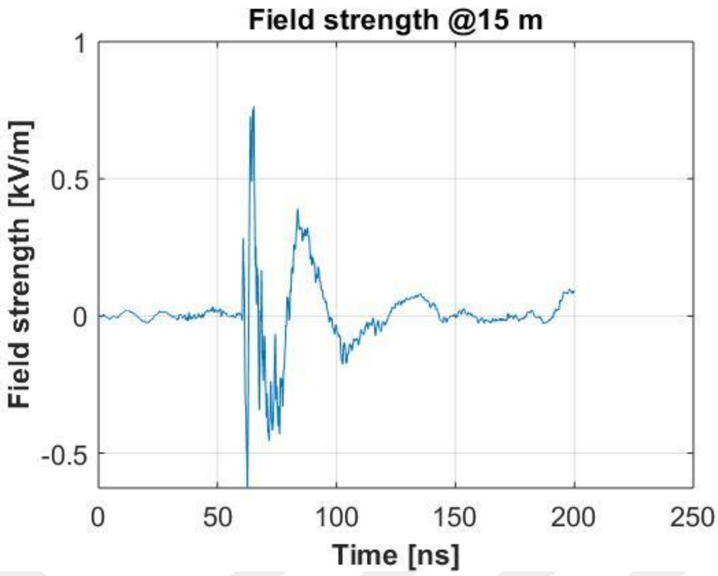

Figure 4.53: Pulsed E-field strength at 15 m

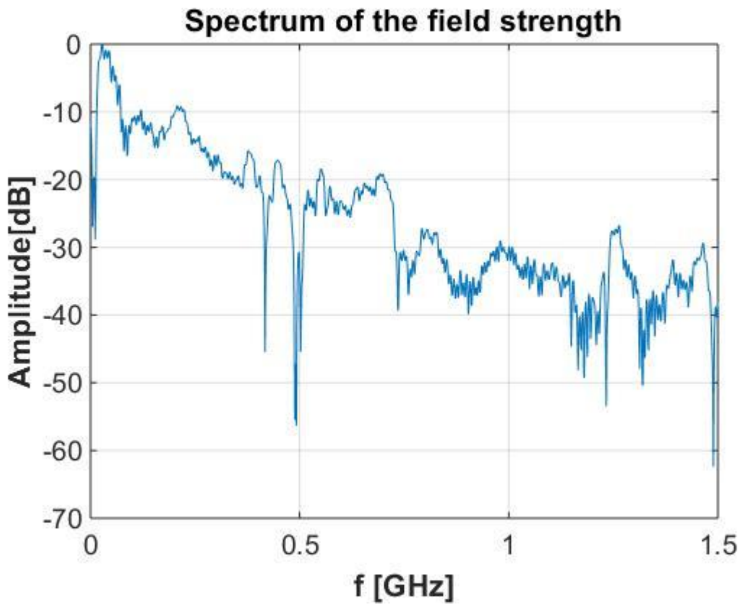

Figure 4.54: Frequency spectrum of the E-field signal

Fourier transform is further evaluated by taking only the “pulse part” of the observed E-field strength, in order to examine the frequency spectrum of this part. The examined pulse and the FFT signal can be seen in Figure 4.55 and Figure 4.56, respectively. In the spectrum, roughly 750 MHz bandwidth can be observed at -20 dB level.

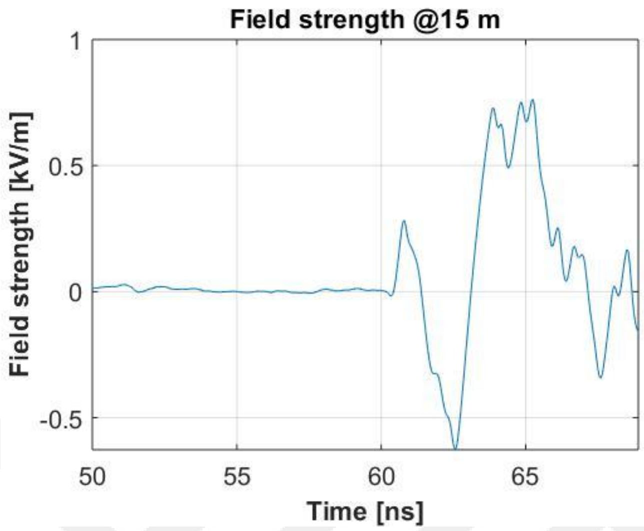

Figure 4.55: Pulse signal observed from the D-dot probe

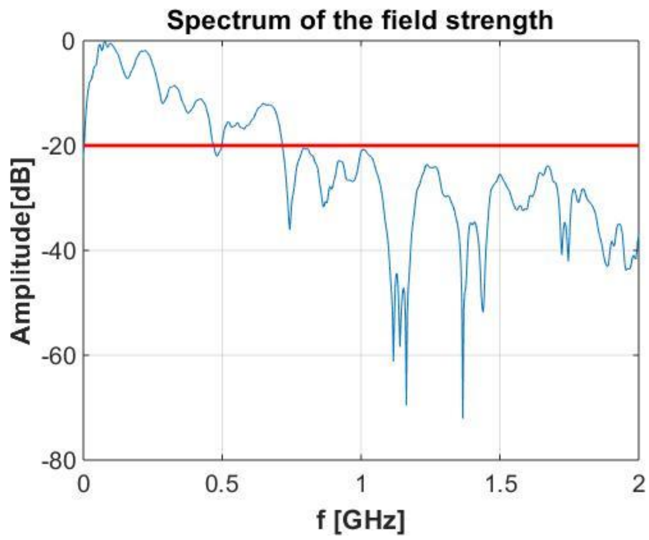

Figure 4.56: Frequency spectrum of the E-field signal

Consistent results are obtained in the whole experiment set involving as many as 50 shots. Experiments were also carried out without changing the spark gap distance and without oil filling. It has been observed that the signal form in the air environment is still the same, but there is a decrease in the bandwidth as shown in Figure 4.57. Since the breakdown voltage level of the air is low, the spark gap works earlier.

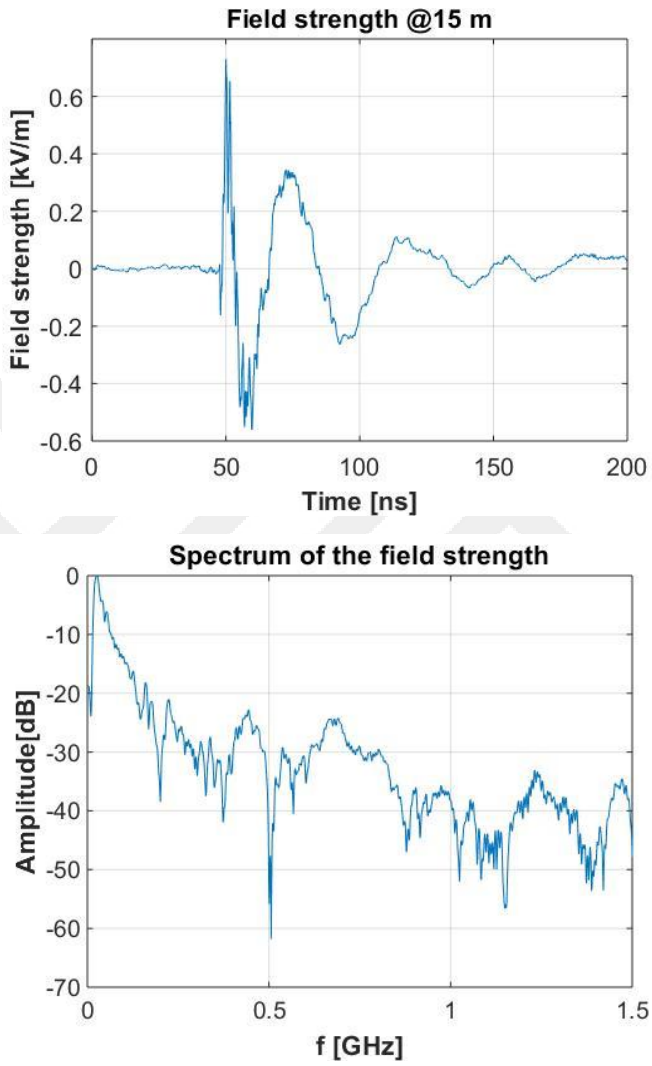

Figure 4.57: E-field strength and its frequency spectrum when the spark gap is in air

In several shots, electric field pulse signals with different forms are also observed, as shown in Figure 4.58. The bandwidth of this sample signal is 750 MHz, while the peak-to-peak amplitude is 1 kV/m. It is predicted that this type of signals may result from unwanted breakdowns in the PFL or on the antenna.

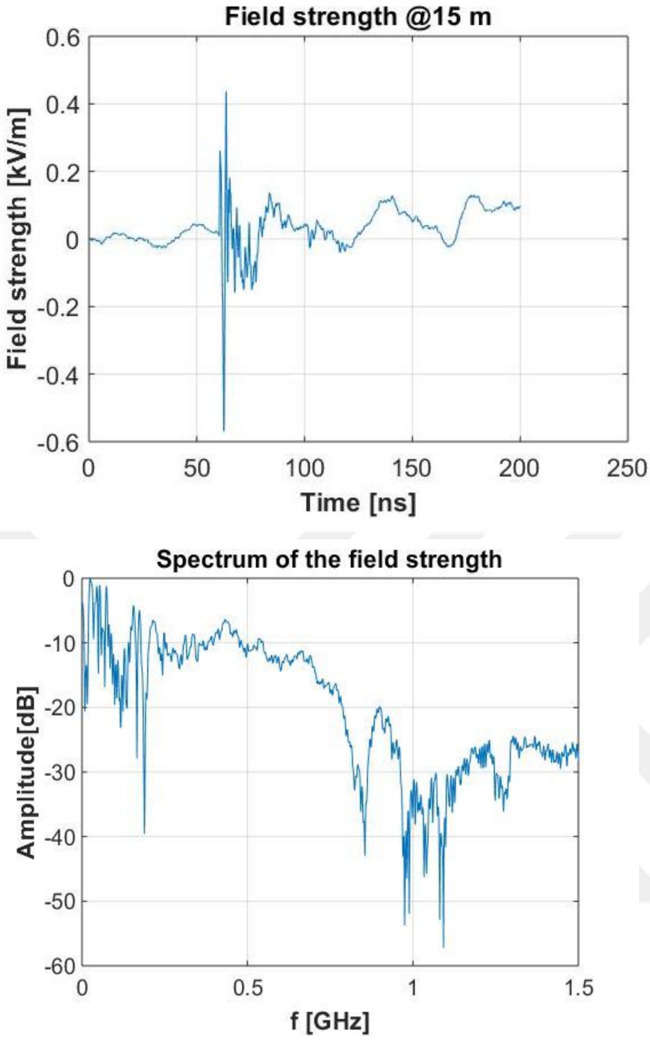

Figure 4.58: E-field strength at 15 m

The raw data taken from the V-dot probe and its frequency spectrum can be seen in Figure 4.59 and Figure 4.60. When it is examined, the frequency spectrum of the data is observed to be outside the linear region of the transfer function of the V-dot probe, as it remains in 300 MHz bands at -20 dB point.

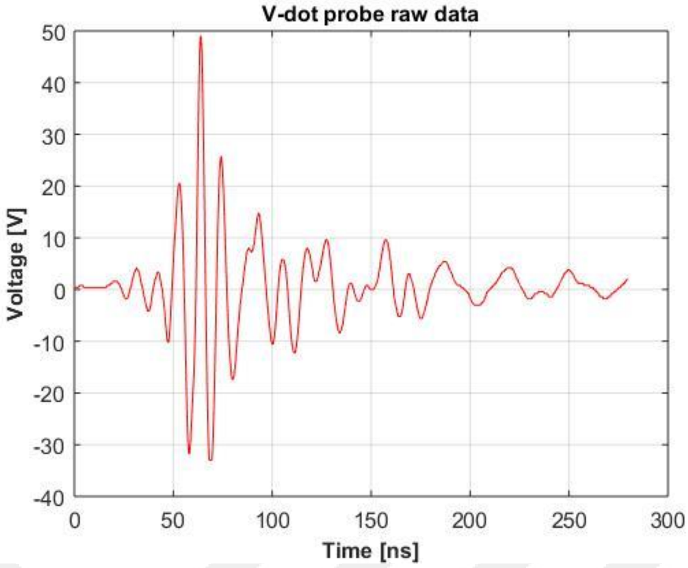

Figure 4.59: Raw data observed from the V-dot probe

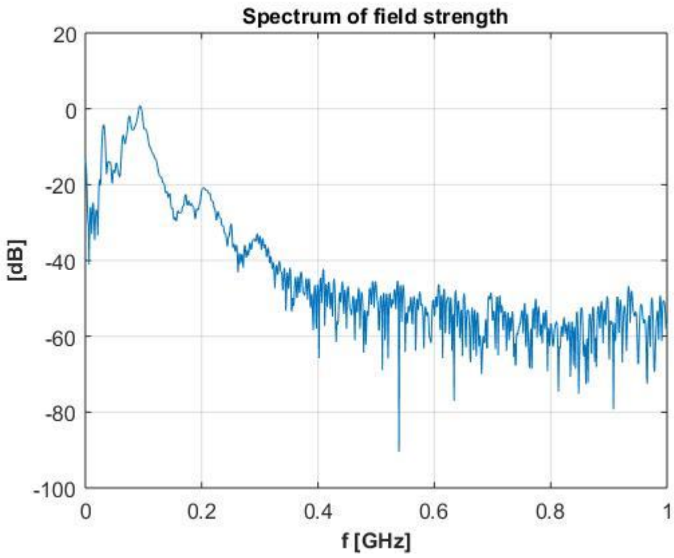

Figure 4.60: Frequency spectrum of the V-dot probe raw data

4.6.2 Conclusion

As discussed in this chapter, the designed PFL, balun, IRA, and V-dot probe are finally integrated with the Marx generator to build the entire system and perform experiments. Experiments involving as many as 50 shots provide consistent results measured for the D-dot probe. Although a tail-cut switch is used to obtain a sharp pulse in the literature, no tail-cut switch study was performed in this thesis.

All experiments are carried out outdoors. No data could not be obtained from the V-dot and D-dot probes in the first trials. Arc problems are experienced at the antenna feed arms and feed point of the PFL, which is the connection between the Marx generator and the PFL. This undesirable arcing problems are mitigated by increasing insulation at the feed point.

As a result of the experiments, it is shown that peak-to-peak 1.2 kV/m electric field intensity can be reached at approximately 15 m using a 50-kV Marx generator. When the frequency domain results are examined, it is seen that the oscillations that follows the pulse suppress the high-frequency components. Nevertheless, 750 MHz bandwidth can be observed from the experiment results.

CHAPTER 5

CONCLUSION

In the scope of this thesis, an impulse radiating antenna system driven by a Marx generator, was studied and experimented. In the context of the study, it was aimed to obtain an electromagnetic pulse with high amplitude across the antenna. Before its implementation, the design of the system was determined by examining existing systems and alternative solutions presented in the literature. Marx generator, PFL, balun, IRA, and V-dot probe designs were investigated in detail.

In the first stage, the Marx generator structure and its operating principles were studied. Both Pspice simulations and experiments were carried out. Load effect in the Marx generator, which obtains different signals according to load, was observed. Then PFL design and simulations were performed by considering a coaxial PFL structure and it was observed that the length of the PFL affects the pulse width. Coaxial PFL was designed so that the spark gap distance can be kept less than 1 mm by using transformer oil to obtain a very fast rise time.

Alternative solutions were considered to transfer the signal from the PFL to the IRA and to switch from the coaxial structure to the feed arm of the IRA. As a novelty, IRA simulations were carried out with Klopfenstein tapered balun, and return loss parameters, radiation patterns, electric field probe signals were examined. The final design was reached after an optimization process. A reflector with a F/D ratio of 0.33 was used, as it was available at TÜBİTAK BİLGEM. After a long time for fabrication and integration of the system, tests were carried out.

In the first experiments, arcing problems were experienced in the transition from the Marx generator to the PFL, and it was observed that the spark gap in the PFL did not breakdown. Insulation was increased to overcome arcing problems, and the issues in the feed point part were partially solved.

Electric field signals were measured with the Montena D-dot probe placed 15 m away from the antenna, and the E-field strength signal was obtained by integrating the received raw data. Nanosecond-level rise time and pulse duration and approximately 1.5 kV/m peak-to-peak E-field strength was observed, in addition to 0-750 MHz bandwidth in the frequency domain.

As a future work, oscillations which follow the pulse can be cut using a tail-cut switch. Different pressurized gas, oil, or vacuum systems can be used in the PFL and picosecond-level rise times and pulse durations can be seen across the antenna. Thus, GHz frequency components can be observed in the electric-field signal. Furthermore, insulation can be increased to solve the remaining arcing problems on the antenna. Finally, the V-dot probe can be calibrated with a standardized commercial impulse generator. Then, the signal which is generated by PFL can be calculated and further improvements can be obtained.

REFERENCES

[1] J. Biela, "Solid State Pulse Modulators," https://www.hpe.ee.ethz.ch.

[2] J. D. Taylor, W. C. Nunally, R. N. Edwards, and D. V. Giri, "Blumlein Impulse Generator and TEM Radiator," in *Introduction to Ultrawideband Radar Systems*, CRC Press, 1995, p. 287.

[3] R. Hoad, N. J. Carter, D. Herke, and S. P. Watkins, "Trends in EMC susceptibility of IT equipment," *IEEE Trans. Electromagn. Compat.,* vol. 46, pp. 390-395, Aug. 2004.

[4] V. I. Koshelev, Y. I. Buyanov, Y. A. Andreev, V. V. Plisko, and K. Sukhushin, "Ultrawideband radiators of high-power pulses," in *Proc. IEEE Pulsed Power Conf.*, 2001.

[5] S. Bazzoli, Caractérisation et simulation de la susceptibilité des circuits intégrés face aux risques d'inductions engendrées par des Micro-ondes de Fortes Puissances, France: Thèse de Doctorat, l'Université de Lille I, Villeneuve d'Ascq, 2005.

[6] J. Benford, J. A. Swegle, and E. Schamiloglu, High-Power Microwaves, New York: Taylor & Francis, 2007, p. 531.

[7] D. V. Giri and F. M. Tesche, "Classification of intentional electromagnetic environments (IEME)," *IEEE Transactions on Electromagnetic Compatibility*, vol. 46, pp. 322-328, 2004.

[8] M. Uman, The Lightning Discharge, New York: Academic, 1987, p. 118.

[9] W. D. Prather, C. E. Baum, R. J. Torres, and F. Sabath, "Survey of worldwide high-power wideband capabilities," *IEEE Transactions on Electromagnetic Compatibility,* vol. 46, pp. 335-344, 2004.

[10] C. E. Baum, "Switched oscillators,in circuit and electromagnetic system design note 45," Air Force Res. Lab. Kirtland AFB, NM, Sept. 2000.

[11] J. Bohletal, "Fundamental requirements of compact and effective HPM sources and an overview of HPM sources for different applications," in *Proc. AMEREM*, Annapolis, MD, June 2002.

[12] K. Ruffing, "Compact pulsed power RF demonstrator," in *Proc. 14th IEEE Int. Pulsed Power Conf.*, Dallas, TX, June 2003.

[13] T. Ehlen, J. Bohl, R. Kulnke, and F. Sonnemann, "Compact HPM and UWB sources using explosives—The potential of future nonlethal warhead systems," in *Ultra-Wideband, Short-Pulse Electromagnetics 5,* New York: Plenum, 2002.

[14] J. W. Burger, C. E. Baum, W. D. Prather, R. J. Torres, T. C. Tran, M. D. Abdalla, M. C. Skipper, and B. C. Cockreham, "Design and development of a high voltage, coaxial hydrogen switch," in *Ultra Wideband Short-Pulse Electromagnetics 6*, New York: Plenum, 2003.

[15] W. M. Henderson, D. E. Voss, A. L. Lovesee, E. Mokole, M. Kragalott, and K. Gerlach, "The etcheron valley outdoor high power electromagnetic test facility and the transient high output radiator (THOR)," in *Ultra-Wideband/Short-Pulse Electromagnetics 6,* New York: Plenum, 2003.

[16] D. V. Giri, H. Lackner, I. D. Smith, D. W. Morton, C. E. Baum, J. R. Marek, W. D. Prather, and D. W. Scholfield, "Design, fabrication, and testing of a paraboloidal reflector antenna and pulser system for impulse like waveforms," *IEEE Trans. Plasma Sci.,* vol. 25, pp. 318-326, 1997.

[17] W. D. Prather, "The 6 IRA," in *Proc. Nat. Radio Science Meeting*, Boulder, CO, Jan. 2001.

[18] C. E. Baum, "Variations on the impulse radiating antenna theme," Sensor and Simulation Note 378, Kirtland AFB, NM, Feb. 1995.

[19] C. E. Baum, "JOLT: A highly directive, very intensive, impulse-like radiator," Sensor and Simulation Note 480, 2003.

[20] F. Sabath, D. Nitsch, M. Jung, and G. Weise, "Design and setup of a short pulse simulator for susceptibility investigations," Sensor and Simulation Notes 460, Air Force Res. Lab., Kirtland AFB, NM, Oct. 2001.

[21] J. S. Schoenberg, J. S. Tyo, J. W. Burger, M. D. Abdalla, and M. C. Skipper, "A linear array of ultra-wideband radiators driven by photoconductive, semiconductor-switched blumleins," in *Ultra-Wideband*, *Short-Pulse Electromagnetics 4*, New York: Plenum, 1999.

[22] B. Martin and P. Delmote, "Design of an ultra-compact UWB pulse ormer," in *16th IEEE International Pulsed Power Conference*, Albuquerque, NM, USA, 2007.

[23] A. Pokryvailo, Y. Yankelevich, and M. Shapira, "A compact source of subgigawatt subnanosecod pulses," *IEEE Transactions on Plasma Science,* vol. 32, pp. 1909-1918, 2004.

[24] K. Rainwater, D. Barnett, C. Lynn, J. Dickens, A. Neuber, and J. Mankowski, "A 160 J, 100 Hz repetition rate, compact Marx generator for driving an HPM source," in *IEEE International Power Modulator and High Voltage Conference*, 2016.

[25] J. R. Mayes, C. Hatfield, J. Byman, D. Kohlenberg, and P. Flores, "Design and performance of a 4 MV, 14 kJ Marx jenerator," in *IEEE Pulsed Power and Plasma Science (PPPS)*, Orlando, 2019.

[26] B. Cadilhon, B. Cassany, and P. Modin, "Repetitive auto-triggered Marx generator as the driver of an ultrawideband source," in *IEEE Pulsed Power Conference*, 2009.

[27] T. Huiskamp, S. J. Voeten, E. J. M. Heesch, and A. J. M. Pemen, "Design of a subnanosecond rise time, variable pulse duration, variable amplitude, repetitive, high-voltage pulse source," *IEEE Transactions of Plasma Science,* vol. 42, no. 1, pp. 127-137, 2014.

[28] T. Huiskamp, "Nanosecond pulsed power technology for transient plasma generation," PhD dissertation, Technische Universiteit Eindhoven, Eindhoven, 2015.

[29] T. Huiskamp, E. J. M. Heesch, and A. J. M. Pemen, "Final implementation of a subnanosecond rise time, variable pulse duration, variable amplitude, repetitive, high-voltage pulse source," *IEEE Transactions on Plasma Science,* vol. 45, pp. 444-451, 2015.

[30] B. Cadilhon, L. Pécastaing, T. Reess, P. Pignolet, and A. S. Ferron, "High pulsed power sources for broadband radiation," *IEEE Transactions on Plasma Science,* vol. 38, pp. 2593-2603, 2010.

[31] T. Heeren, J. T. Camp, J. F. Kolb, and K. H. Schoenbach, "250 kV sub-nanosecond pulse generator with adjustable pulse-width," *IEEE Transactions on Dielectrics and Electrical Insulation,* vol. 14, no. 4, pp. 884-888, 2007.

[32] J. T. Camp, S. Xiao, and K. H. Schoenbach, "Development of a high voltage, 150 ps pulse generator for biological applications," in *IEEE International Power Modulators and High-Voltage Conference*, Las Vegas, 2008.

[33] S. Pinguet, J. Dupéroux, P. Delmote, F. Bieth, and R. Bischoff, "Short-pulse Marx generator for high-power microwave applications," *IEEE Transactions on Plasma Science*, vol. 41, no. 10, pp. 2754-2757, 2013.

[34] P. Delmote, J. Dupéroux, F. Bieth, and S. Pinguet, "Performances of an ultra compact, high-power, monocycle pulse former for WB and UWB applications," in *IEEE Pulsed Power Conference*, Chicago, 2011.

[35] J. Ryu, "Electromagnetic transient simulation of spark gap switched pulse generators for predicting pulse waveforms," *IEEE Transactions on Plasma Science*, vol. 42, pp. 2193-2197, 2014.

[36] J. S. Tyo, "Optimization of the TEM feed structure for four-arm reflector impulse radiating antennas," *IEEE Transactions on Antennas and Propagation*, vol. 49, pp. 607-614, 2001.

[37] J. S. Tyo, "Optimization of the feed impedance for an arbitrary crossed-feed arm impulse radiating antenna," Sensor and Simulation Note 438, 1999.

[38] M. Valibeiglou and A. Khaleghi, "A reflector impulse radiating antenna (IRA) with a new feeding structure," in *The 8th European Conference on Antennas and Propagation*, 2014.

[39] D. K. Singh, D. C. Pande, and A. Bhattacharya, "A new feed for reflector based 100Ω impulse radiating antenna," in *Progress In Electromagnetics Research Symposium Proceedings*, Malaysia, 2012.

[40] D. K. Singh, D. C. Pande, and A. Bhattacharya, "Improved feed design for enhance performance of reflector based impulse radiating antennas," Sensor and Simulation Notes 565, June 2013.

[41] M. Mantegh and Y. Rahmat-Samii, "Improved feeding structures to enhance the performance of the reflector impulse radiating antenna (IRA)," *IEEE Transactions on Antennas and Propagation*, vol. 54, pp. 823-834, 2006.

[42] L. H. Bowen and E. G. Farr, "A high-voltage cable-fed impulse radiating antenna," Sensor and Simulation Note 507, 2005.

[43] L. Bowen and E. Farr, "An improved collapsible impulse radiating antenna," Sensor and Simulation Notes 444, 2000.

[44] L. Bowen and E. Farr, "Experimental results of the optimizing the location of the feed arms in a collapsible IRA and solid IRA," Sensor and Simulation Notes 450, 2000.

[45] V. Felix, R. Farhad, and M. Nicolas, "Design, realization, and experimental test of a coaxial exponential transmission line adaptor for a half-impulse radiating antenna," *IEEE Transactions on Plasma Science*, vol. 41, no. 1, pp. 173-181, 2013.

[46] S. O. Kuja, P. G. Wiid, and T. J. Phiri, "Optimization of impulse radiating antenna for time domain metrology," in *International Conference on Electromagnetics in Advanced Applications (ICEAA)*, Verona, Italy, 2017.

[47] D. Pozar, Microwave Engineering 3rd Ed., Wiley, 2005.

[48] D. Chang, "UWB balun for TEM horn antenna," in *International Conference on Applications of Electromagnetism*, 2010.

[49] N. Marchand, "Transmission line conversion transformers," *Electronics*, vol. 17, pp. 142-145, 1944.

[50] J. H. Cloete, "Exact design of the Marchand balun," in *9th European Microwave Conference*, Brighton, UK, 1980.

[51] J. H. Cloete, "Graphs of circuit elements for the Marchand balun," *Microwave Journal*, vol. 24, no. 5, pp. 125-128, 1981.

[52] V. P. Minerva and J. W. Duncan, "100:1 Bandwidth balun," *Proceedings IRE*, vol. 48, no. 2, pp. 156-164, 1960.

[53] P. Foster and S. Tun, "A wideband balun from coaxial line to TEM line," in *9th International Conference on Antennas and Propagation*, Eindhoven, 1995.

[54] S. K. Singh, "A high power UWB system with subnanosecond rise time using balanced TEM horn antenna," in *2014 IEEE International Power Modulator and High Voltage*, 2014.

[55] S. Ghosh, B. K. Sarkar, and S. V. Pandey, "TEM horn antenna using improved UWB feeding mechanism," in *38th European Microwave Conference*, Amsterdam, 2008.

[56] Z. Yue, Z. Anxue, J. Yansheng, and W. Wenbing, "A design of coaxial-to-horn antenna balun in ultra-wide band applications," in *IEEE Antennas and Propagation Society International Symposium*, Albuquerque, NM, USA, 2006.

[57] R. W. Klopfenstein, "A transmission line taper of improved design," *Proceedings of the IRE*, pp. 31-35, 1956.

[58] R. H. McKnight, Measurement of electrical quantities in pulsed power systems, Boulder, Colorado: Forgotten Books, 2-4 March 1981.

[59] C. A. Ekdahl, "Voltage and current sensors for a high-density z-pinch experiment," *Rev. Sci. Instrum.*, vol. 51, no. 12, pp. 1645-1658, 1980.

[60] S. Burkhart, "Coaxial E-field probe for high-power microwave measurement," *IEEE Trans. Microwave Theory and Techniques*, vol. 33, no. 3, pp. 262-265, 1985.

[61] T. C. Wagoner, "Differential-output B-dot and D-dot monitors for current and voltage measurements on a 20-MA, 3-MV pulsed-power accelerator," *Phys. Rev. ST Accel. Beams*, vol. 11, 2008.

[62] P. Ripka, "Electric current sensors: a review," *Meas.Sci.Tech.*, vol. 21, no. 11, p. 1120, 2010.

[63] "High Voltage Probes," North Star High Voltage, [Online]. Available: htttp://www.highvoltageprobes.com.

[64] A. Lorusso, V. Nassisi, and M. V. Siciliano, "Fast capacitive probe for electromagnetic pulse diagnostic," *Rev. Sci. Instrum.*, vol. 79, no. 6, p. 064702, 2008.

[65] C. Yao, Q. Xiao, Y. Mi, T. Yuan, C. Li, and W. Sima, "Contactless measurement of lightning current using self-integrating B-dot probe," *IEEE Trans. Dielectr. Electr. Insul.*, vol. 18, no. 4, pp. 1323-1327, 2011.

[66] J. Lehr and P. Ron, Foundations of Pulsed Power Technology, IEEE Press, 2017.

[67] T. Huiskamp, F. J. Beckers, E. J. M. Heesch, and A. J. M. Pemen, "First implementation of a subnanosecond rise time, variable pulse duration, variable amplitude, repetitive, high-voltage pulse source," *IEEE Transactions on Plasma Science*, vol. 42, no. 3, pp. 859-867, 2014.

[68] T. Huiskamp, F. J. Beckers, E. J. M. van Heesch, and A. J. M. Pemen, "B-Dot and D-Dot sensors for (sub)nanosecond high-voltage and high-current pulse measurements," *IEEE Sensors Journal*, vol. 16, no. 10, pp. 3792-3802, 2016.

[69] B. M. Novac, R. Xiao, T. Huiskamp, L. Pécastaing, M. Wang, and P. Senior, "Theoretical and experimental studies of off-the-shelf V-dot probes," *IEEE Transactions on Plasma Science*, vol. 46, no. 8, pp. 2985-2992, 2018.

[70] R. Fitch, "Marx-and Marx-like high voltage generators," *IEEE Trans. Nucl. Sci.*, vol. 18, no. 4, pp. 190-198, 1971.

[71] G.W. Swift, "Charging time of a high voltage impulse generator," *IEEE Electron Lett.*, vol. 5, no. 21, p. 534, 1969.

[72] J. Francis, "High voltage pulse techniques report 74-2639-5," AFOSR, 1976.

[73] E. Husain and R. S. Nema, "Analysis of paschen curves for Air, N2 and SF6 using the townsend breakdown equation," *IEEE Transactions on Electrical Insulation*, vol. 17, no. 4, pp. 350-353, 1982.

[74] R. Curry, P. D. Champney, C. Eichenberger, J. Fockler, D. Morton, and R. Sears, "The development and testing of subnanosecond rise, kilohertz oil switches for the generation of high-frequency impulses," *IEEE Trans. Plasma Sci*, vol. 20, no. 3, pp. 383-392, 1992.

[75] R. D. Curry and C. Yeckel, "Pulsed breakdown characterization of advanced liquid dielectrics for high-power high-pressure rep-rate oil switching," in *IEEE Pulsed Power Conference*, 2009.

[76] T. Zhao, Y. Liu, F. Lv, X. Cheng, Z. Wang, F. Wang, and Q. Xie, "Breakdown characteristics of transformer oil insulation under impulse voltage with different waveform parameters," in *Electrical Insulation Conference (EIC)*, USA, 2017.

[77] M. G. Danikas, "Breakdown of transformer oil," *IEEE Electrical Insulation Magazine*, vol. 6, no. 5, pp. 27-34, 1990.

[78] R. M. D. Vecchio, "Geometric effects in the electrical breakdown of transformer oil," *IEEE Transactions on Power Delivery*, vol. 19, no. 2, pp. 652-656, 2004.

[79] J. Martin, "Nanosecond pulse techniques," *Proc. IEEE,* vol. 80, no. 6, pp. 934-945, 1992.

[80] S. Altunc, "Focal waveform of a prolate-spheroidal impulse radiating antenna," PhD Dissertation, The University of New Mexico, Albuquerque, New Mexico, 2007.

[81] C. Baum, E. G. Farr, and D. Giri, "Review of impulse-radiating antennas," *Review of Radio Science,* pp. 403-439, 1999.

[82] J. Rosenlind, "The impulse-radiating antenna," MSc Thesis, Karlstads Universitet, Karlstads, 2009.

[83] C. E. Baum, "Selection of angles between planes of TEM feed arms of an IRA," Sensor and Simulation Note 425, 1998.

[84] L. H. Bowen and E. G. Farr, "Experimental results of optimizing the location of feed arms in a collapsible IRA and a solid IRA," Sensor and Simulation Note 450, 2000.

[85] L. Westergren and B. Rade, Mathematics Handbook for Science and Engineering, Studentlitteratur, 2004.

[86] Antenna Magus, "Tapered Balun Information," 3ds, [Online]. Available: https://www.3ds.com/.

[87] "CST Studio Suite," 3ds, [Online]. Available: https://www.3ds.com/.

[88] S. J. Voeten, "Matching high voltage pulsed power technologies," Ph.D. dissertation, Dept. Math., Eindhoven Univ. Technol, Eindhoven, North Brabant, Netherlands, 2012.

[89] "LMR-1700," Times Microwave, [Online]. Available: https://www.timesmicrowave.com/.